Research Repository UCD

Title	Profile Calculation and Bridge Damage Detection Using Vehicle-based Inertial Readings and the Fleet Monitoring Concept
Authors(s)	Ren, Yifei
Publication date	2022
Publication information	Ren, Yifei. "Profile Calculation and Bridge Damage Detection Using Vehicle-Based Inertial Readings and the Fleet Monitoring Concept." University College Dublin. School of Civil Engineering, 2022.
Publisher	University College Dublin. School of Civil Engineering
Item record/more information	http://hdl.handle.net/10197/13168

Downloaded 2026-04-30 18:55:44

The UCD community has made this article openly available. Please share how this access benefits you. Your story matters! (@ucd_oa)

© Some rights reserved. For more information

Profile Calculation and Bridge Damage Detection Using Vehicle-based Inertial Readings and the Fleet Monitoring Concept

by

Yifei Ren

This thesis is submitted to University College Dublin for the degree of PhD in the College of Engineering and Architecture

April 2022

University College Dublin,

School of Civil Engineering

Head of School:

Dr. Amanda Gibney

Thesis Supervisors:

Prof. Eugene J. OBrien

Dr. Jennifer Keenahan

Abstract

The aim of this research is to use inertial vehicle sensor data to determine road and rail profiles and ultimately to monitor bridge condition. A novel fleet monitoring concept is developed to determine profiles and detect bridge damage using a fleet of instrumented vehicles. To improve the robustness of the calculation, a Bayesian updating method is developed.

As a first step towards calculating the profile from vehicle acceleration response(s), a novel Inverse Newmark-Beta method is developed. For a single vehicle, the profile can be found if the vehicle properties are known. However, for a single vehicle, acceleration by itself is not enough to determine both profile and vehicle properties. Fortunately, a fleet of vehicles provides additional information that can be used to address this problem. To solve this fleet monitoring problem, the Inverse Newmark-Beta method is combined with the Cross Entropy (CE) optimisation method. Sprung mass and half-car models are used to represent the vehicle and test this method separately. Numerical results show that the calculated profiles are the same as the 'true' profiles which were used to generate the 'simulated measured' accelerations. The absolute values of the vehicle properties are not obtained accurately but this algorithm can determine the relative values, i.e., the properties expressed as a proportion of the vehicle mass. Noise is added to the measurements and is seen to have an influence on the calculated results.

The fleet monitoring concept is used again to determine a flexible railway profile, i.e., an uneven surface that deflects under the weight of the passing vehicle. The 'apparent profile' (AP) of the railway track is defined as the true surface profile plus components of track deflection under the moving vehicle. Again, the Inverse Newmark-Beta method and CE optimisation are used together to solve this problem. In this part of the thesis, the train is simulated as a 4-axle carriage model and the railway track is represented by a beam (the rail) supported on spaced sprung masses (the sleepers and foundations). The calculated AP of railway track is found to be very close to the true one.

Since the previous method is sensitive to noise, the fleet monitoring concept is also solved using a Bayesian Updating method. The road profile is again determined using the 'drive-by' measurements. The Markov Chain Monte Carlo method is used here to solve the problem, i.e., to find the vehicle properties and the profile. Results indicate that the calculated road profile is very close to the true profile and is insensitive to Gaussian noise in the (simulated)

measurements. In addition, it is possible to determine the relative vehicle properties at the same time. A 3-D ‘carpet’ road profile is also tested and shows good results.

This thesis goes on to use similar principles of fleet monitoring to assess bridge condition or health. Firstly, a novel method is proposed to calculate the moving reference influence line (MRIL), i.e., the deflection due to a moving (static) unit load at the (moving) location of that load. The results show that the MRIL can constitute an effective indicator of the behaviour and condition of a bridge. The AP of a railway bridge is used to calculate the MRIL. The AP experienced by the vehicle on the railway bridge is the true surface profile plus components of ballast and bridge deflection under the moving vehicle. This numerical approach is assessed using a blind test operated by an independent research group at the Norwegian University of Science and Technology. In the blind test, a frame structure is used to model the railway bridge/culvert and different levels of global damage are simulated on this bridge. Using a 4-axle train carriage model, the damage levels of the bridge are inferred by the calculated MRILs with very good accuracy. When a half car model is used to represent the train bogie, damage levels can be found again, but with less accuracy.

The bridge damage is then detected using the Bayesian Updating method, with the data found from the passing vehicles. Local damage is considered in the form of cracks in the bridge. The second moments of area of each segment (finite element) of the bridge is updated as data becomes available. It is shown in simulations that estimates of the bridge second moments of area can be found, including cases where there are multiple instances of local damage. The vehicle mass can be calculated in this process. Bridge bearing damage is also simulated in this section. Using the Bayesian method, the value of bearing rotational spring stiffness, bridge second moments of area and vehicle masses can be calculated at the same time which is a good way to detect bridge bearing damage.

Table of Contents

List of Figures

List of Tables

Declaration

The author hereby declares that this thesis, in whole or part, has not been used previously to obtain any degree in this, or any other university. Except where reference has been given in the text, it is entirely the author's own work. The author confirms that the library may lend or copy this thesis, upon request, for academic purposes.

Yifei Ren
April 2022

Acknowledgements

First of all, I would like to express my deepest gratitude to my supervisor, Prof. Eugene J. OBrien. I cannot complete this thesis without him. His knowledge, guidance, insight, and continuous encourage have immensely helped me throughout the PhD. I have learnt a lot from him. It has been a pleasure and honour to work with him. I also would like to express my appreciation to my co-supervisor, Dr. Jennifer Keenahan for her recommendation and encouragement. I have learnt an immense amount from her vast knowledge in proposing novel idea and writing scientific report. Due to the Covid-19 pandemic period, they kept in close contact with me and helped to solve the issues in both study and life. With their kind and wise counsel, I never felt alone over this long study journey.

I am grateful to the UCD-Chinese Scholarship Council (CSC) scheme for financially supporting my PhD study, and HEA for offering me extra subsidy to help me go through the hard time due to the COVID-19 pandemic.

I wish to thank Prof. Simon Wilson, who has provided support in Bayesian problem. I would like to thank Dr. Daniel Cantero, who spent much time preparing data to be used for a 'blind' test.

I would also like to thank my fellows and friends from the bridge group: Dr. Muhammad Arslan Khan and Kun Feng from Room G29; Room G30: Dr. Abdollah Malekjafarian, Dr. Paul C. Fitzgerald, Dr. Miguel Casero Florez, Dr. Daniel Martinez-Otero, Dr. E. Alexandra Micu and Shuo Wang. And some friends from other rooms: Yuxiang Zhang, Dr. Yan Yang, Dr. Ranbin Liu, Dr. Cheng Tang and Linda Heerey. Specially, Licheng Zhu, who is also my housemate in Windy Arbour and Sandymount. All of them are always willing to lend a helping hand and discussion to push the work forward at any time. Many activities are organized after work, and I spend a great time with all of them.

Thanks to all the staff in the Newstead building. In particular, thanks to Andrew Griffiths, David Morgan, John Ryan and Derek Holmes who were always extremely helpful and a pleasure for a chat. I am also sincerely thankful to Dr. Daniel McCrum, Dr. Fiachra O'Loughlin and Prof. Paul Fanning for their helpful advice during the Doctoral Studies Panel meetings.

I would like to thank my other friends in UCD. I am grateful for all the fond memories at every lunch or dining gathering, every activity and event and many more. A special thanks to Yi- thanks for all your support and good advice. And thanks to Momo, my lovely kitten. Thank you for being a part of my journey.

Thanks to Ireland. I never thought I would be here. I have spent 7 years in Ireland. It is not too long but one of most important and best time in my live. In these years I explored many beautiful cities and charming places. It is a long and sweet story.

Finally, I would like to thank my parents, grandparents, and other family members for their unconditional support and encouragement over the years. I'm extremely grateful to them for providing me with every opportunity in life and education.

Chapter 1 – Introduction

Chapter 1 – Introduction

1.1 Background

Roads and bridges are critical elements of any transportation network. They are expensive to construct and maintain. In the event of serviceability limits being exceeded, or bridge collapse, the infrastructure owners have to bear the cost of both maintenance/replacement and potentially lost revenue during any period of closure. The collapse of the Malahide viaduct in Ireland in 2009, due to undermining of a bridge pier from inter-tidal scouring action, is one such example. The direct cost of replacing the collapsed spans was approximately € 5 m (Anon, 2010). However, the combination of lost revenue and the requirement to provide a replacement bus service cost Irish Rail an additional € 5 m. Structural Health Monitoring (SHM) of bridges can provide a means to detect damage and aid maintenance planning, thereby helping to prevent bridge collapse, prolong service life and prevent unplanned repairs. Roads routinely become damaged with features emerging such as potholes or increased roughness. Railway tracks also have permanent settlement or 'soft spots' in the railway track, with excessive deformation in response to load. These damages may influence the serviceable and safe operation of the transportation network.

Traditionally SHM of roads and bridges has been undertaken using periodic visual inspections made by engineers and other technical staff. Owing to the large number of structures present on a transportation network, these methods are labour intensive, resulting in significant cost. The inspection challenge is exacerbated by the logistical complications associated with inspections of bridges over water and tall viaducts. It is difficult to achieve consistency in monitoring due to the subjective nature of the inspections. As a result of these and other challenges, there has been a shift towards sensor-based monitoring in recent years, with research being conducted into improving sensing technologies and diagnostic techniques (Fujino and Siringoringo, 2011).

The concept of 'drive-by' (indirect) monitoring of highway bridges was investigated by Yang et al. (2004), Yang and Lin (2005). Drive-by monitoring involves the placement of sensors on a passing vehicle. A major advantage of this 'indirect' monitoring is that an instrumented vehicle can monitor large parts of a network as a by-product of its normal operation. When a vehicle crosses a bridge, the bridge responds with a static deflection, combined with a dynamic oscillation. The presence of damage in the structure causes a change in bridge stiffness which

changes the modal properties, influencing both the static and dynamic responses. The response of the bridge is sensed by the passing vehicle which will also vibrate differently. Consequently, the response of the passing vehicle has the potential to be used to detect damage in the bridge. Malekjafarian et al. (2015), Yang et al. (2020a) review the state-of-the-art in drive-by health monitoring of highway bridges. The bridge dynamic properties such as natural frequency, mode shapes and damping are identified using measurements from a passing vehicle in many studies (Yang et al., 2004, Gonzalez et al., 2012, Zhang et al., 2012). Some other works focus on damage detection techniques without finding the conventional dynamic characteristics of the bridge.

The drive-by method is also used to determine road or railway track profiles. Many methods are developed to calculate profile height or to determine the road roughness class (Gonzalez et al., 2008, Harris et al., 2010). Using accelerations measured in moving trains, the longitudinal profile of the track and the foundation stiffness under the sleepers can be determined (OBrien et al., 2016, Yang et al., 2020b). These results show that passing vehicle measurements can be used to estimate road and track condition effectively.

Many drive-by monitoring methods involve a specialist vehicle driving on the infrastructure fitted with inertial sensors that extract information about the infrastructure. Specialist vehicles are expensive, and they do not typically travel on a road/railway more than once or twice per year, resulting in long intervals between condition reports. More importantly, accuracy is limited by the speed of the vehicle – it is extremely difficult to get accurate information on, for example, a short-span bridge in the second or two that it takes the vehicle to pass over it. Some drive-by methods use a complex Cross Entropy (CE) optimisation method to determine the profile which is computationally intensive (OBrien et al., 2016, OBrien and Keenahan, 2015).

This goal of this thesis is to extend the drive-by method to a vehicle fleet monitoring concept. The proposal is to extract drive-by data from the population of regular vehicles in the transportation network. Nowadays, vehicles are getting smarter with ever greater numbers of sensors, including accelerometers. It seems reasonable to assume that, in the medium or long term, the data from these vehicles can be accessible for road and bridge management purposes. With the rapid development of fifth generation (5G) communications technology, the performance of communications networks is improving and it may be possible to collect these data from drive-by vehicles in real time.

A major challenge in this thesis is the calibration problem, i.e., finding both the vehicle properties and the profile, knowing only the accelerations. A further goal is to monitor bridge condition with accelerations from the same vehicles, using the vehicle properties calculated from off-bridge data.

1.2 Research Objectives and Outline

The overall focus of this study is to develop the drive-by method using a fleet of operating vehicles. A fleet monitoring concept is developed to monitor roads, railways and bridges. A number of novel methods are proposed to estimate the road/track profile and to detect bridge damage. Vehicle-Bridge Interaction (VBI) simulation models are used extensively in this study. Figure 1.1 provides an outline of this thesis. It highlights the links between the key contributions of this work and the different chapters.

Chapter 2 of this thesis describes a novel Inverse Newmark-Beta method to determine the 2-dimensional (2-D) road profile exciting the vehicle, from its acceleration responses. The measured accelerations are simulated using a vehicle and road dynamic interaction model. Sprung mass and half-car models are tested separately. This method is effective and finds the profile with little computational effort. Combining the Inverse Newmark-Beta method with a Cross Entropy (CE) optimisation algorithm, the vehicle fleet monitoring concept is proposed to predict road profiles. Using this concept, the profiles can be calculated without prior knowledge of the vehicle properties.

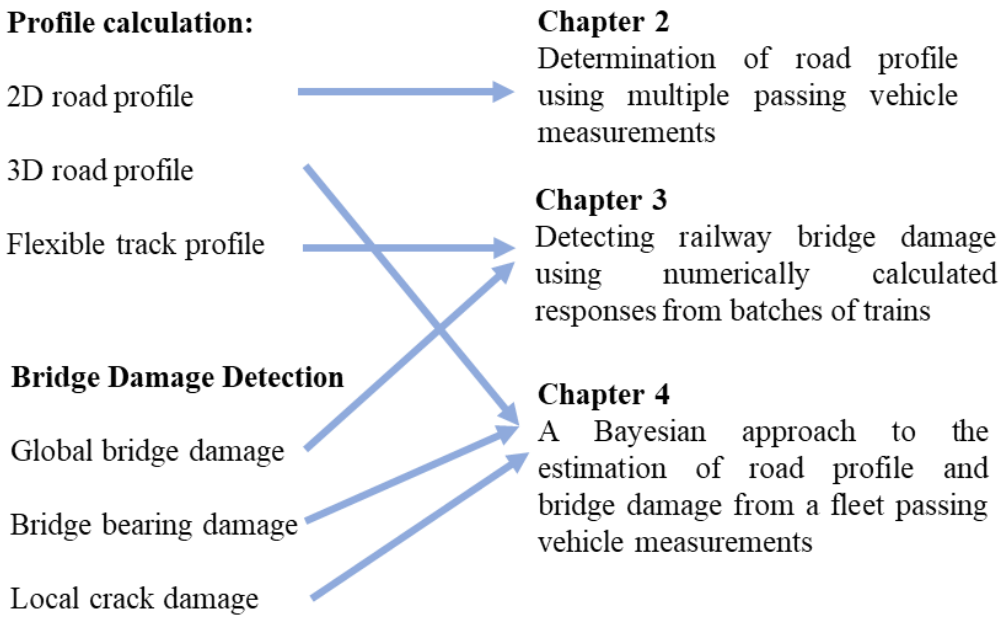

Figure 1.1 Chart showing the outline of the thesis.

Chapter 3 further develops the vehicle fleet monitoring concept and extends its application to railway tracks which have a flexible profile, i.e., a profile that deflects under load. It uses sensor data from a batch of in-service train passes to determine the apparent profile of railway track i.e., the true profile plus components of track deflection under the moving train. In this chapter, the concept is further extended to determine the structural health of a railway bridge. A train-track–bridge (TTB) dynamic model is used here which was developed by others (Cantero et al. (2016). The train is represented by a 4-axle railway carriage model and the track is modelled as a beam (the rail) supported on a spaced sprung mass system which is flexible. The apparent profile of the railway track is calculated from the Inverse Newmark-Beta method in combination with Cross Entropy (CE) optimisation. For bridge health monitoring, the apparent profile of the bridge is first determined, i.e., the true profile plus components of ballast and bridge deflection under the moving train. The apparent profile is used, in turn, to calculate the moving reference influence line, i.e., the deflection due to a moving (static) unit load. Global change of bridge stiffness is simulated as the type of damage in this section. The moving reference influence line constitutes an effective indicator of global damage of the bridge. This numerical approach is tested numerically using an elaborate finite element model operated by an independent research group.

Chapter 4 uses a Bayesian Updating method to calculate the road profile using data from a fleet of simulated vehicles. A 3-dimensional (3-D) road surface profile is simulated to allow for the fact that each vehicle may pass along the profile in a slightly different transverse position on the road and experience a slightly different profile. Gaussian noise is added to allow for inaccuracy in the acceleration measurements. This method can calculate the 2-D and 3-D profiles with good accuracy. This approach is also applied to monitor bridge damage. Firstly, it considers bearing damage, simulated as an increase in support rotational stiffness. The support rotational stiffnesses can be calculated with the Bayesian Updating method. Then, crack damage is simulated, assumed to affect the bending stiffness of a region equal to 1.5 times the beam depth on either side of the crack. Bayesian Updating is shown to be capable of estimating the values of the bridge second moments of area, thereby giving an estimate of both damage location and severity.

1.3 Thesis Structure

This thesis comprises three scientific papers which have either been submitted for publication or published. Each of Chapters 2 to 4 is a stand-alone paper which means that there may be

some repetition between chapters. It also means that each chapter has its own short literature review and there is no general review in the thesis. The status of each paper (submitted or published) is stated at the beginning of each chapter, along with an explanation of the candidate's contribution. It is the policy of the research group, generally, to rotate first authorship of publications. Two appendices are included at the end of the thesis. Appendix A introduces the Inverse Newmark-Beta integration method using a simple half car model to calculate the track AP. A more elaborate 4-axle vehicle model is used in the explanation of the concept in Chapter 3. Appendix B provides the detailed algorithm of the Inverse Newmark-Beta method for the 4-axle train carriage model used in Chapter 3 and the quarter-car model used in Chapter 4.

Chapter 2 – Determination of Road Profile Using Multiple Passing Vehicle Measurements

Authors:

Jennifer Keenahan

Yifei Ren

Eugene J. OBrien

Paper Status:

Published* in *Structure and Infrastructure Engineering* (2020), 16(9), 1262-1275.

Note to the Reader:

This chapter is the work of the author, under the supervision of Prof. OBrien and Dr. Keenahan.

* Some small updates have been made in the chapter since publication of the original paper.

Chapter 2 – Determination of Road Profile Using Multiple Passing Vehicle Measurements

2.1 Introduction

Over time, roads and bridges often become damaged due to vehicle overloading, bridge strikes and due to environmental effects. Undoubtedly, this damage may impact the safe running of the transportation network and consequently, infrastructure monitoring is an important area of research. Highway structures such as bridges are most commonly monitored by visual inspection that requires large numbers of inspectors and significant cost. Furthermore, due to human subjectivity and differing experience, it is often difficult to achieve consistency in the results.

Recently, the concept of sensor-based monitoring of road structures has become popular in the literature. It can be divided into two types: direct and indirect monitoring. Direct monitoring measures the response directly using sensors installed in the structure. This method requires multiple sensors to be mounted on a bridge, for example, which can be more expensive than traditional visual inspections. It also results in a significant amount of data being collected, stored, transmitted and processed. Furthermore, the direct sensing method is specific to the infrastructure in which the sensors are installed; these sensors cannot be subsequently reused in another structure. As a result, the concept of indirect monitoring (the drive-by method) is proposed for road profiles by Gonzalez et al. (2008) and for bridges by Yang et al. (2004), Yang and Lin (2005), Gonzalez et al. (2008). This family of methods uses inertial sensors installed in a passing vehicle to assess the condition of pavement, railway track or a bridge indirectly. There is no need for sensors to be installed in the road or on the bridge. This chapter proposes a new method of drive-by monitoring to determine the surface profile. For a road pavement or railway track, this can be used directly as a measure of pavement/track condition. For a bridge, the profile experienced by the vehicle includes elements of bridge deflection and, as such, can be used as an indication of the bridge condition. Compared to the direct method, indirect monitoring has a number of advantages; it is easy to operate, efficient, economic, and no power supply is needed in the infrastructure.

Road profiles are often monitored using specialist vehicles, particularly for highways and major roads. Sayers and Karamihas (1998), Sayers and Karamihas (1996) discuss inertial

profilometers, that can measure profiles at highway speeds. A typical inertial profilometer consists of a vehicle equipped with a height sensing device, such as a laser, which measures pavement elevations at regular intervals. The effects of the vehicle can be removed from the elevation measurements using accelerometer(s) mounted on the vehicle. High resolution profile measurements can be provided, but at significant cost because of the laser-based technology. Ergun et al. (2005) also measure road surface macrotexture with a laser profilometer. Ma et al. (2018) review developments in mobile laser scanning (MLS) techniques which introduce many MLS technology applications and show that this technology can achieve accurate road condition detection. These specialist vehicles are expensive and do not run frequently.

With considerably greater precision (and cost), Flintsch et al. (2012) identify continuous deflection devices such as traffic speed deflectometers (TSD's), as valuable tools in pavement analysis. Using a set of velocity-sensing lasers, the TSD measures the pavement deflection velocity based on the Doppler principle. Malekjafarian et al. (2017) use a vehicle pavement interaction model to illustrate the functionality of a TSD. The pavement is represented by a Winkler model and pavement deflections are calculated from the simulated TSD measurements. The deflections compare well to those from a numerical model. Later, OBrien and Keenahan (2015) propose a TSD-type vehicle containing two displacement sensors to measure pavement deflection. Using data collected from sensors in the TSD, the 'apparent profile' is calculated and the time-shifted difference in the apparent profile is used to indicate bridge damage. Numerical simulation suggests that this method can be used as a damage indicator in the presence of noise. It is shown to be economical, efficient and free from the influence of other heavy traffic on the bridge.

In recent years, different methods have been proposed to measure road surface profiles using smartphone in passing vehicles. The concept of using crowd sourcing to detect potholes or bumps in pavements is already established in the 'Street Bump' app in operation in Boston. However, this is a very simple empirical approach, most likely using an acceleration threshold in the smartphone, above which a bump is registered. There are also some challenges with this concept. For example, the quality of devices can limit the quality of the gathered information, compromising the precision (O'Leary, 2013). Souza et al. (2018) introduce a new system, Asfault, to evaluate and monitor road pavement condition using smartphone sensors. These sensors can measure the vehicle vibration while driving and use the data to evaluate pavement condition. This system classifies road quality into 4-classes: Good, Average, Fair, and Poor, as well as identifying the occurrence of obstacles on the road. Zang et al. (2018) use GPS and

accelerometer sensors on bicycle-mounted smartphones to measure the road surface roughness of pedestrian and bicycle lanes. Nevertheless, smartphone-based sensing has the challenges of low frequency and low detection accuracy (Sattar et al., 2018). Mei et al. (2020) use gyroscopes in smartphones to measure road deformation in a series of laboratory experiments. Du et al. (2020) develop a new method to recognize a damage road surface using accelerations from a smartphone. The improved Gaussian background model is used to extract the features of the damage pavement, and the k-nearest neighbour (kNN) algorithm is used to distinguish damage pavement types, including pothole and bump.

Accelerometer(s) mounted on the vehicle provide an accurate means to monitor road profile at low cost. Imine et al. (2006) present a method to estimate road profile by analysing the measured dynamic response of an instrumented vehicle. In this method, a full car sprung mass model is used to determine the road profile from the vertical wheel accelerations and vertical displacement and rotation of the vehicle body. Gonzalez et al. (2008) collect data from accelerometers fitted to a vehicle and use this data to estimate the condition of a road. This approach uses the relationship between vehicle accelerations and the power spectral densities of road surfaces using a transfer function. The road condition is classified using Fourier analysis to calculate the power spectral density (PSD) function of the surface. The result shows that road profile roughness can be accurately classified using axle and body accelerations from a range of simulated vehicle–road dynamic scenarios.

Harris et al. (2010) describe a novel method for the characterisation of road surface profiles using measurements of vehicle acceleration. The method proposes the use of a combinatorial optimisation technique to determine the road profile which causes a set of observed responses in a known vehicle model. The parameters of the half-car model are determined using road profiles and known accelerations. The algorithm is numerically validated for different road profiles and, while computationally intensive, the calculated road profile heights are found to provide a good fit to the true profiles. OBrien et al. (2014) present a method to monitor transport infrastructure (such as bridges and pavements) by analysing vehicle accelerations. Using the vehicle response, an algorithm is developed to identify the dynamic vehicle-bridge interaction forces. It is proposed that this method could be used to identify the global bending stiffness of the bridge and to predict the pavement roughness.

Fauriat et al. (2016) use a data processing algorithm to estimate road profiles from the dynamic responses measured on a vehicle. This algorithm, based on Kalman filtering theory, aims at

solving a so-called inverse problem, in a stochastic framework. The application of Kalman filters was investigated to classify road condition by Wang et al. (2016). Kim et al. (2019) propose an improved discrete Kalman filter to simultaneously estimate unknown road roughness input and state variables for a vehicle suspension control system. Fox et al. (2017) develop a novel crowd-sourced system to monitor the road. This method uses accelerometer data from embedded vehicle sensors to detect and localize potholes in multi-lane environments. An Independent Component Analysis (ICA) technique is used to identify the road profile knowing the dynamic responses of the system (Ben Hassen et al., 2019).

Cross Entropy (CE) optimisation is sometimes used to solve optimisation problems in Civil Engineering. Walsh and Gonzalez (2009) use CE optimisation to estimate the stiffness distribution of a structure, given a set of displacements. Harris et al. (2010) use CE optimisation to infer the parameters of a vehicle model by examining the vertical acceleration response of the vehicle to a known excitation. Li et al. (2014) develop an optimization method to identify 1st frequency and stiffness of the bridge based on a Generalized Pattern Search Algorithm (GPSA). OBrien and Keenahan (2015) use CE optimisation to determine the apparent profile, where displacements recorded by the sensors are the assumed inputs. Quirke et al. (2016) use the CE optimisation technique to determine the track stiffness profile of a railway track. This method generates a vehicle response that best fits the measured vertical accelerations of a railway carriage bogie.

While the use of CE optimisation methods represents a step forward in solving engineering problems, the computational effort of doing so is a significant drawback. It is often grossly inefficient to solve engineering problems using optimisation in a brute-force manner. This chapter introduces a new indirect method of back-calculating the road profile from vehicle accelerations. Firstly, the chapter presents the Inverse Newmark-Beta algorithm for calculating the road profile using the vehicle acceleration histories. The work is then expanded to introduce the concept of using a fleet of vehicles to find the road profile more accurately, ever without prior knowledge of the vehicle properties. This fleet-based monitoring method uses the Inverse Newmark-Beta method and the CE algorithms together.

2.2 Model Description

2.2.1 Vehicle model

In this study, a variety of vehicle models are used. Initially, the work considers a sprung mass model, then a half-car model to represent vehicles travelling on profiles.

2.2.1.1 Sprung mass model

Firstly, the vehicle is represented as a sprung mass model, as shown in Figure 2.1. This simple dynamic system consists of a mass and a spring. The general equation of this single degree of freedom dynamical system can be expressed as:

$$m\ddot{u} + ku = F \tag{2.1}$$

where m and k are the mass and stiffness of the vehicle, respectively, $\ddot{u}$ and u are the vehicle acceleration and displacement respectively, and F is the applied force at the vehicle degree of freedom, ie, the force in the spring. F is related to profile $y(t)$ and can be expressed as:

$$F(t) = k \times y(t) \tag{2.2}$$

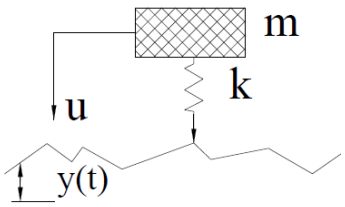

Figure 2.1 Sprung mass and profile model.

2.2.1.2 Half-car model

The vehicle is later extended to a 4 degree-of-freedom half-car model travelling on the road (Figure 2.2). The four independent degrees of freedom correspond to sprung mass bounce displacement, u_s sprung mass pitch rotation, θ_s and axle hop displacements of the unsprung masses at axle 1 and axle 2, u_{u1} and u_{u2} respectively. The sprung mass, m_s represents the vehicle body and I_s is the sprung mass moment of inertia. The unsprung masses, $m_{u,1}$ and $m_{u,2}$ represent the axle components. The sprung mass connects to the axle masses via a combination of springs and dampers. The stiffness of springs is $K_{s,i}$ and damping coefficients of viscous dampers are $C_{s,i}$ which represent the suspension components for the front and rear axles ($i =$

1,2). The axle masses connect to the road surface via springs with linear stiffnesses, $K_{t,i}$ which represent the tyre components for the front and rear axles ($i = 1,2$). Finally, the distances from the axles to the centre of gravity are D_1 and D_2.

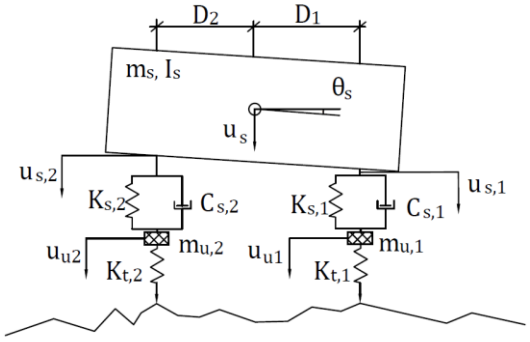

Figure 2.2 Half-Car and road model.

The equations of motion of the vehicle are obtained by imposing equilibrium of all forces and moments acting it:

$$M_v\ddot{u}_v + C_v\dot{u}_v + K_v u_v = f_v \tag{2.3}$$

where M_v, C_v, and K_v are the mass, damping and stiffness matrices of the vehicle respectively:

$$M_v = \begin{bmatrix} m_s & 0 & 0 & 0 \\ 0 & I_s & 0 & 0 \\ 0 & 0 & m_{u,1} & 0 \\ 0 & 0 & 0 & m_{u,2} \end{bmatrix} \tag{2.4}$$

$$C_v = \begin{bmatrix} C_{s,1} + C_{s,2} & D_1C_{s,1} - D_2C_{s,2} & -C_{s,1} & -C_{s,2} \\ D_1C_{s,1} - D_2C_{s,2} & {D_1}^2C_{s,1} + {D_2}^2C_{s,2} & -D_1C_{s,1} & D_2C_{s,2} \\ -C_{s,1} & -D_1C_{s,1} & C_{s,1} & 0 \\ -C_{s,2} & D_2C_{s,2} & 0 & C_{s,2} \end{bmatrix} \tag{2.5}$$

$$K_v = \begin{bmatrix} K_{s,1} + K_{s,2} & D_1K_{s,1} - D_2K_{s,2} & -K_{s,1} & -K_{s,2} \\ D_1K_{s,1} - D_2K_{s,2} & {D_1}^2K_{s,1} + {D_2}^2K_{s,2} & -D_1K_{s,1} & D_2K_{s,2} \\ -K_{s,1} & -D_1K_{s,1} & K_{s,1}+K_{t,1} & 0 \\ -K_{s,2} & D_2K_{s,2} & 0 & K_{s,2}+K_{t,2} \end{bmatrix} \tag{2.6}$$

The vectors, $\ddot{u}_v$, $\dot{u}_v$ and u_v are vehicle accelerations, velocities and displacements respectively. The displacement vector of the vehicle is:

$$u_v = \{u_s, \theta_s, u_{u1}, u_{u2}\}^T \tag{2.7}$$

The time-varying dynamic interaction force vector is:

$$f_v = \{0,0,F_{t1},F_{t2}\}^T \tag{2.8}$$

The dynamic interaction force at wheel i is:

$$F_{ti} = K_{t,i} \times y_i \tag{2.9}$$

$i = 1,2$, where y_i is the road profile.

2.2.2 Road model

In this research, a 100 m road profile is generated by Monte Carlo simulation according to the ISO standard (ISO 8608: 1995). A class 'A' road is used which is a 'very good' profile and expected in a well-maintained highway. It has a geometric spatial mean of $16 \times 10^{-6} m^3/$ cycle. A moving average filter is applied to the generated road profile heights, y_i. It is over a distance of 0.24 m to simulate the attenuation of short wavelength disturbances by the tyre contact patch (Harris et al., 2007, OBrien et al., 2014).

2.3 Direct Solution of Profile Calculation

In vehicle-road-interaction, the forward problem uses the coupled vehicle-road model to find vehicle accelerations, velocities and displacements for a specified road profile. By contrast, the inverse problem takes measured accelerations from a vehicle traversing a road, $\ddot{u}$ and uses this signal to find the road profile. In previous research, the road profiles are back-calculated from vehicle-mounted sensor data (accelerations) using an optimisation procedure (OBrien and Keenahan, 2015). This method involves finding the profile elevations that give a best fit to the measured acceleration data. In this section, a new Inverse Newmark-Beta method is developed and used to solve the inverse problem of finding the road profile from vehicle acceleration histories. The dynamic systems are solved in MATLAB using the Newmark-Beta integration scheme for sprung mass and half-car models.

2.3.1 Sprung mass model

For the sprung mass vehicle, the inverse problem is solved using the Newmark-Beta method. A value of $\gamma = 0.8$ is used to ensure unconditional stability of the algorithm. In the Newmark-Beta method, the integration constants are listed:

Time step, $\Delta t = 0.001,\ \gamma = 0.8, \beta = 0.25 \times (0.5 + \gamma)^2$

$$a_0 = 1/(\beta \times \Delta t^2), \quad a_1 = \gamma/(\beta \times \Delta t), \quad a_2 = 1/(\beta \times \Delta t),$$

$$a_3 = 1/(\beta \times 2) - 1, a_4 = \gamma/\beta - 1, \tag{2.10}$$

$$a_5 = \Delta t/2 \times (\gamma/\beta - 2), a_6 = (1 - \gamma) \times \Delta t, a_7 = \gamma \times \Delta t$$

At the first time step, the mass, m, spring stiffness, k, time step, Δt, initial displacement and velocity of the mass, $u_0, \dot{u}_0$, are deemed to be known. The acceleration of the mass $\ddot{u}$ is measured so it is also known for each time step. Here the displacement and velocity of the mass at each time step can be calculated using the Newmark-Beta method:

$$u_{t+\Delta t} = (\ddot{u}_{t+\Delta t} + a_2 \times \dot{u}_t + a_3 \times \ddot{u}_t)/a_0 + u_t \tag{2.11}$$

$$\dot{u}_{t+\Delta t} = \dot{u}_t + a_6 \times \ddot{u}_t + a_7 \times \ddot{u}_{t+\Delta t} \tag{2.12}$$

Using the displacement, velocity and acceleration of the mass, the force being applied to the mass can be determined.

The effective stiffness matrix is found using:

$$\bar{K} = k + a_0 \times m \tag{2.13}$$

The effective force is found using:

$$\bar{F}_{t+\Delta t} = \bar{K} \times u_{t+\Delta t} \tag{2.14}$$

$$F_{t+\Delta t} = \bar{F}_{t+\Delta t} - m \times (a_0 \times u_t + a_2 \times \dot{u}_t + a_3 \times \ddot{u}_t) \tag{2.15}$$

Finally, the profile is calculated using:

$$y_{t+\Delta t} = F_{t+\Delta t}/k \tag{2.16}$$

Figure 2.3 shows a sample ‘calculated’ profile using this Inverse Newmark-Beta method, and the ‘true’ profile which was used to generate the accelerations in the forward problem. In both cases, the mass of the vehicle is 15 000 kg and stiffness of the spring is 3 500×10^3 N/m. The results clearly demonstrate that the calculated profile is the same as the ‘true’ profile.

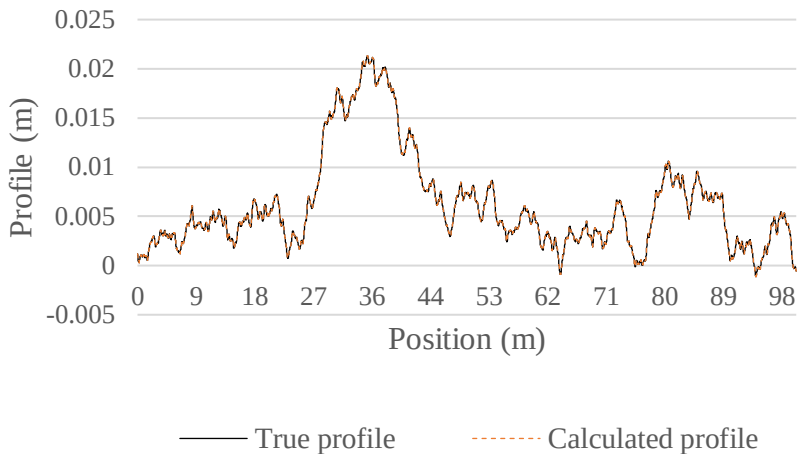

Figure 2.3 Calculated profile and true profile of sprung mass model.

2.3.2 Half-car model

In later simulations, the vehicle is represented with a half-car model, and the inverse problem is also solved using the Inverse Newmark-Beta method. The approach assumes knowledge of the sprung mass bounce acceleration, $\ddot{u}$, and the sprung mass pitch rotational velocity $\dot{\theta}_s$. Also, the vehicle properties M_v, C_v, K_v are taken to be known. Then, using the Newmark-Beta integration scheme, the displacement and velocity of the sprung mass can be calculated. The unsprung mass displacement can be calculated using the equations of motion of the sprung mass. Then, the acceleration and velocity of the unsprung mass can be found. Finally, using the Newmark-Beta integration scheme, the time varying interaction forces applied by the vehicle and the profile can be calculated. There are five steps in the process as follows:

Step 1:

Using the Newmark-Beta integration scheme, the sprung mass bounce displacement, u_s, and velocity, $\dot{u}_s$, sprung mass pitch rotational displacement, θ_s, and accelerations, $\ddot{\theta}_s$, can be calculated:

$$u_{s,t+\Delta t} = (\ddot{u}_{s,t+\Delta t} + a_2 \times \dot{u}_{s,t} + a_3 \times \ddot{u}_{s,t})/a_0 + u_{s,t} \tag{2.17}$$

$$\dot{u}_{s,t+\Delta t} = \dot{u}_{s,t} + a_6 \times \ddot{u}_{s,t} + a_7 \times \ddot{u}_{s,t+\Delta t} \tag{2.18}$$

$$\theta_{s,t+\Delta t} = (\dot{\theta}_{s,t+\Delta t} + a_4 \times \dot{\theta}_{s,t} + a_5 \times \ddot{\theta}_{s,t})/a_1 + \theta_{s,t} \tag{2.19}$$

$$\ddot{\theta}_{s,t+\Delta t} = a_0 \times (\theta_{s,t+\Delta t} - \theta_{s,t}) - a_2 \times \dot{\theta}_{s,t} - a_3 \times \ddot{\theta}_{s,t} \tag{2.20}$$

Step 2:

According to Equations (2.3) to (2.9), the equations of motion of the sprung mass can be found:

$$m_s \times \ddot{u}_{s,t+\Delta t} + \left(C_{s,1} + C_{s,2}\right) \times \dot{u}_{s,t+\Delta t} + (D_1 C_{s,1} - D_2 C_{s,2}) \times \dot{\theta}_{s,t+\Delta t} - C_{s,1} \times \dot{u}_{u1,t+\Delta t}$$

$$-C_{s,2} \times \dot{u}_{u2,t+\Delta t} + \left(K_{s,1} + K_{s,2}\right) \times u_{s,t+\Delta t} + (D_1 K_{s,1} - D_2 K_{s,2}) \times \theta_{s,t+\Delta t}$$

$$-K_{s,1} \times u_{u1,t+\Delta t} - K_{s,2} \times u_{u2,t+\Delta t} = 0 \tag{2.21}$$

$$I_s \times \ddot{\theta}_{s,t+\Delta t} + \left(D_1 C_{s,1} - D_2 C_{s,2}\right) \times \dot{u}_{s,t+\Delta t} + ({D_1}^2 C_{s,1} + {D_2}^2 C_{s,2}) \times \dot{\theta}_{s,t+\Delta t}$$

$$-D_1 C_{s,1} \times \dot{u}_{u1,t+\Delta t} + D_2 C_{s,2} \times \dot{u}_{u2,t+\Delta t} + \left(D_1 K_{s,1} - D_2 K_{s,2}\right) \times u_{s,t+\Delta t}$$

$$+({D_1}^2 K_{s,1} + {D_2}^2 K_{s,2}) \times \theta_{s,t+\Delta t} - D_1 K_{s,1} \times u_{u1,t+\Delta t} + D_2 K_{s,2} \times u_{u2,t+\Delta t} = 0$$

(2.22)

The terms, $\dot{u}_{u2,t+\Delta t}$ and $u_{u2,t+\Delta t}$ can be removed by combining Equations (2.22) with Equations (2.21), scaled by D_2:

$$\begin{aligned} D_2 m_s \times \ddot{u}_{s,t+\Delta t} &+ D_2\left(C_{s,1} + C_{s,2}\right) \times \dot{u}_{s,t+\Delta t} + D_2(D_1 C_{s,1} - D_2 C_{s,2}) \times \dot{\theta}_{s,t+\Delta t} \\ &+ D_2\left(K_{s,1} + K_{s,2}\right) \times u_{s,t+\Delta t} + D_2(D_1 K_{s,1} - D_2 K_{s,2}) \times \theta_{s,t+\Delta t} + I_s \times \ddot{u}_{s,t+\Delta t} \\ &+ \left(D_1 C_{s,1} - D_2 C_{s,2}\right) \times \dot{u}_{s,t+\Delta t} + ({D_1}^2 C_{s,1} + {D_2}^2 C_{s,2}) \times \dot{\theta}_{s,t+\Delta t} \\ &+ \left(D_1 K_{s,1} - D_2 K_{s,2}\right) \times u_{s,t+\Delta t} + ({D_1}^2 K_{s,1} + {D_2}^2 K_{s,2}) \times \theta_{s,t+\Delta t} \\ &= \left(D_2 C_{s,1} + D_1 C_{s,1}\right) \times \dot{u}_{u1,t+\Delta t} + (D_2 K_{s,1} + D_1 K_{s,1}) \times u_{u1,t+\Delta t} \end{aligned}$$

(2.23)

In the Newmark-Beta method,

$$\dot{u}_{u1,t+\Delta t} = a_1 \times (u_{u1,t+\Delta t} - u_{u1,t}) - a_4 \times \dot{u}_{u1,t} - a_5 \times \ddot{u}_{u1,t} \tag{2.24}$$

Substituting (2.24) into (2.23), the unsprung mass displacement can be found:

$$\begin{aligned} u_{u1,t+\Delta t} = \left(D_2 m_s \times \ddot{u}_{s,t+\Delta t} + I_s \times \ddot{\theta}_{s,t+\Delta t} + \left(D_2 C_{s,1} + D_1 C_{s,1}\right) \times \dot{u}_{s,t+\Delta t} + (D_2 D_1 C_{s,1} + \right. \\ {D_1}^2 C_{s,1}) \times \dot{\theta}_{s,t+\Delta t} + \left(D_2 K_{s,1} + D_1 K_{s,1}\right) \times u_{s,t+\Delta t} + (D_2 D_1 K_{s,1} + {D_1}^2 K_{s,1}) \times \theta_{s,t+\Delta t} + \\ \left(D_2 C_{s,1} + D_1 C_{s,1}\right) \times \left(a_1 \times u_{u1,t} + a_4 \times \dot{u}_{u1,t} + a_5 \times \ddot{u}_{u1,t}\right))/(D_2 K_{s,1} + D_1 K_{s,1} + \\ (D_2 C_{s,1} + D_1 C_{s,1}) \times a_1) \end{aligned} \tag{2.25}$$

Step 3:

Using the Newmark-Beta method, unsprung mass acceleration and velocity can be calculated:

$$\ddot{u}_{u1,t+\Delta t} = a_0 \times (u_{u1,t+\Delta t} - u_{u1,t}) - a_2 \times \dot{u}_{u1,t} - a_3 \times \ddot{u}_{u1,t} \tag{2.26}$$

$$\dot{u}_{u1,t+\Delta t} = \dot{u}_{u1,t} + a_6 \times \ddot{u}_{u1,t} + a_7 \times \ddot{u}_{u1,t+\Delta t} \tag{2.27}$$

Step 4:

Use Newmark-Beta to calculate $f_{v,t+\Delta t}$ at time step, $t + \Delta t$,

The effective stiffness matrix is:

$$\bar{K} = K_v + a_0 \times M_v + a_1 \times C_v \tag{2.28}$$

The effective force is:

$$\bar{f}_{v,t+\Delta t} = \bar{K} \times u_{v,t+\Delta t} \tag{2.29}$$

and,

$$f_{v,t+\Delta t} = \bar{f}_{v,t+\Delta t} - M_v \times \left(a_0 \times u_{v,t} + a_2 \times \dot{u}_{v,t} + a_3 \times \ddot{u}_{v,t}\right) - C_v \times (a_1 \times u_{v,t} + a_4 \times \dot{u}_{v,t} + a_5 \times \ddot{u}_{v,t}) \tag{2.30}$$

According to Equation (2.8), $f_{v,t+\Delta t} = \{0,0, F_{t1,t+\Delta t}, F_{t2,t+\Delta t}\}^T$, and $F_{ti,t+\Delta t}$ is known.

Step 5:

Finally, the profile can be calculated using Equation (2.9):

$$y_{i,t+\Delta t} = F_{ti,t+\Delta t}/K_{t,i} \tag{2.31}$$

Using this Inverse Newmark-Beta method, the profile can be calculated step by step. For a specified profile, the forward problem is used here to calculate the accelerations and rotational velocities in the usual way. All the vehicle property values are listed in Table 2.1. These accelerations and rotational velocities are then used as the 'measurements' in a test of the inverse problem. The inverse problem is solved to back-calculate the profile using these signals. Figure 2.4(a) presents the calculated profile and the true profile. Figure 2.4(b) shows a detail in the 45 m to 55 m zone. As expected, the results show that the profile is found with a high degree of accuracy. The profiles are calculated using this approach directly. However, in the optimisation method the profiles are split into a number of phases to be calculated separately

(OBrien and Keenahan, 2015). In each phase, a large population of unknows is generated and regenerated for many generations. This Inverse Newmark-Beta method is much more efficient than an optimisation algorithm and allows the calculation to be completed in a fraction of the time.

Table 2.1 Vehicle parameters of half-car model.

Property	Unit	Symbol	Value
Body mass	kg	m_s	16 200
Axle mass	kg	m_{u1}	700
		m_{u2}	1 100
Suspension stiffness	$\mathrm{Nm^{-1}}$	$K_{s,1}$	4×10^5
		$K_{s,2}$	1×10^6
Suspension damping	$\mathrm{N\ sm^{-1}}$	$C_{s,1}$	1×10^4
		$C_{s,2}$	2×10^4
Tyre stiffness	$\mathrm{Nm^{-1}}$	$K_{t,1}$	1.75×10^6
		$K_{t,2}$	3.5×10^6
Pitch moment of inertia	$\mathrm{kg\ m^2}$	I_s	93 457
Distance of axle to centre of gravity	m	D_1	2.375
		D_2	2.375

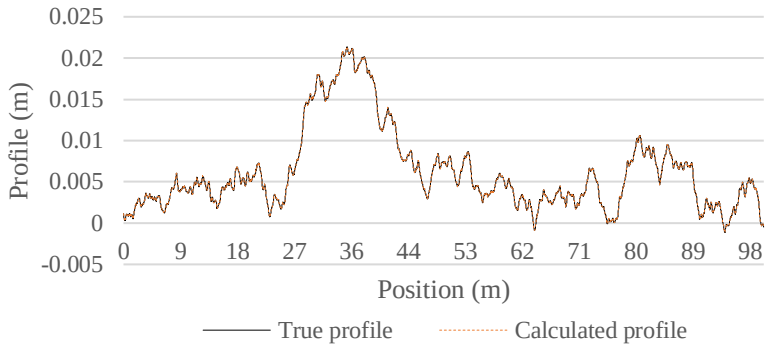

(a)

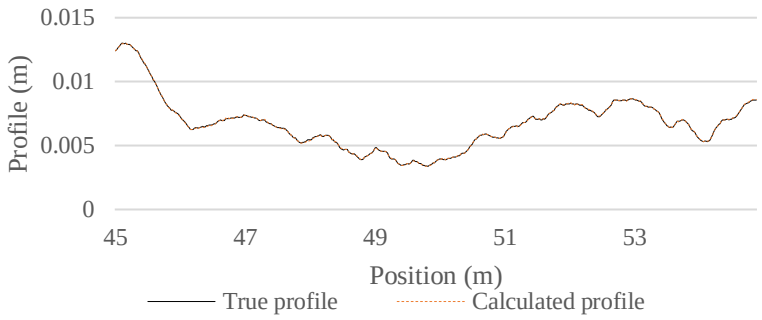

(b)

Figure 2.4 (a) Calculated profile and true profile of half-car model (0 to 100 m); (b) Calculated profile and true profile of half-car model (45 to 55 m).

2.4 Vehicle Fleet Monitoring Concept

It is shown in the previous section that road profiles can be found, knowing the vehicle accelerations and the vehicle properties. In this section, a vehicle fleet monitoring concept is introduced to calculate profiles from vehicle accelerations without prior knowledge of the vehicle properties. For a single vehicle, either the profile or the vehicle properties can be found, but not both. But all vehicles in a fleet are subject to the same profile. This feature is exploited here to find the profile. To solve the fleet problem, the Inverse Newmark-Beta method and the Cross Entropy (CE) optimisation technique are used together. Like the genetic algorithms (Goldberg and Holland, 1988) CE is a population-based method of optimisation (Rubinstein and Kroese, 2004). A population of trial solutions is generated randomly using Monte Carlo simulation. Each solution in the population is assessed and an 'elite set' of the best solution identified. Discarding all other solutions, the vector mean and standard deviation of the 'elite set' is used to generate a new population of solution and the process repeated until convergence.

It can occur that the CE algorithm converges prematurely and not converge to the true optimum. A method called 'injection' is used to address this problem, proposed by Botev and Kroese (2004). Injection resets the standard deviation in the Monte Carlo simulation to restart the algorithm. The first two injections reset the standard deviations at their initial values. Then the magnitude of the following ones decrease in inverse proportion to the number of injections (Casero et al., 2014).

The responses to a group of vehicles whose properties are unknown provide the data used in this method. Applying CE, a population of vehicle properties are randomly generated from a normal distribution. For each vehicle in this population, the responses are used to calculate the profile using the Inverse Newmark-Beta method. These calculated profiles will not, generally, be correct as incorrect vehicle properties have been used. However, the sets of properties for some vehicles will be better than for others and these can be identified as the corresponding profiles will be similar. The objective function for the j^{th} trial solution, O_j, is therefore the sum of squared differences of the profile its mean values.

$$O_j = \sum_i \sum_h \sum_k \left(r_{h,i,j,k} - \bar{r}_{h,j,k}\right)^2 \tag{2.32}$$

where $r_{h,i,j,k}$ is the k^{th} profile elevation in the j^{th} trial of h^{th} axle of the i^{th} vehicle's in the fleet and $\bar{r}_{h,j,k}$ is mean profile in the j^{th} trial of h^{th} axle of the n_i vehicles of the fleet:

$$\bar{r}_{h,j,k} = \frac{1}{n_i}\sum_i r_{h,i,j,k} \tag{2.33}$$

The objective functions are then ranked and the 10% best of the trial vehicle property sets are selected. Through the normal CE method, Monte Carlo simulation is used to generate the next generation of trial vehicle properties from the means and standard deviations of this elite set, μ and σ. Figure 2.5 illustrates the workflow of the algorithm presented in this chapter.

2.4.1 Results for sprung mass modal

For this investigation a very small population of just 6 vehicles is selected to illustrate the procedure ($n_i = 6$). The parameters for these 6 vehicles are chosen randomly and used in the forward problem to generate the responses that would be measured. The six sets of parameters are given in Table 2.2. Using these parameters, the forward problems are solved to determine the acceleration histories. These accelerations are used as inputs to solve vehicle fleet problem. The profile is calculated using these accelerations without knowledge of the vehicle properties.

Table 2.2 Ture vehicle parameters of sprung mass model

	Vehicle 1	Vehicle 2	Vehicle 3	Vehicle 4	Vehicle 5	Vehicle 6
m (kg)	15 614	12 365	18 115	13 081	13 609	13 975
k (N m^{-1})	2 655×10^3	4 138×10^3	2 123×10^3	4 402×10^3	1 108×10^3	1 917×10^3

The initial mean of mass and stiffness are 10 000 kg and 300×10^3 Nm^{-1} respectively. The calculated profiles are shown in Figure 2.6 and can be seen to be the same as the true profile. The calculated parameters (m and k) for the six vehicles are highly inaccurate, as shown in Table 2.3 (However m/k ratio is found with good accuracy).

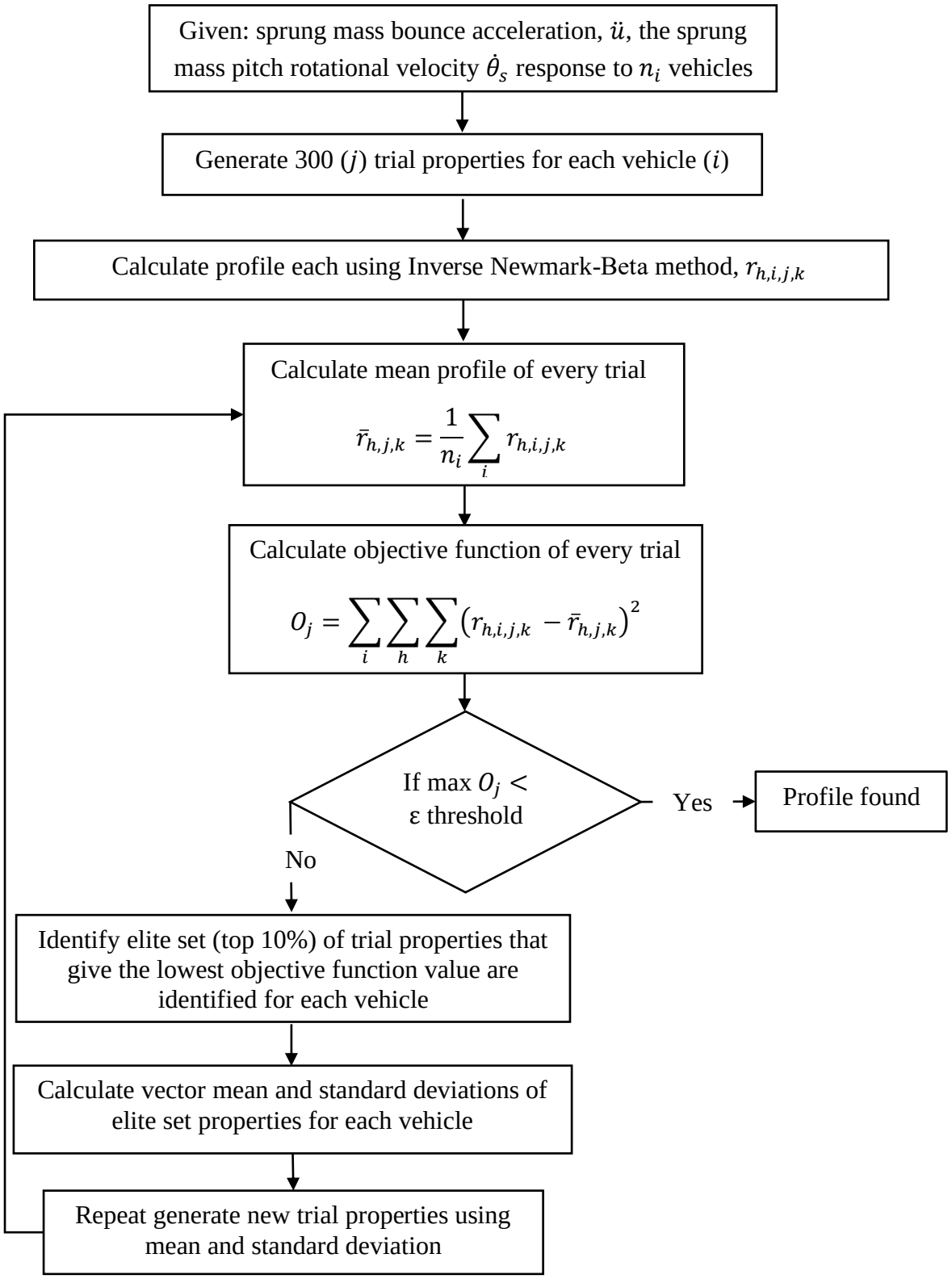

Figure 2.5 CE optimisation method algorithm.

Table 2.3 Inferred vehicle parameters of sprung mass model.

	True m (kg)	True k (Nm^{-1})	True ratio m/k	Inferred m (kg)	Inferred k (Nm^{-1})	Inferred ratio m/k
Vehicle 1	15 614	$2\,655\times10^3$	0.0059	2 098	356 920	0.0059
Vehicle 2	12 365	$4\,138\times10^3$	0.0030	1 933	645 469	0.0030
Vehicle 3	18 115	$2\,123\times10^3$	0.0085	4 221	495 372	0.0085
Vehicle 4	13 081	$4\,402\times10^3$	0.0030	1 663	558 487	0.0030
Vehicle 5	13 609	$1\,108\times10^3$	0.0123	5 524	449 414	0.0123
Vehicle 6	13 975	$1\,917\times10^3$	0.0073	3 832	523 167	0.0073

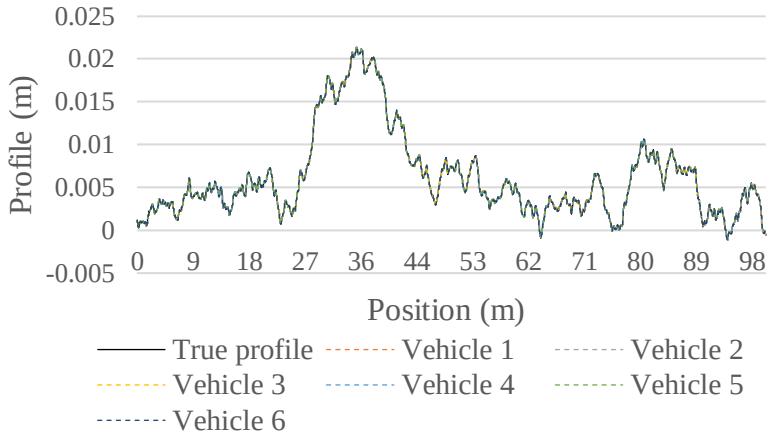

Figure 2.6 True profile and calculated profiles for sprung mass vehicles of the fleet.

To investigate the sensitivity issue, different vehicle fleets are generated. Accelerations are calculated by the forward problem in the vicinity of the true (m_0', k_0') pair of $(14\,000, 3.5 \times 10^6)$ whose m_0'/k_0' ratio is 0.0040. Four vehicles near incorrect pairs (m_0, k_0) are generated, $(m_0 + \Delta m, k_0), (m_0, k_0 - \Delta k), (m_0 - \Delta m, k_0), (m_0, k_0 + \Delta k)$, where $\Delta m = 1\,000$ kg and Δk=100 000 Nm^{-1}. The incorrect pairs are generated by varying the mass, m_0, from 11 000 kg through 20 000 kg in increments of 1 000 kg and the stiffness k_0 is generated in the immediate vicinity from 3.2×10^6 Nm^{-1} through 5×10^6 Nm^{-1} in increments of 200 000 Nm^{-1}. For the true vehicle properties, four (approximately) true vehicle signals are generated, corresponding to, $(m_0' + \Delta m, k_0'), (m_0', k_0' - \Delta k), (m_0' - \Delta m, k_0'), (m_0', k_0' + \Delta k)$. All other vehicle property points, (m_0, k_0) are incorrect and are used to assess the sensitivity of the result to their incorrect values. For each small fleet in the vicinity of the incorrect pair, the profiles are calculated. Contours are plotted in Figure 2.7 of the Root Mean Square (RMS) difference between the calculated profiles and their mean.

It can be seen that there are equally good solutions for all (m_0, k_0) pairs for which the m_0/k_0 ratio is 0.0040, showing that there is insufficient information to find unique value for m_0 and k_0. Two points are chosen to explain the issue. In each case, the inverse problem is solved to find the profiles. Point A is $(18\,000, 4.5 \times 10^6)$ and has the same m_0/k_0 ratio as the true vehicle. Point B $(13\,000, 3.8 \times 10^6)$, on the other hand, has a different m_0/k_0 ratio. The calculated profiles and true profiles (0 to 100 m) are shown in Figures 2.8(a) and 2.9(a). Figures 2.8(b) and 2.9(b) show the detail in the 45 m to 55 m zone. The profile calculated at Point A is very similar to the true profile even though the m and k values are incorrect. The profile calculated at Point B is different from true profile and significantly, the 4 profiles are different from each other.

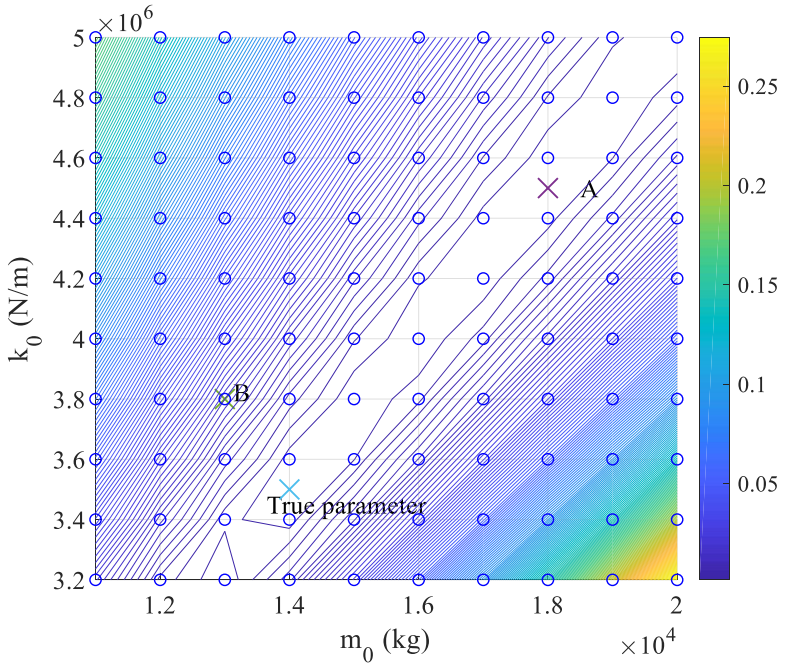

Figure 2.7 RMS difference between the calculated profiles and their mean.

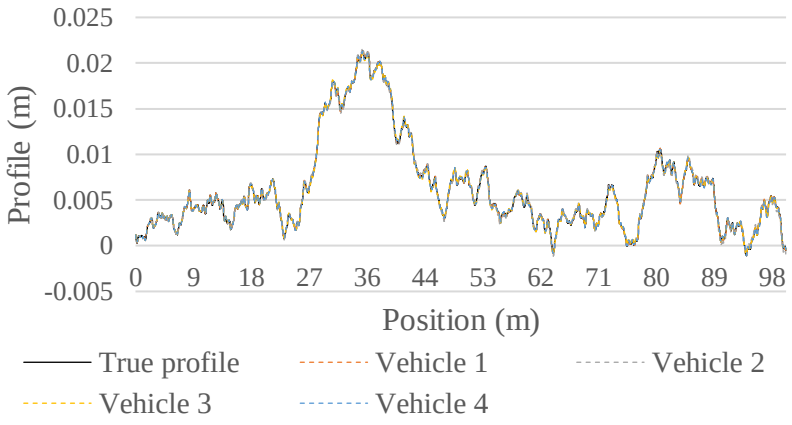

(a)

Figure 2.8 Calculated and true profiles (continued on next page).

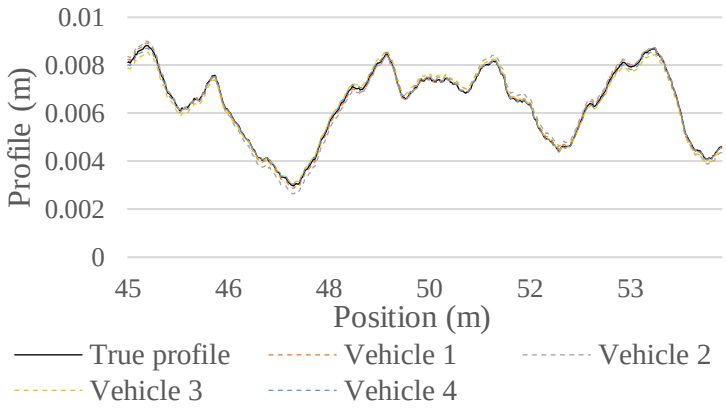

(b)

Figure 2.8 Calculated and true profiles (continued from previous page) (a) Point A (0 to 100 m); (b) Point A (45 to 55 m).

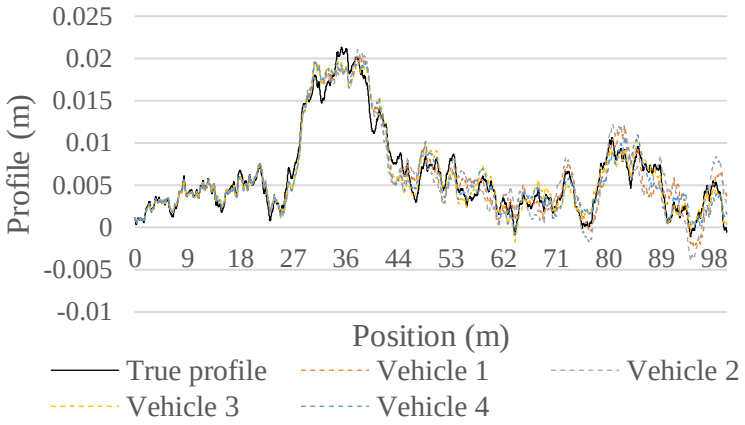

(a)

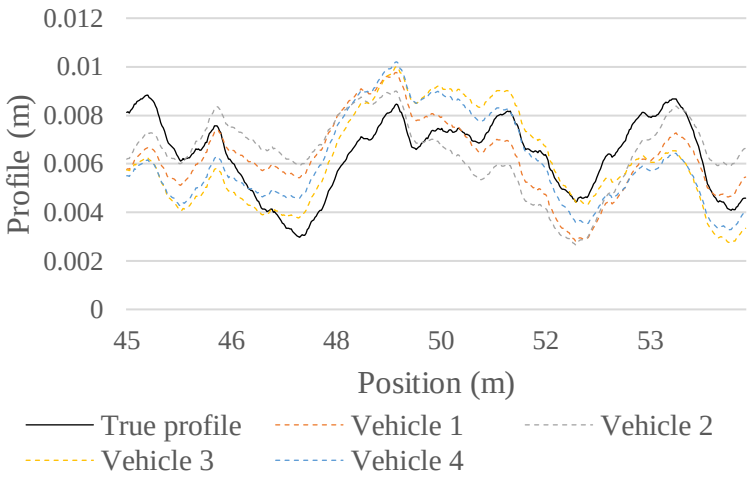

(b)

Figure 2.9 Calculated profile and true profile (a) Point B (0 to 100 m); (b) Point B (45 to 55 m).

2.4.2 Results for half-car model

The half-car model is further used to investigate the vehicle fleet concept. Vehicle properties for a fleet of six vehicles are randomly generated and are shown in Table 2.4. The forward problems are calculated to get sprung mass bounce acceleration and sprung mass pitch rotational velocity. From this the vehicle fleet problem is solved using these acceleration and velocity histories. The initial values for the properties of all vehicles are also shown in the table. The calculated profiles are shown in Figure 2.10. Figure 2.10(a) is the calculated profile under 1st axle of Vehicle 1 and the true profile. A detail in the 45 m to 55 m zone is shown in Figure 2.10(b). The calculated profiles 1st axle of all six vehicles in the fleet and the true profile as shown in Figure 2.10(c).

Table 2.4 Vehicle parameters and initial values of half car model.

Parameters	Vehicle 1	Vehicle 2	Vehicle 3	Vehicle 4	Vehicle 5	Vehicle 6	Initial values
I_s (kg m^2)	89 415	77 891	94 629	96 146	82 743	104587	80 000
m_s (kg)	15 499	13 502	16 403	16 666	14 343	18 129	10000
$m_{u,1}$ (kg)	783	697	723	712	687	751	500
$m_{u,2}$ (kg)	1 035	1 340	1 085	1 113	1 217	1 107	800
$K_{s,1}$ (Nm^{-1})	384005	427600	432 625	428 476	451 610	426 744	300 000
$K_{s,2}$ (Nm^{-1})	1 119 084	879 754	998 021	984 328	839 591	1 025 730	800 000
$K_{t,1}$ (Nm^{-1})	1 733 740	1 608 501	1 800 050	1 522 849	1 871 435	2 026 006	1 000 000
$K_{t,2}$ (Nm^{-1})	3 257 879	3 800 299	3 938 900	2 942 195	2 995 662	3 699 902	3 000 000
$C_{s,1}$ (N sm^{-1})	8 944	11415	9195	10 529	10 219	9 078	9 000
$C_{s,2}$ (N sm^{-1})	15 659	19 882	17 979	21 229	21 015	23 385	10 000
D_1 (m)	2.375	2.375	2.375	2.375	2.375	2.375	2
D_2 (m)	2.375	2.375	2.375	2.375	2.375	2.375	2

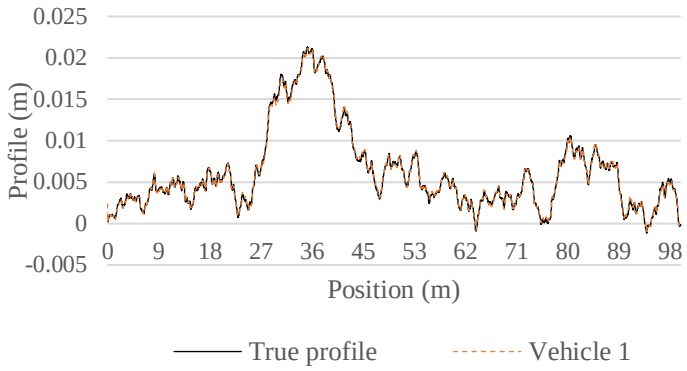

(a)

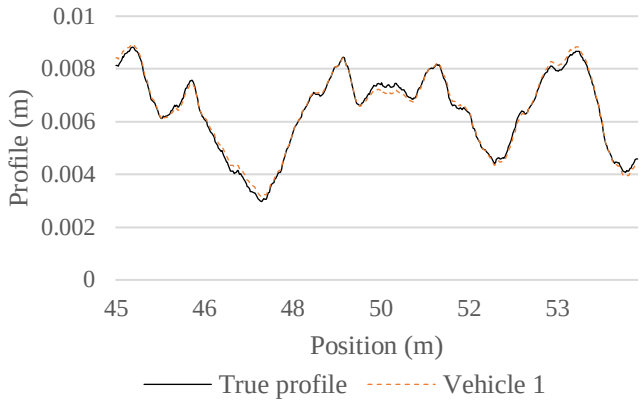

(b)

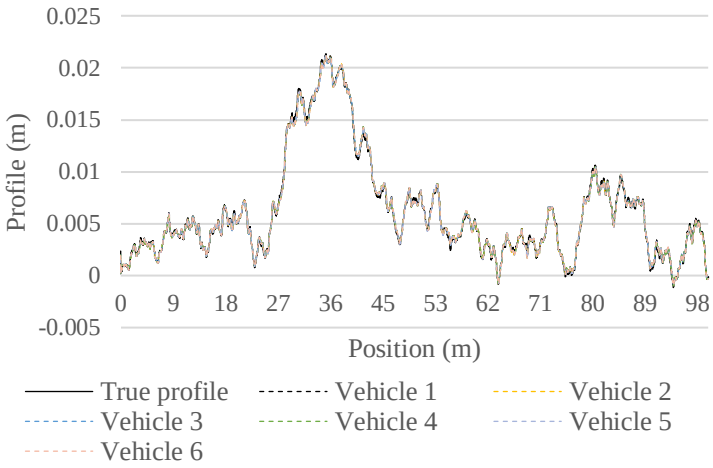

(c)

Figure 2.10 (a) Calculated profiles under 1st axle of vehicle 1 and true profile (0 to 100 m); (b) Calculated profiles under 1st axle of vehicle 1 and true profile (45 to 55 m); (c) Calculated profiles under 1st axle of vehicle 1 to 6 and true profile (0 to 100 m).

Table 2.5 shows the calculated vehicle properties. Like the sprung mass model results, the calculated vehicle properties are quite inaccurate, though the calculated profiles are close to the 'true' profile. However, as for the sprung mass model results, the calculated ratios of vehicle properties to sprung mass can be calculated with good accuracy. This is shown in Table 2.6 which compares the estimates to the true property ratios.

Table 2.5 Calculated vehicle parameters of half car model

Parameters	Vehicle 1	Vehicle 2	Vehicle 3	Vehicle 4	Vehicle 5	Vehicle 6
I_s (kg m^2)	65 728	60 306	68 852	71 545	64 244	73 364
m_s (kg)	11 229	10 305	11 725	12 252	10 992	12 508
$m_{u,1}$ (kg)	533	504	477	506	480	467
$m_{u,2}$ (kg)	764	1 020	800	806	915	766
$K_{s,1}$ (Nm^{-1})	314 279	367 754	349 669	355 918	387 510	329 456
$K_{s,2}$ (Nm^{-1})	771 019	646 553	680 329	692 506	618 190	679 566
$K_{t,1}$ (Nm^{-1})	1 091 012	1 086 072	1 115 952	996 029	1 252 653	1 203 506
$K_{t,2}$ (Nm^{-1})	2 480 437	2 951 608	2 979 044	2 188 401	2 296 541	2 625 069
$C_{s,1}$ (N sm^{-1})	7 956	10 623	8 065	9 571	9 385	7 531
$C_{s,2}$ (N sm^{-1})	10 989	14 875	12 473	15 192	15 807	15 725
D_1 (m)	2.23	2.25	2.24	2.24	2.26	2.25
D_2 (m)	2.46	2.46	2.46	2.46	2.46	2.46

Table 2.6 Calculated and true vehicle properties ratios of half car model

Ratio	Vehicle 1		Vehicle 2		Vehicle 3	
	Calculated	**True**	**Calculated**	**True**	**Calculated**	**True**
I_s / m_s	5.85	5.77	5.85	5.77	5.87	5.77
$m_{u,1} / m_s$	0.048	0.051	0.049	0.052	0.041	0.044
$m_{u,2} / m_s$	0.068	0.067	0.099	0.099	0.068	0.066
$K_{s,1} / m_s$	28.0	24.8	35.7	31.7	29.8	26.4
$K_{s,2} / m_s$	68.7	72.2	62.7	65.2	58.0	60.8
$K_{t,1} / m_s$	97.2	111.9	105.4	119.1	95.2	109.7
$K_{t,2} / m_s$	220.9	210.2	286.4	281.5	254.1	240.1
$C_{s,1} / m_s$	0.71	0.58	1.03	0.85	0.69	0.56
$C_{s,2} / m_s$	0.98	1.01	1.44	1.47	1.06	1.10
D_1 / m_s	0.00020	0.00015	0.00022	0.00018	0.00019	0.00014
D_2 / m_s	0.00022	0.00015	0.00024	0.00018	0.00021	0.00014

Ratio	Vehicle 4		Vehicle 5		Vehicle 6	
	Calculated	**True**	**Calculated**	**True**	**Calculated**	**True**
I_s / m_s	5.84	5.77	5.84	5.77	5.87	5.77
$m_{u,1} / m_s$	0.041	0.043	0.044	0.048	0.037	0.041
$m_{u,2} / m_s$	0.066	0.067	0.083	0.085	0.061	0.061
$K_{s,1} / m_s$	29.1	25.7	35.3	31.5	26.3	23.5
$K_{s,2} / m_s$	56.5	59.1	56.2	58.5	54.3	56.6
$K_{t,1} / m_s$	81.3	91.4	114.0	130.5	96.2	111.8
$K_{t,2} / m_s$	178.6	176.5	208.9	208.9	209.9	204.1
$C_{s,1} / m_s$	0.78	0.63	0.85	0.71	0.60	0.50
$C_{s,2} / m_s$	1.24	1.27	1.44	1.47	1.26	1.29
D_1 / m_s	0.00018	0.00014	0.00021	0.00017	0.00018	0.00013
D_2 / m_s	0.00020	0.00014	0.00022	0.00017	0.00020	0.00013

2.4.3 Implications of noise in measurements

In this section, Additive White Gaussian Noise (AWGN) is added to allow for inaccuracy in the acceleration and velocity measurements. Noise is added to the measurements according to Equation (2.34) (Lyons, 2011):

$$A_{polluted} = A + E_{noise} \times Noise \tag{2.34}$$

where $A_{polluted}$ is the signal with noise, A is the original signal without noise, $Noise$ is a standard normal distribution vector with zero mean and unit standard deviation and E_{noise}^2 is the square of the energy in the noise. The E_{noise}^2 is calculated from the definition of the Signal to Noise Ratio (*SNR*) given by Equation (2.35):

$$SNR = 10\, log_{10} \frac{var(A)}{E_{noise}^2} \tag{2.35}$$

which is the ratio of the power in the signal to the power in the noise, where $var(A)$ is the variance of the signal.

Here, the 'measured' acceleration and velocity are contaminated assuming 1% noise (*SNR*=100). Figure 2.11 (a) shows the calculated profile under 1st axle of Vehicle 1 while Figure 2.11 (b) shows the calculated profiles for all six vehicles in the fleet. A detail in the 45 m and 55 m zone is shown in Figure 2.11 (c). The true profile is also shown in all figures. While the noise clearly has an influence, the calculated profile is reasonably close to the true one. Figure 2.11 (b) shows that the profiles inferred from the population of six vehicles are similar. This is a feature of the strategy described in Equation (2.32), namely, that similar profiles are assumed to be more likely to be correct. Furthermore, different levels of noise are added to measurements to study its effects. The calculated profiles are determined and analysed by Root Mean Square Error (RMSE). The RMSE for each calculated profile under different noise are calculated using the equation:

$$RMSE = \sqrt{\frac{1}{M}\sum_{k=1}^{M}(r_{true,k} - \bar{r}_{calculated,k})^2} \tag{2.36}$$

where $r_{true,k}$ is the true profile at the k^{th} point, $\bar{r}_{calculated,k}$ is the mean of 6 calculated profiles at the k^{th} point. Both are the profile under 1st axle of the half car model. RMS errors for different noise levels are calculated using this equation and the results are shown in Figure 2.12. It can be seen that the RMS errors increase with increasing noise level, but a reasonable level of accuracy is maintained. It is felt by the authors that the influence of noise will be much reduced when larger populations are considered.

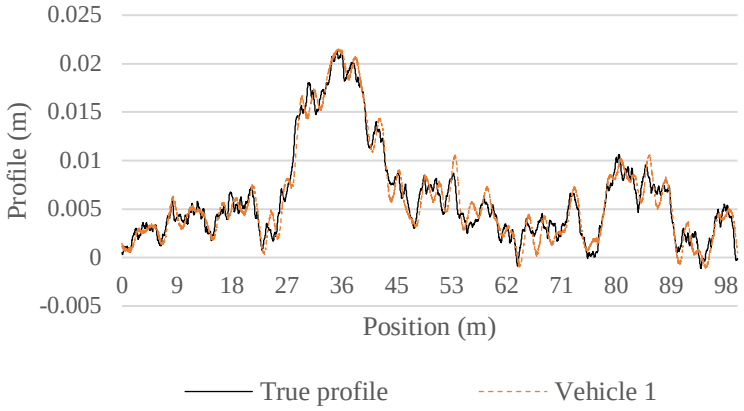

(a)

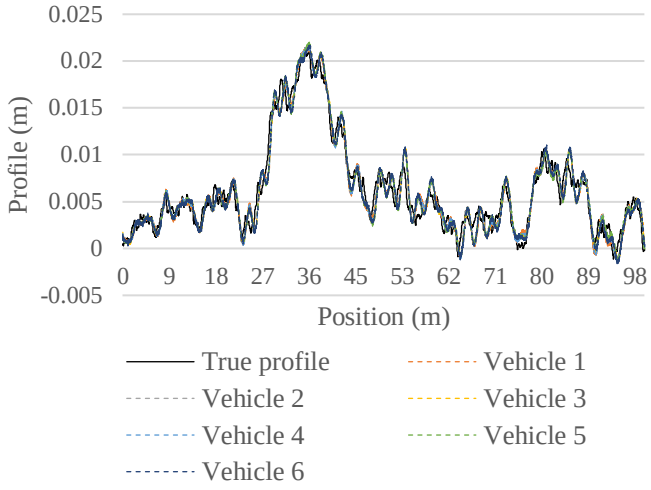

(b)

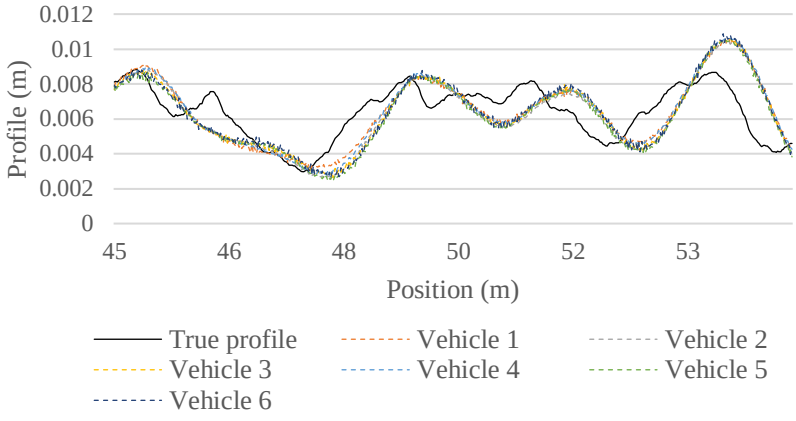

(c)

Figure 2.11 (a) Calculated profiles under 1st axle of vehicle 1 and true profile in the presence of noise; (b) Calculated profiles under 1st axle of vehicle 1 to 6 and true profile in the presence of noise (0 to 100 m); (c) Calculated profiles under 1st axle of vehicle 1 to 6 and true profile in the presence of noise (45 to 55m).

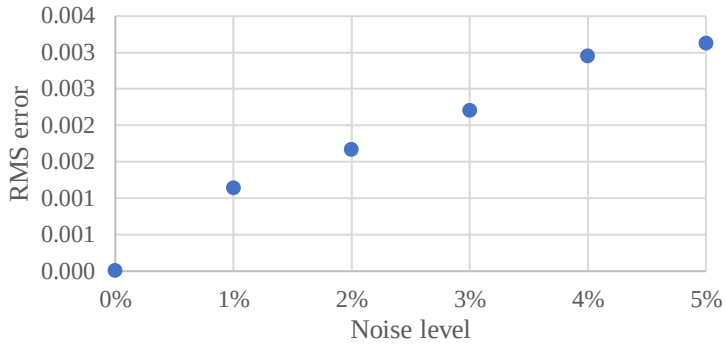

Figure 2.12 RMS errors of calculated profile for different noise levels.

2.5 Conclusions and Future Work

This chapter introduces a novel method of inferring road or rail surface profiles from inertial measurements. A new Inverse Newmark-Beta method is proposed to determine the profiles using accelerations measured in passing vehicles. The acceleration histories are simulated here using a vehicle/road dynamic interaction model. Sprung mass and half-car models are tested separately. The results show that the calculated profiles are the same as the true profiles used in the forward problem to generate the accelerations. The Inverse Newmark-Beta method is much more efficient than optimization and allows the calculation to be completed rapidly.

The work is expanded to introduce the concept of using a fleet of vehicles to determine a profile. Using several vehicles, the profiles can be calculated without prior knowledge of the vehicle properties in a process that combines the Inverse Newmark-Beta method with CE optimisation. The results show that the algorithm is successful in predicting profiles that are similar to the true profile. The vehicle properties are inaccurate when estimated from the road profile, but the properties ratios are accurately captured, which results in good accuracy for road profile estimation. To process data from a vehicle fleet will require the solution of an inverse dynamics problem, the calibration of a fleet of vehicles and the use of the database of accelerations to determine bridge conditions in the future.

The scanning frequency used here is high and gives an accurate result. For a lower scanning frequency, there is a risk that it could be less effective for a profile of given length, which may reduce the accuracy of the result. The scanning frequency depends on the devices (sensors) used in practice. It is not clear what scanning frequency is best. A frequency of 500 Hz is commonly used for drive-by monitoring. This may represent a challenge for data storage. The accuracy implications of different scanning frequencies should be investigated further in the future.

Chapter 3 – Detecting Railway Bridge Damage Using Numerically Calculated Responses from Batches of Trains

Authors:

Yifei Ren

Eugene J. OBrien

Daniel Cantero

Jennifer Keenahan

Paper Status:

Published in *Applied Sciences* (2022), 12, 4972.

Note to the Reader:

The work in this chapter is largely the work of the author, under the supervision of Prof. OBrien and Dr. Keenahan. Dr. Cantero developed the model used in the 'blind' test and subsequently provided the acceleration and velocity signals for the test.

Chapter 3 – Detecting Railway Bridge Damage Using Numerically Calculated Responses from Batches of Trains

3.1 Introduction

Traditional monitoring of railway infrastructure involves on-track visual inspections or specialist Track Recording Vehicles (TRVs). Neither approach is entirely satisfactory due to issues of cost, safety, and speed of implementation. The vehicle-based techniques have long been used to detect the geometrical properties of the track, such as profile and rail condition (Weston et al., 2015, Yang et al., 2020a). Specialist TRVs are used for this purpose in accordance with European Standard EN 13848 (2018) but are expensive and may disrupt scheduled services. Using in-service vehicles to provide data for railway infrastructure maintenance managers has the potential to complement or replace TRV data and has the advantage of providing real-time information at a much-reduced cost.

Cantero and Basu (2015) propose a wavelet-based assessment methodology to detect local track irregularities using accelerations measured in moving vehicles. A wavelet-based indicator is proposed to facilitate recognition of deteriorated segments. OBrien et al. (2016) develop a method to determine the longitudinal profile using bogie vertical accelerations and angular velocities resulting from train/track dynamic interaction. The railway track profile elevations, determined by Cross Entropy (CE) optimisation, are those that generate a vehicle response which best fits the measurements in a railway carriage bogie. Yang et al. (2020b) develop an effective technique to identify the track modulus, i.e., the foundation stiffness of the rails, using the contact-point response of a moving test vehicle. It is shown that the track modulus can be successfully identified via the first rail frequency extracted from the contact-point response.

The drive-by method is examined by field test in some research. The numerical method developed in OBrien et al. (2016) subsequently tested in the field by OBrien et al. (2017). A good match is achieved between the inferred longitudinal profiles and the surveyed track profile. Wei et al. (2016) use bogie and the car body acceleration sensors to estimate track irregularities. The acceleration signals are pre-processed with filters. Subsequently, the track alignments are obtained by double integration of the signals. Field tests were carried out on the Shanghai metro Line 1 to demonstrate the effectiveness of the proposed track inspection system. Paixao et al. (2019) use a smartphone to obtain constant acceleration measurements on in-

service trains to assess structural performance and geometrical degradation of the tracks. Cross-correlation values were obtained between the standard deviations of the longitudinal level and the measured vertical accelerations and are proposed as a means to identify critical situations that affect the performance of the track.

The drive-by method of bridge health monitoring has advantages compared with the conventional direct monitoring approach. It is mobile, economic, and efficient (Yang and Yang, 2018). Malekjafarian et al. (2015) review drive-by, also known as indirect, methods of monitoring highway bridges. Most methods are based on the identification of dynamic characteristics of the bridge from responses measured in the vehicle, such as natural frequencies, mode shapes, and damping (Yang et al., 2004, Zhang et al., 2012, Gonzalez et al., 2012). Some methods detect bridge damage directly from the interaction between the vehicle and bridge without using the conventional structural dynamic properties. OBrien and Keenahan (2015) use CE optimisation to determine the Apparent Profile (AP), where the displacements recorded by the sensors are used as the inputs. The time-shifted difference in the AP is proposed to detect bridge damage and numerical results show that it has good potential as a damage indicator. Elhattab et al. (2016) calculate APs from on-board sensors and then subtract them to calculate the 'bridge displacement profile difference' (BDPD) which is proposed as another bridge damage indicator. Keenahan and OBrien (2018) used a Traffic Speed Deflectometer (TSD) to detect damage in bridges. The data gathered from the TSD are post-processed and time-shifted curvature, without pitch, is used as the damage indicator. Time-shifted curvature is derived from the displacements and is proposed as a novel damage indicator, which removes the influence of the road profile and all vehicle motions except for pitch.

For railway bridges, Quirke et al. (2017) detect damage through comparison of APs sensed by the passing vehicle. The APs are calculated using the CE optimisation method that generates a vehicle dynamic response most similar to the measured input. APs for a number of damage scenarios are inferred and compared over time to detect damage. Fitzgerald et al. (2019) develop a method to detect the presence of railway bridge scour using bogie acceleration measurements from a passing train. A scour indicator is defined as the difference in average Continuous Wavelet Transform coefficients between healthy and scoured batches of train crossings. The result shows that this indicator is quite effective at detecting the presence of scour and its location.

Some field tests of railway bridge monitoring using onboard train measurements are introduced in the following papers. Various tests have been conducted at the Bridge Deflection Test Facility (BDTF) at the Transportation Technology Center, USA. A track deflection measurement system (TDMS) and a track geometry measurement system (TGMS) have been tested on different trains. They investigate the potential for using onboard technology to detect bridge impairment or changes in bridge behaviour (Rakoczy et al., 2016). Rakoczy et al. (2017) present simulation and field test results of a freight car and locomotive running on a railway bridge. Simulations and tests are used to improve the onboard measurement capability of such a system and the new configuration of accelerometers is shown to provide useful results for bridge condition evaluations. Displacements are derived from the acceleration data. Then, the results from different bridge conditions are compared and relative deflections calculated to identify the change in bridge condition. Micu et al. (2022) introduce a field study of drive-by bridge monitoring using acceleration measurements on an instrumented train. The dynamic responses of the train signals are used to detect the existence and location of a stiffer part of the viaduct where two spans were replaced. The results show that instrumented trains can be successfully used to monitor bridge condition and to identify a need for repair or rehabilitation.

This chapter presents a novel method of determining AP of the track and detecting bridge damage using batches of trains. In this context, AP is deemed to include the unloaded surface profile and the deflections of the track under the applied train load. Firstly, an Inverse Newmark-Beta algorithm is introduced to calculate AP from a train measurement. Following this, the concept of using a batch of trains is introduced to find the profile, without prior knowledge of the train masses and velocities. This is effectively a train self-calibration process, using the train responses. Moving reference influence lines are calculated from APs of the bridge which are shown to be a good indication of bridge behaviour and condition. A blind test is used to validate these methods: bridge damage is calculated for simulated data provided by an independent laboratory, without prior knowledge of the damage levels used in the simulations.

3.2 Model Description

In this research, the vehicle is simulated crossing the track and bridge in a train–track–bridge (TTB) dynamic system. More detailed information of TTB systems is available in (Cantero et al., 2016). This model is used by the Norwegian team to provide simulated measured data for the blind test. It is described briefly in this section.

3.2.1 Vehicle model

The train is represented by the two-dimensional (2D) 4-axle railway carriage model shown in Figure 3.1. The vehicle model includes lumped masses, rigid bars, springs and dampers. There are 10 degrees of freedom (DOFs) in this vehicle model: vertical translation and rotation about the centre of gravity for the car body and bogies, and vertical translation for each wheelset. The wheels are fixed to the track with no separation being permitted. This reduces the system to 6 DOFs. In this model, each wheel is modelled with a mass (m_w). It is connected to the bogie by a primary suspension represented by a spring (k_p) and a viscous damper (c_p) in parallel. The bogies are represented as rigid bars with mass (m_b) and moment of inertia (I_b), while the main body of the vehicle is also represented as a rigid bar with mass (m_v) and moment of inertia (I_v). Springs (k_s) and dampers (c_s) represent the secondary suspensions to connect the bogies to the main body. The distances between the car body centre of mass and the bogie pivots are L_{v1} and L_{v2}. Similarly, L_{b1}, L_{b2}, L_{b3}, L_{b4} are the distances between the bogie centres of mass and the wheels. Vehicle models of this type have been used in many studies (Lei and Noda, 2002, Lou, 2007).

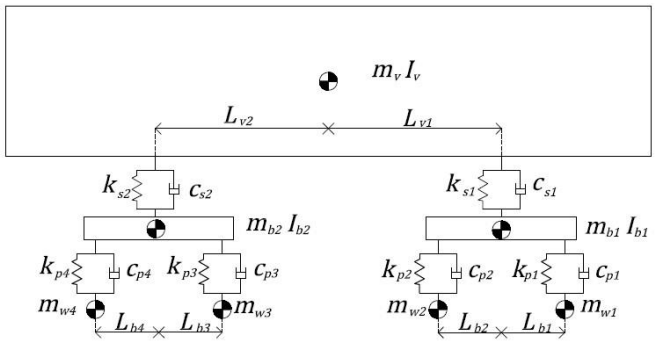

Figure 3.1 Two-dimensional (2D) 4-axle railway carriage model.

Assuming small rotations, a linearised system of equations of motion is adopted (Nguyen et al., 2012) and can be expressed in matrix form:

$$M_v\ddot{u}+C_v\dot{u}+K_vu = F \tag{3.1}$$

where M_v, C_v and K_v are the mass, damping and stiffness matrices of the vehicle, respectively. The vectors $\ddot{u}$, $\dot{u}$ and u represent the vehicle accelerations, velocities, and displacements, respectively and F contains the external forces applied to the vehicle. All matrices and vectors are introduced in the following equations:

$$\ddot{u} = \begin{Bmatrix} \ddot{u}_v \\ \ddot{u}_{b1} \\ \ddot{u}_{b2} \\ \ddot{\theta}_v \\ \ddot{\theta}_{b1} \\ \ddot{\theta}_{b2} \end{Bmatrix} \tag{3.2}$$

$$\dot{u} = \begin{Bmatrix} \dot{u}_v \\ \dot{u}_{b1} \\ \dot{u}_{b2} \\ \dot{\theta}_v \\ \dot{\theta}_{b1} \\ \dot{\theta}_{b2} \end{Bmatrix} \tag{3.3}$$

$$u = \begin{Bmatrix} u_v \\ u_{b1} \\ u_{b2} \\ \theta_v \\ \theta_{b1} \\ \theta_{b2} \end{Bmatrix} \tag{3.4}$$

$$F = \begin{Bmatrix} m_v g \\ m_{b1} g + k_{p1} r_{w1} + c_{p1} r'_{w1} + k_{p2} r_{w2} + c_{p2} r'_{w2} \\ m_{b2} g + k_{p3} r_{w3} + c_{p3} r'_{w3} + k_{p4} r_{w4} + c_{p4} r'_{w4} \\ 0 \\ L_{b11}\left(k_{p1} r_{w1} + c_{p1} r'_{w1}\right) - L_{b12}(k_{p2} r_{w2} + c_{p2} r'_{w2}) \\ L_{b21}\left(k_{p3} r_{w3} + c_{p3} r'_{w3}\right) - L_{b22}(k_{p4} r_{w4} + c_{p4} r'_{w4}) \end{Bmatrix} \tag{3.5}$$

$$M_v = diag[m_v \quad m_{b1} \quad m_{b2} \quad J_v \quad J_{b1} \quad J_{b2}] \tag{3.6}$$

$$K_v = \begin{bmatrix} k_{s1}+k_{s2} & -k_{s1} & -k_{s2} & L_{v1}k_{s1}-L_{v2}k_{s2} & 0 & 0 \\ -k_{s1} & k_{p1}+k_{p2}+k_{s1} & 0 & -L_{v1}k_{s1} & L_{b11}k_{p1}-L_{b12}k_{p2} & 0 \\ -k_{s2} & 0 & k_{p3}+k_{p4}+k_{s2} & L_{v2}k_{s2} & 0 & L_{b21}k_{p3}-L_{b22}k_{p4} \\ L_{v1}k_{s1}-L_{v2}k_{s2} & -L_{v1}k_{s1} & L_{v2}k_{s2} & {L_{v1}}^2k_{s1}+{L_{v2}}^2k_{s2} & 0 & 0 \\ 0 & L_{b11}k_{p1}-L_{b12}k_{p2} & 0 & 0 & {L_{b11}}^2k_{p1}+{L_{b12}}^2k_{p2} & 0 \\ 0 & 0 & L_{b21}k_{p3}-L_{b22}k_{p4} & 0 & 0 & {L_{b21}}^2k_{p3}+{L_{b22}}^2k_{p4} \end{bmatrix} \tag{3.7}$$

$$C_v = \begin{bmatrix} c_{s1}+c_{s2} & -c_{s1} & -c_{s2} & L_{v1}c_{s1}-L_{v2}c_{s2} & 0 & 0 \\ -c_{s1} & c_{p1}+c_{p2}+c_{s1} & 0 & -L_{v1}c_{s1} & L_{b11}c_{p1}-L_{b12}c_{p2} & 0 \\ -c_{s2} & 0 & c_{p3}+c_{p4}+c_{s2} & L_{v2}c_{s2} & 0 & L_{b21}c_{p3}-L_{b22}c_{p4} \\ L_{v1}c_{s1}-L_{v2}c_{s2} & -L_{v1}c_{s1} & L_{v2}c_{s2} & {L_{v1}}^2c_{s1}+{L_{v2}}^2c_{s2} & 0 & 0 \\ 0 & L_{b11}c_{p1}-L_{b12}c_{p2} & 0 & 0 & {L_{b11}}^2c_{p1}+{L_{b12}}^2c_{p2} & 0 \\ 0 & 0 & L_{b21}c_{p3}-L_{b22}c_{p4} & 0 & 0 & {L_{b21}}^2c_{p3}+{L_{b22}}^2c_{p4} \end{bmatrix} \tag{3.8}$$

3.2.2 Track model

The track is modelled as a beam supported on spaced sprung mass systems (Figure 3.2) corresponding to the railway sleepers. The rail is modelled by beam elements in a Finite Element framework. In this three-layer sprung mass system, the masses represent the sleeper, m_S and ballast, m_{BA}. The various layers are connected by pad, ballast and sub-ballast, spring and damping systems with respective properties: k_P and c_P; k_{BA} and c_{BA}; and k_{SB} and c_{SB}. A surface profile is included on the track. Similar models have been used by other researchers (Lu et al., 2008, Zhai et al., 2004).

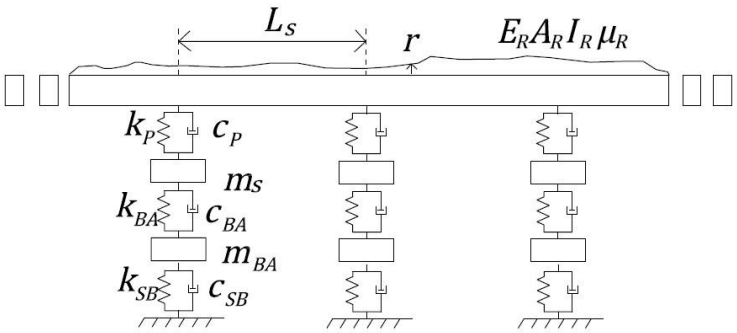

Figure 3.2 Track model.

3.2.3 Bridge model

The bridge/culvert is modelled using a Finite Element discretization (Figure 3.3). Behind the walls (abutments), it is filled with soil which is represented by an additional layer of springs with stiffness k_{soil}. On top of the beam there is a track which is also modelled as a beam (of much less flexural rigidity). The track beam is supported on a sprung mass system which represents pads, sleepers and ballast.

The vehicle and track/bridge model are coupled together via the wheel/rail interaction, i.e., the DOF's of the wheels and the DOF's of the rail are combined. Each of the subsystems can be defined by a set of equations of motion. The coupling of the subsystems is addressed by the coupled equations of motion of the complete model. The equations of motion are solved using the Newmark-Beta numerical integration scheme.

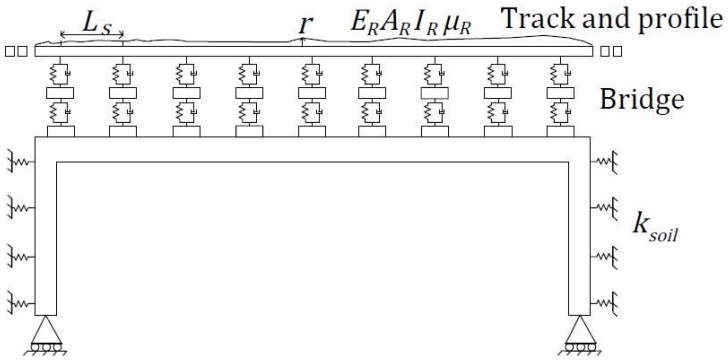

(a)

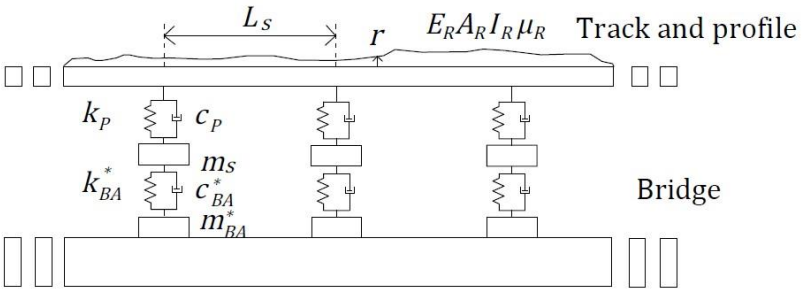

(b)

Figure 3.3 (a) Elevation of track-bridge model; (b) Detail of track-bridge model of Figure 3.3 (a).

3.3 Inverse Newmark-Beta Method to Calculate AP

As shown in previous work, for a road or a track on infinitely rigid supports, the profile can be determined by CE optimization using bogie vertical accelerations and angular velocities (OBrien et al., 2016). This approach is shown to be effective but computationally intensive and therefore impractical for kilometers of track data. In Chapter 2, the candidate proposes a much more efficient Inverse Newmark-Beta integration process to calculate the road profile using a half car model. It is also used to calculate track AP, as introduced in Appendix A. The Inverse Newmark-Beta concept is extended here from the simple half-car model introduced in Chapter 2 to a complex 4-axle railway carriage model which is closer to a real train.

The standard Newmark-Beta integration scheme is used to calculate the accelerations, velocities and displacements in a vehicle, $\{\ddot{u}\}$, $\{\dot{u}\}$ and $\{u\}$ due to a specified vehicle excitation (e.g., surface profile), i.e., to find $\{\ddot{u}\}$ according to Equation (3.1).

The Inverse Newmark-Beta concept uses measured accelerations and rates of rotation to find the excitation forces or the surface profile that generates them. In the standard Newmark-Beta integration scheme, the acceleration, $\{\ddot{u}\}$ can be calculated from $\{u\}$:

$$\ddot{u}_{t+\Delta t} = (u_{t+\Delta t} - u_t)a_0 \; - a_2\dot{u}_t - a_3\ddot{u}_t \tag{3.9}$$

In the inverse problem, the displacement, $\{u\}$ can be determined from measured acceleration:

$$u_{t+\Delta t} = (\ddot{u}_{t+\Delta t} + a_2\dot{u}_t + a_3\ddot{u}_t)/a_0 + \; u_t \tag{3.10}$$

where a_0, a_2 and a_3, are integration constants of the Newmark-Beta method.

For the 4-axle car model, accelerations and rates of rotation on bogies, $\ddot{u}_b$ and $\dot{\theta}_b$, are known inputs. Other parameters, $\dot{u}_b$, u_b, $\ddot{\theta}_b$ and θ_b of the bogies can be calculated from the known inputs according to the inverse Newmark-Beta concept. Then, using the equations of motion of the main body, the displacement and rotation of the carriage (u_v and θ_v) can be calculated. Accelerations and velocities of the body, $\ddot{u}_v, \dot{u}_v$, $\dot{\theta}_v, \ddot{\theta}_v$ can be calculated from u_v and θ_v. Therefore, all the terms on the left side of Equation (3.1) are known and on the right side of Equation (3.1), F can be found. Finally, the AP that excited the vehicle and caused the accelerations, r_w can be determined by solving Equation (3.5). Details of this processes are shown in the Appendix B.

Here, a 100 m railway track with a profile and a 4-axle railway carriage model vehicle of known properties, are used to generate the bogie vertical accelerations and angular velocities. The vehicle properties and speed are shown in Table 3.1 (Iwnicki, 1998). These signals are then taken as inputs and used to back-calculate the AP using the Inverse Newmark-Beta method. The calculated results are compared with the original 'true' AP in Figure 3.4. The calculated result is from the first axle of this train. The calculated AP has similar local features to the 'true' AP but is displaced upwards by a 'drift' effect that results from an accumulation of numerical inaccuracies. As the drift effect is very low frequency, it has a negligible effect on the train/track dynamic interaction. Changes in pseudo-static component of the AP, as a result of bridge deflection, are normally also in the low frequency range. However, as bridge deflection is zero at the supports, drift in the signal as the vehicle crosses the bridge can be removed using a linear correction or filter.

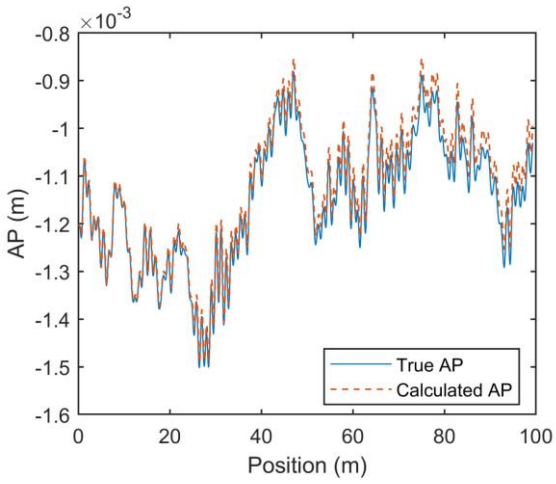

Figure 3.4 'True' AP and that calculated AP using the Inverse Newmark-Beta equations.

Table 3.1 Vehicle properties used to calculate the AP (Iwnicki, 1998).

Property	Symbol	Unit	Value
Carriage body mass	m_v	kg	32.4×10^3
Carriage body moment of inertia	I_v	kg m^2	1.99×10^6
Speed	v	m/s	33
Bogie mass	m_b	kg	2,615
Bogie moment of inertia	I_b	kg m^2	1,476
Wheelset mass	m_w	kg	1,813
Primary suspension stiffness	k_p	N/m	2.4×10^6
Secondary suspension stiffness	k_s	N/m	0.86×10^6
Primary suspension damping	c_p	N s/m	7×10^3
Secondary suspension damping	c_s	N s/m	16×10^3
Distance between bogie centre of gravity and wheelsets	L_b	m	1.28
Distance between main body centre of gravity and bogies	L_v	m	9.5

3.4 Monitoring Track Using Self-Calibrating Batches of Vehicles

In the previous section, it is shown that the AP can be calculated from measured vertical accelerations and angular velocities if the properties of the train are known. Trains often make multiple runs on the same route. Hence, an instrumented carriage will provide data from multiple runs for which some 'global' vehicle properties such as spring stiffnesses and damping coefficients are the same but other 'local' properties, such as speed, mass and moment of inertia are not. In this study, the global properties are assumed to have been determined in a global

calibration exercise to some degree of accuracy. A novel process is presented for calculation of the local properties, which are taken to be different for every run of the train.

As first proposed in Chapter 2 for 2-axle vehicles, batches of runs of the same vehicle will be used to calculate profiles, and to determine the local properties. However, in this case, unlike Chapter 2, the track is supported on springs. The concept of Chapter 2 is that every vehicle is subjected to the same (rigidly supported) surface profile. Hence, whatever the vehicle properties, processing its measurements should give the same surface profile as all other runs. Chapter 2 uses this phenomenon to self-calibrate the system, finding the surface profile and the properties for every vehicle in the batch. CE optimization is used to find those train properties that imply the same profile for all runs in the batch.

In this chapter, the fleet monitoring concept is extended to 4-axle railway carriages passing over tracks on spring supports. As the surface profile is no longer on rigid supports, the track deflects under the weight of the train. From the vehicle's perspective, it is excited by an AP made up of the unloaded surface profile plus deflection components due to deformation of the track under its own weight. The hypothesis is that the system can be calibrated by forcing all calculated APs to be the same (for all trains).

3.4.1 Methodology

Like the Genetic Algorithm, CE is a population-based method of optimization which considers multiple feasible solutions in each generation (or iteration) of the process (Rubinstein and Kroese, 2004). Firstly, a population of trial values of the vehicle parameter vector is generated. For calibration of a particular batch, global train-specific parameters (such as vehicle stiffnesses) are assumed to be known and only local run-specific parameters are needed. In this case, the local parameter vector has three components: carriage mass (m_v), moment of inertia (I_v) and speed (v).

In the CE process, a population of parameter vectors is randomly generated from a normal distribution using Monte Carlo simulation. Using the generated masses, moments of inertia, speeds and known global properties, the AP is calculated from the bogie vertical accelerations and angular velocities using the Inverse Newmark-Beta method. This process is repeated for all vehicles so the total number of unknown local properties in the vector is $3n_b$, where n_b is the number of runs in the batch.

In the first generation of solutions, the n_b generated APs will not be correct as the (run-specific) train properties will not generally be correct. However, better trials of the $3n_b$ parameters can be identified as those for which the calculated APs are closest to each other. Thus, an 'elite set' of the trials with the best property vectors can be identified using an objective function that captures similar APs within the batch. While more sophisticated measures of 'similarity' of APs are possible, a simple approach is adopted here, and the objective function is defined as the sum of squared differences between each AP and the mean of all calculated APs. Hence, the objective function for the j^{th} trial solution, O_j, is the sum of squared differences of the AP generated by this trial vector of $3n_b$ properties and the mean AP generated by all vehicles.

$$O_j = \sum_{h} \sum_{i=1}^{n_b} \sum_{k} \left(r_{h,i,j,k} - \bar{r}_{h,j,k} \right)^2 \tag{3.11}$$

where $r_{h,i,j,k}$ is the k^{th} AP elevation in the j^{th} trial under the h^{th} axle of the i^{th} vehicle in the batch, and $\bar{r}_{h,j,k}$ is mean AP in the j^{th} trial under the h^{th} axle of the n_b vehicles of the batch:

$$\bar{r}_{h,j,k} = \frac{1}{n_b} \sum_{i=1}^{n_b} r_{h,i,j,k} \tag{3.12}$$

As AP elevations are defined in space and these calculations are processed at fixed time intervals arising from the scan rate of the data, there needs to be a conversion to allow for the different speed of each run. For this purpose, the mean speed for all runs is used as the reference and the data for each individual run is interpolated to find the AP elevations corresponding to this reference speed.

In the CE optimization, the elite set is defined as the 10% of trial solutions that have the least values for the objective function. The vector mean and standard deviation of this elite set, μ and σ are calculated and used as the basis to generate the next generation of trial vehicle properties by Monte Carlo simulation. This process is repeated until convergence. A number of restarts of the process are used to avoid premature convergence (Botev and Kroese, 2004). In each restart, the vector mean is retained but the standard deviation is reset to its initial value.

3.5 Bridge Health Monitoring

When trains are traveling on track only (off-bridge), their data can be used to monitor AP which is a valuable measure of track condition. In addition, as was shown above, off-bridge data can

be used to determine local train dynamic properties. When a train crosses a bridge, it is subject to another AP, this time made up of a combination of the track profile, track deformation and elements of bridge deflection. Because the AP includes bridge deflections, it contains information about the bridge response to applied load and ultimately about the bridge condition.

3.5.1 Moving reference influence line (MR-IL) calculation

Moving reference deflections are the deflections under a moving instrumented axle. They are affected by both bridge and vehicle properties and, as such, are different for every vehicle passage. To provide information about bridge condition, this data needs to be transformed into a form that is independent of the vehicle. The influence line (IL) of a bridge is the response to a unit moving load and is a useful descriptor of structural behaviour, independent of any vehicle property.

OBrien et al. (2006) describe a 'Matrix Method' to determine the IL from a measured multi-wheel response. This method is very effective at finding the IL directly from strain measurements. In this section, a method is proposed to find the moving reference influence line (MR-IL) for deflection under the leading axle of the railway carriage. In conventional structural analysis, an influence line describes the response at a fixed point on a bridge. By its nature, MR-IL is more complex as the point of reference is no longer fixed and the load and response may be at different relative locations. The 'general' MR-IL function, $J^1(x, y)$, is defined here as the response at a moving point, x, to a unit load at any point, y – see Figure 3.5. A special case is when the load and the measurement are at the same point ($x = y$). This response at a moving point, x, to a unit load at that point, is referred to here as the 'fundamental' MR-IL function, $J^0(x)$. It can be seen that the fundamental function is a special case of the general function: $J^0(x) = J^1(x, x)$. This section describes a methodology which extends the Matrix Method of OBrien et al. (2006) to find the fundamental MR-IL directly from moving reference deflection data.

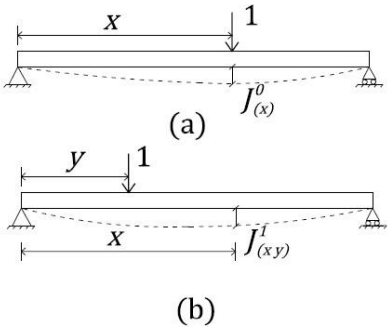

Figure 3.5 Deflection responses to moving unit load: (a) Response at *x* to load at *x*; (b) Response at *x* to load at *y*.

3.5.2 Methodology

The MR-IL derivation process is described for the simplest case of a 2-axle vehicle for which the 1st and 2nd axle weights, W_A and W_B, are known. The moving reference deflection under Axle A is:

$$\delta_A = W_A J^0(x) + W_B J^1(x, x-d) \tag{3.13}$$

where d is the axle spacing. Similarly, the deflection under Axle B is:

$$\delta_B = W_A J^1(x-d, x) + W_B J^0(x-d) \tag{3.14}$$

According to Betti's Reciprocal Theorem, the deflection at x due to a unit load at $(x - d)$ equals the deflection at $(x - d)$ due to a load at x, i.e.,

$$J^1(x, x-d) = J^1(x-d, x) \tag{3.15}$$

Hence, the equations above can be manipulated to remove all but the fundamental, J^0 terms:

$$W_A \delta_A - W_B \delta_B = W_A^2 J^0(x) - W_B^2 J^0(x-d) \tag{3.16}$$

Using Equation (3.16), the fundamental MR-IL, $J^0(x)$, can be found from the moving reference deflections, δ_A and δ_B using an approach similar to the Matrix Method proposed by OBrien et al. (2006). The process consists of finding the influence line ordinates that best fit the corresponding measured values. An error function is defined as the sum of the squared differences between the weighted measured deflections (left hand side of Equation. (3.16)) and the corresponding theoretical values (right hand side of Equation. (3.16)). Expressing the data in terms of scan number, k, instead of distance, x, gives:

$$E = \sum_{k=1}^{K} \left\{ W_A \delta_{A,k} - W_B \delta_{B,k} - W_A^2 J_k^0 + W_B^2 J_{k-c}^0 \right\}^2 \tag{3.17}$$

where K is the total number of scans, and c is the number of scans corresponding to the distance between the two axles, d. The best fit fundamental MR-IL is that which minimizes E. The minimum error function is found by taking partial derivatives with respect to each influence ordinate, J_k^0 , and setting them to zero. There are K scans for which at least one axle is on the bridge and, for a 2-axle vehicle, $K - c$ scans corresponding to the bridge length. Hence, there are $K - c$ unknown influence ordinate values. Setting all partial derivatives to zero results in system of $K - c$ simultaneous equations:

$$[A]\{J^0\} = \{b\} \tag{3.18}$$

Here, $\{J^0\}$ is the fundamental MR-IL vector and $[A]$ is a sparse symmetric matrix consisting of axle weight terms:

$$[A] = \begin{bmatrix} a_{1,1} & 0 & \cdots & a_{1,1+c} & 0 & \cdots & & \\ & \ddots & & & \ddots & & & \vdots \\ & & a_{i,i} & 0 & \cdots & a_{i,i+c} & 0 & \cdots \\ & & & \ddots & & & \ddots & \\ & \text{Symmetric} & & & a_{K-2c,K-2c} & 0 & \cdots & a_{K-2c,K-c} \\ & & & & & \ddots & & \vdots \\ & & & & & & & 0 \\ & & & & & & & a_{K-c,K-c} \end{bmatrix} \tag{3.19}$$

where the main diagonal elements are:

$$a_{i,i} = {W_A}^4 + {W_B}^4 \tag{3.20}$$

and the upper triangular elements are given by:

$$a_{i,i+C} = -W_A^2 W_B^2, i + c \leq K - c \tag{3.21}$$

The right-hand side of this system of equations consists of a vector, {b} with components made up of axle weight and measured MR deflection terms:

$$\{b\} = \begin{Bmatrix} W_A^3 \delta_{A,1} - W_A W_B^2 \delta_{A,c+1} + W_B^3 \delta_{A,c+1} \\ W_A^3 \delta_{A,2} - W_A W_B^2 \delta_{A,c+2} + W_B^3 \delta_{B,c+2} \\ \vdots \\ W_A^3 \delta_{A,c} - W_A W_B^2 \delta_{A,c+c} + W_B^3 \delta_{B,c+c} \\ W_A^3 \delta_{A,c+1} - W_A^2 W_B \delta_{B,c+1} - W_A W_B^2 \delta_{A,2c+1} + W_B^3 \delta_{B,2c+1} \\ \vdots \\ W_A^3 \delta_{A,K-2c} - W_A^2 W_B \delta_{B,K-2c} - W_A W_B^2 \delta_{A,K-c} + W_B^3 \delta_{B,K-c} \\ W_A^3 \delta_{A,K-2c+1} - W_A^2 W_B \delta_{A,K-2c+1} + W_B^3 \delta_{B,K-c+1} \\ \vdots \\ W_A^3 \delta_{A,K-c} - W_A^2 W_B \delta_{A,K-c} + W_B^3 \delta_{B,K} \end{Bmatrix} \tag{3.22}$$

The fundamental MR-IL vector, $\{J^0\}$, is found by solving Equation (3.18):

$$\{J^0\} = [A]^{-1} \{b\} \tag{3.23}$$

For a batch of measurements taken from 2-axle vehicles with the same inter-axle spacings for each run, there are only two axle spacings of relevance, zero and the axle spacing, *d*. Thus, all the information necessary to calculate the responses of a bridge to the vehicles is contained in two cross-sections through the general 2-dimensional MR-IL function: $y = 0$ (fundamental MR-IL) and $y = d$. Having found the fundamental MR-IL function using the above equations, it

should be possible to find the other function, corresponding to $y = d$, using a similar approach. However, only the fundamental MR-IL function is used here as it tends to have a better signal-to-noise ratio and is therefore believed to be a more robust indicator of bridge condition.

3.5.3 Preliminary results with a 2-axle half-car model

To illustrate the fleet monitoring concept for a bridge, the simple 2-axle 2-degree-of-freedom half-car and track beam with a smooth profile model shown in Figure 3.6, is simulated in MATLAB. This track beam is modelled as a simply supported beam using a Finite Element discretization. Vehicles are simulated crossing this beam and, for each run, moving reference deflections are calculated under each of the two axles. Using the equations described above, fundamental MR-ILs are calculated from the moving reference deflections. Here, a fleet of 20 vehicles is generated using Monte Carlo simulation with different body masses, m_s and body moment of inertias, I_s. The vehicle properties are shown in Table 3.2. The length of the beam is 20 m, and the second moment of area is 0.33 m^4. The Young's modulus is 35×10^9 N/m^2 and the mass per unit length is 9.6×10^3 kg/m. The 1st natural frequency vibration is 4.31 Hz. These vehicle and bridge property values are based on the values gathered from Fitzgerald et al. (2019) and Iwnicki (1998). The process is repeated for three different speeds, using the same batch of vehicles in each case. The calculated fundamental MR-ILs from 20 vehicle crossings are compared with the 'true' MR-ILs calculated from a simple static analysis, in Figure 3.7.

Table 3.2 Vehicle properties used to calculate MR-IL.

Property	Type	Symbol	Unit	Value	Mean	Standard deviation
Sprung mass	Local	m_s	kg	Varied	32×10^3	3.2×10^3
Sprung mass moment of inertia	Local	I_s	kg m^2	Varied $61.6m_s$		
Spring stiffness	Global	K_1, K_2	N/m	0.73×10^6		
Damping	Global	C_1, C_2	N s/m	7.5×10^3		
Distance of axle to body centre of gravity	Global	D_1, D_2	m	8.5		

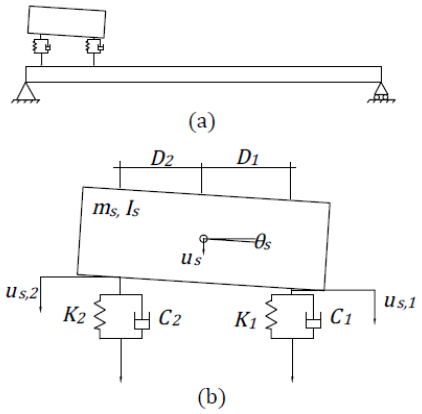

Figure 3.6 Model of 2-degree-of-freedom half-car and beam: (a) Overview; (b) Detail of 2-degree-of-freedom half-car.

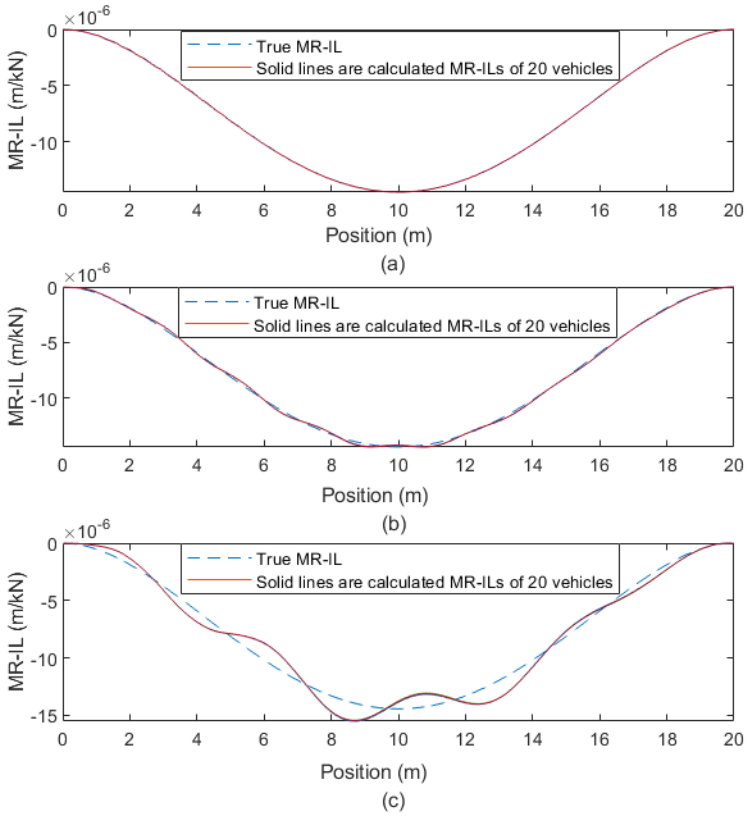

Figure 3.7 True and calculated fundamental MR-ILs for bridge and vehicle at different speeds: (a) 2 m/s; (b) 10 m/s; (c) 20 m/s.

For a speed of 2 m/s – effectively pseudo-static – the calculated fundamental MR-IL closely matches the corresponding true MR-IL. The dashed curve is the true MR-IL, i.e., the deflection at *x* due to a unit load at *x*, calculated using the Unit Load Theorem (a Corollary of the Theorem of Virtual Work). As speed increases, the influence of vehicle/bridge dynamic interaction becomes evident, with a significant divergence from the true MR-IL. A Fast Fourier Transform (FFT) on the MR-IL from the first vehicle at 20 m/s shows a dominant peak at 4.33 Hz, very

close to the 1st fundamental bridge frequency (4.31 Hz). The dynamics of the bridge clearly has an influence on the calculated results.

Two bridge states with different levels of global damage are simulated, with the resulting moving reference deflections and MR-ILs. The global damage event is represented as a uniform loss in the flexural rigidity of the whole beam as might occur due to uniform corrosion. The overall losses of flexural rigidity are 5%, 10%. Batches of 20 vehicles are generated with the same property values in Table 3.2 and simulated crossing the bridge in its healthy state and in the two damaged states. Two speeds are used separately: 10 m/s and 20 m/s. The mean calculated MR-ILs of the three bridge states are shown in Figure 3.8. The mean of the 20 mid-span MR-IL values, denoted $\widetilde{IL}$, is chosen as an indicator of bridge damage. It is noted that MR-IL is inversely proportional to the flexural rigidity, so inversely proportional to damage. For this reason, $Damage\ Indicator$ 1 is defined by Equation (3.24). The area under the mean calculated MR-ILs (denoted IL^*) is used as $Damage\ Indicator$ 2.

$$Damage\ Indicator\ 1\ (D1) = 100\left\{1 - \frac{\left({}^{1}/_{\widetilde{IL}}\right)^{D}}{\left({}^{1}/_{\widetilde{IL}}\right)^{H}}\right\} = 100\left\{1 - \frac{(\widetilde{IL})^{H}}{(\widetilde{IL})^{D}}\right\}$$

$$Damage\ Indicator\ 2\ (D2) = 100\left\{1 - \frac{\left({}^{1}/_{IL^*}\right)^{D}}{\left({}^{1}/_{IL^*}\right)^{H}}\right\} = 100\left\{1 - \frac{(IL^*)^{H}}{(IL^*)^{D}}\right\} \quad (3.24)$$

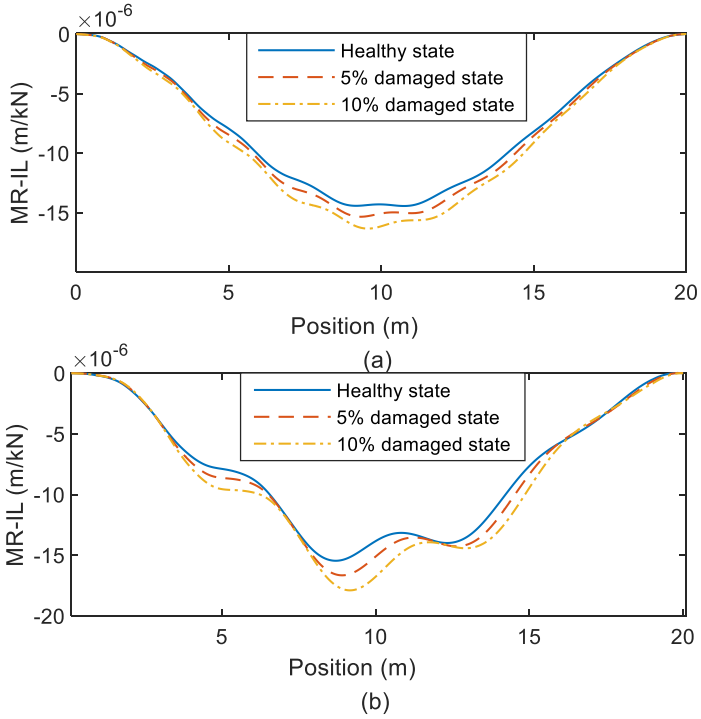

Figure 3.8 Mean calculated MR-ILs with different damage at different speed: (a) 10 m/s; (b) 20 m/s.

The calculated damage indicator values are shown in Table 3.3. For this simple example, there is a clear strong correlation between the damage indicators and the true loss of flexural rigidity. For the high speed case, *Damage Indicator* 1 is less accurate because of dynamic effects though it can show the damage state. The mean calculated MR-ILs are passed through a finite-impulse-response (FIR) low pass filter to remove the oscillation at the bridge frequency (4.31 Hz). FIR filter is attractive because it is inherently stable. It could remove the high frequency content of the MR-ILs. Other filters may be appropriate for other examples; the filters used here were effective for this case. For other cases, it may, for example, be necessary to remove records at particular speeds. *Damage Indicator* 2 is an effective way to detect bridge damage, even with dynamic effects. In fact, bridge first natural frequency and other frequencies may influence the calculated MR-IL values. Nevertheless, this indicator can be used to detect the level of damage with reasonably accuracy.

Table 3.3 Inferred damaged indicators and true damage levels.

True damage level			0%	5%	10%
Calculated damage level	10 m/s	*Damage Indicator* 1	0%	5%	11%
		Damage Indicator 2	0%	5%	10%
	20 m/s	*Damage Indicator* 1 with filter	0%	5%	12%
		Damage Indicator 1 without filter	0%	7%	15%
		Damage Indicator 2	0%	5%	10%

3.6 Blind Tests

The concept of monitoring railway bridge condition using batches of instrumented trains was assessed in a series of blind tests. A team from the Norwegian University of Science and Technology (NTNU) used the advanced model described in Section 3.2 to simulate batches of train carriages crossing a railway track and a culvert. The vertical accelerations and angular velocities from two bogies were generated by NTNU for various cases of the bridge condition. University College Dublin (UCD) analysed these signals to calculate the AP, determine the train properties and detect bridge damage level using the methods described above.

In these tests, the 'off-bridge' length of track used for calibration was 120 m (unknown to UCD) and the length of the bridge was 10.2 m. Data were analysed for seven different bridge damage states, including one perfectly healthy state. Global damage was simulated but, for each

damaged bridge, there were small random differences (5% standard deviation) between element flexural rigidities (stiffnesses), reflecting the natural variation in a corroded bridge. For each state, data from 50 different train journeys were used. In each run, all properties were kept constant except for the local properties of mass (m_v) moment of inertia (I_v) and speed (v) (Table 3.4). For each batch of runs, NTNU used Monte Carlo simulation to randomly generate these properties for each of the 50 vehicles in the fleet. The individual vehicle local property values were not made known to UCD but the means were provided, on the basis that these mean values are repeatable and can be determined for a particular site. UCD was provided with the approximate speed (v) which was a little different from the true value (to represent inaccuracy in a Global Positioning System (GPS) measurement). NTNU applied random noise (5% standard deviation) to other global vehicle properties when generating the signals to represent inaccuracy resulting from a global calibration process. Reference global property values were used by UCD which is shown in Table 3.4.

Table 3.4 Carriage vehicle properties in the blind test.

Property	Type	Symbol	Unit	Value before random noise
Carriage body mass	Local	m_v	kg	Varied
Carriage body moment of inertia	Local	I_v	kg m^2	Varied
Speed	Local	v	m/s	Varied
Bogie mass	Global	m_b	kg	2,615
Bogie moment of inertia	Global	I_b	kg m^2	1,476
Wheelset mass	Global	m_w	kg	1,813
Primary suspension stiffness	Global	k_p	N/m	2.4×10^6
Secondary suspension stiffness	Global	k_s	N/m	0.86×10^6
Primary suspension damping	Global	c_p	N s/m	7×10^3
Secondary suspension damping	Global	c_s	N s/m	16×10^3
Distance between bogie centre of gravity and wheelsets	Global	L_b	m	1.28
Distance between main body centre of gravity and bogies	Global	L_v	m	9.5

For railway track, variable stiffness at the ballast and sub-ballast levels were generated randomly using a 'Gaussian process' algorithm which allows small incremental changes. To confirm that the method is not sensitive to the profile assumed, the entire process (healthy + 6 damage states) was repeated for two different track profiles, making a total of 14 batches of runs. To help establish the baseline, the two batches for which the bridge was healthy, were identified to UCD as such. To separate the track and bridge parts, the starting point of the bridge

in each run was provided. For application in the field, it is proposed that the location of the bridge relative to the data can be estimated with a GPS and can be found more accurately using an optimisation algorithm. In this blind test, UCD used the 4-axle railway carriage model and the 2-axle 2-degree-of-freedom half-car model to analyse these signals.

3.6.1 Results with 4-axle railway carriage model

The 4-axle railway carriage model used by UCD (Figure 3.1) is the same as that used by NTNU. Hence, the validation in this subsection does not address differences in the models. It does show the ability of the proposed approach to infer model parameter values from the simulated values provided by NTNU to UCD and an insensitivity to some potential sources of inaccuracy (vehicle global property values and bridge flexural rigidities).

Using the off-bridge data and the fleet monitoring concept, the APs and vehicle local properties (masses, moments of inertia, speeds) were calculated from the vertical accelerations and angular velocities. Figure 3.9 shows the calculated AP from one run under the 1st axle over Profile 1. It is compared to the true AP, provided subsequently by NTNU. This result is for the bridge in State 7 (healthy) but this has no effect as the data is off-bridge. It shows an obvious difference between calculated APs and true APs in the initial value which generates a constant difference in the whole signal. After shifting, it shows a very close match between calculated APs after shifting and true APs. Figure 3.10 shows the calculated values for the local vehicle properties for each of the 50 trains in the batch for Profile 1, State 7. The calculated vehicle properties are generally close to the true values, with some small differences for particular vehicles. As can be seen in Figure 3.10(c), the speeds given by NTNU are sometimes significantly different from the true values (e.g., Run 2), but the calculated speeds are quite accurate.

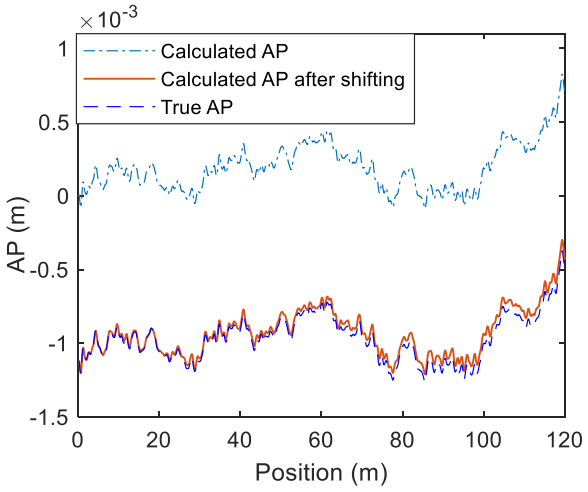

Figure 3.9 Calculated AP, calculated AP after shifting and true AP (off-bridge) for Profile 1, State 7 and Run No. 1.

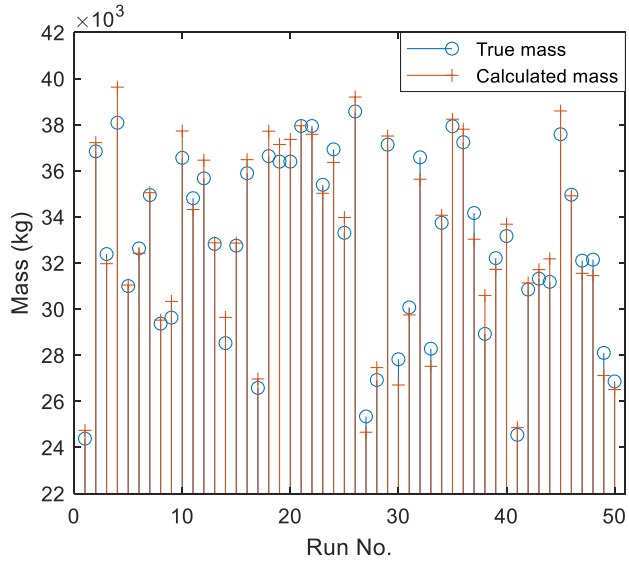

(a)

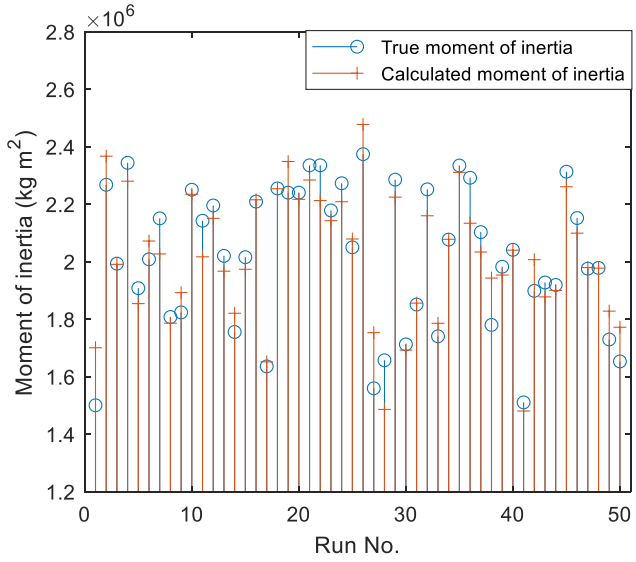

(b)

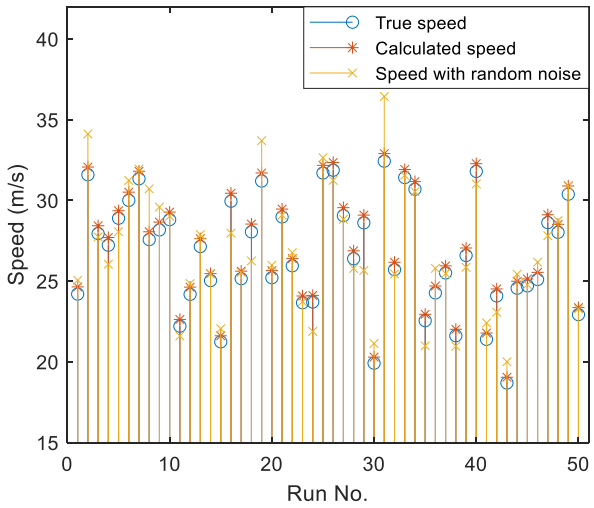

(c)

Figure 3.10 Calculated vehicle masses for each of the 50 runs in the batch, running on Profile 1, State 7: (a) vehicle masses; (b) vehicle moments of inertia; (c) vehicle speeds

The vehicle properties calculated using the off-bridge data, are used to find the APs for the section of track on the bridge. For each run, the APs under each of the four wheels are found using the Inverse Newmark-Beta method from the signals provided by NTNU. The calculated AP of the bridge from one run over Profile 1, State 7, is shown in Figure 3.11. In this figure, the calculated AP is very close to the true one after shifting. The fundamental MR-IL of the first bogie is calculated from the APs under these two wheels using the method described in Section 3.5. Figure 3.12 is a box plot showing the mid-span MR-IL values for Profile 1, plotted against the true damage level. Each box represents data from 50 mid-span MR-IL values and one bridge state. Here the State 7 is the healthy bridge and has the smallest MR-IL values. On each box, the central mark indicates the median, and the bottom and top edges of the box indicate the 25th and 75th percentiles, respectively. The whiskers extend to the most extreme data points not considered outliers, and the outliers are plotted individually using the '+' symbol. The box plot shows that the mid-span MR-IL values provide good repeatability, with obvious differences between damage states. The mean of the 50 mid-span MR-IL values and the area under the mean calculated MR-IL are used to calculate the bridge damage indicator defined in Equation (3.24).

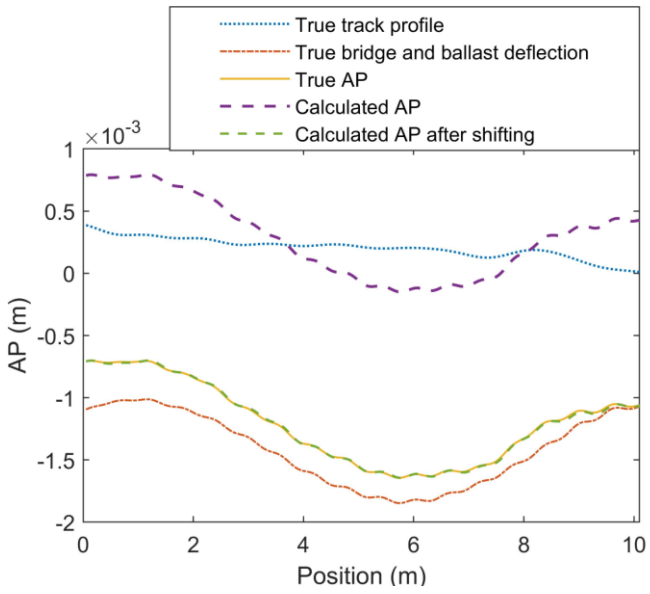

Figure 3.11 The true and calculated AP of the bridge from one run over Profile 1, State 7.

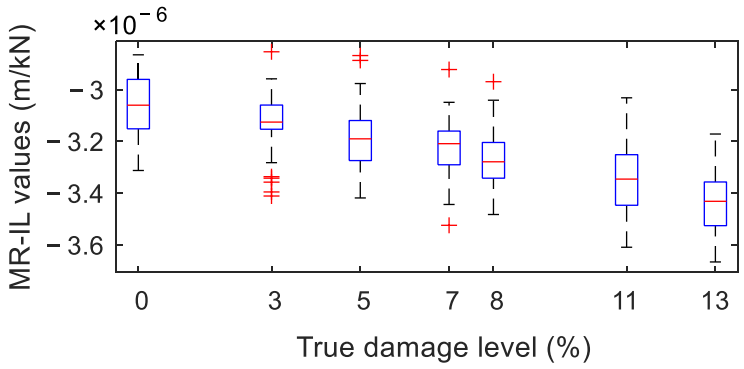

Figure 3.12 Box plot of mid-span fundamental MR-IL values of carriage model for Profile 1.

The corresponding true levels of damage, reported by NTNU, are defined as the percentage losses in flexural rigidity. The numerical results are presented in Table 3.6. All damage states were identified, and the level of damage was accurately found, without prior knowledge of the true states. There is little sensitivity to the profile used in the simulations. Further, there is little difference in the effectiveness of *Damage Indicator* 1 and *Damage Indicator* 2.

3.6.2 Results with 2-axle half-car

UCD also used a 2-axle 2-degree-of-freedom half-car to represent the bogie of the NTNU 4-axle railway carriage model. The objective was to determine if the method is effective when the numerical model (of UCD) is simpler than the true behaviour (simulated by NTNU). It is attempted to create a situation where, as in real life, the model used in the damage calculation was less sophisticated than the model (or the reality) used to generate the input data to the algorithm. The 2-axle model has the capacity to capture the bouncing and rocking motions of the bogie but not the carriage rocking motion that transfers load between bogies. For a 2-axle half-car, given the vertical accelerations and angular velocities, APs under each axle can be calculated using the Inverse Newmark-Beta integration scheme. Here, all the vehicle properties relate to the bogie and are global properties. The property values, before the application of random noise, are shown in Table 3.5. Using the calculated APs under the two axles, the MR-IL of each run are determined using the method described in Section 3.5. To calculate the MR-ILs, the 1st and 2nd axle weights, W_A and W_B, are determined from carriage mass, m_v, bogie mass, m_b, and wheelset mass, m_w. However, in this case, the individual carriage mass, m_v, for each run is not given. The mean value of m_v is used to calculate axle weights.

Table 3.5 Half car vehicle properties in the blind test.

Property	Symbol	Unit	Corresponding property in 4-axle railway carriage model	Value
Sprung mass	m_s	kg	m_b	2,615
Sprung mass moment of inertia	I_s	kg m^2	I_b	1,476
Spring stiffness	K_1, K_2	N/m	K_p	2.4×10^6
Damping	C_1, C_2	N s/m	C_p	7×10^3
Distance of axle to body centre of gravity	D_1, D_2	m	L_b	1.28

A box plot showing the mid-span MR-IL values for Profile 1 is plotted in Figure 3.13. For this calculation, there is considerably more variability in the damage indicators for individual runs, relative to the differences due to damage. However, the calculated damage levels still compare well with the corresponding true levels, as shown in Table 3.6.

Table 3.6 Inferred and true damage levels

Bridge state No.			1	2	3	4	5	6	7
4-axle railway carriage model	Profile 1	$D1$	3%	12%	9%	6%	4%	7%	0%
		$D2$	4%	14%	11%	7%	5%	8%	0%
	Profile 2	$D1$	5%	11%	9%	7%	4%	7%	0%
		$D2$	5%	12%	10%	7%	5%	7%	0%
2-axle half-car	Profile 1	$D1$	4%	10%	9%	4%	2%	6%	0%
		$D2$	5%	11%	10%	4%	3%	6%	0%
	Profile 2	$D1$	3%	10%	8%	6%	5%	6%	0%
		$D2$	2%	9%	7%	5%	3%	6%	0%
True damage level			3%	13%	11%	7%	5%	8%	0%

*$D1$ means $Damage\ Indicator\ 1$ and $D2$ means $Damage\ Indicator\ 2$

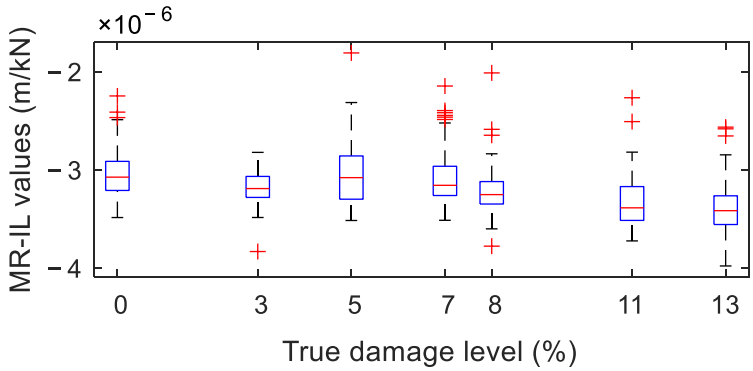

Figure 3.13 Box plot of mid-span fundamental MR-IL values of half-car model for Profile 1.

3.7 Conclusions

This chapter presents a numerical investigation of a novel method to determine AP and detect bridge damage using bogie vertical accelerations and angular velocities measured in batches of passing trains. Firstly, an Inverse Newmark-Beta method is developed to calculate the AP of the railway track using train measurements. A 4-axle railway carriage and train/track/bridge dynamic interaction model is used here to generate bogie vertical accelerations and angular velocities, the simulated measurements. The result shows that the calculated AP is same as the 'true' AP and this method is efficient. Combining the Inverse Newmark-Beta method with CE optimisation, the APs of the track and vehicle properties can be calculated accurately using batches of trains.

The work is expanded to introduce a new method to determine the moving reference influence line from moving reference deflections. A 2-axle half- car and track beam model is tested with different bridge damage. The results show the moving reference influence line is a good indicator of the bridge damage level.

Finally, the results are validated in a blind test with an independent research group. For this, the analysis is carried out using the same 4-axle railway carriage model that generated the data and a simpler 2-axle half-car. For both cases, the moving reference influence lines are determined using measurements from train. And the damage levels of the bridge are inferred by the calculated moving reference influence lines with very good accuracy. A culvert model is used in the blind test and a simply supported bridge model is also tested in Section 3.5.3. This method

works well for these two bridge models. A wider range of bridge models should be investigated in future work.

The idea of the fleet monitoring concept is developed in this chapter. As it will monitor the bridge through time, it will average out the effects through a variety of environmental conditions, including temperature. This mitigates against 'contamination' by changes in environmental conditions. The fleet monitoring concept has the potential to monitor bridges by combining drive-by data from a large number of in-service trains. To analyse large amounts of data, the fleet monitoring concept may be further developed using Machine Learning strategies. A passenger carriage is simulated here. It is expected that using freight carriages with one level of suspension would tend to improve the accuracy of the calculated AP. The train used in this chapter is modelled simply as a 2D model. Further work is needed by to extend this to a 3D train model and to allow for non-linearity in the vehicle. Ultimately, field testing will be needed to validate the concept.

Chapter 4 – A Bayesian Approach to the Estimation of Road Profile and Bridge Damage from a Fleet Passing Vehicle Measurements

Authors:

Eugene J. OBrien

Simon Wilson

Jennifer Keenahan

Yifei Ren

Paper Status:

Submitted for publication to *Structural Control and Health Monitoring*.

Note to the Reader:

The work in this chapter is entirely the work of the author, under the supervision of Prof. OBrien and Dr. Keenahan. Prof. Wilson provided specialist supervision on Bayesian method problem.

Chapter 4 – A Bayesian Approach to the Estimation of Road Profile and Bridge Damage from a Fleet Passing Vehicle Measurements

4.1 Introduction

The monitoring of road and bridge damage is important in minimizing unscheduled disruptions to the transportation network. Traditional visual inspection methods can work well but are costly and time-consuming. As an alternative, a 'drive-by' method of damage detection has been proposed by Yang et al. (2004), Yang and Lin (2005) and has developed significantly in recent year. This method uses inertial measurements from passing vehicles to provide information on infrastructure health. Gonzalez et al. (2008) propose a method to estimate road condition using vehicle-mounted accelerometers. Road profiles can be classified using the relationship between the power spectral densities of road surface and vehicle accelerations via a transfer function. Although a drawback is that the profile elevations cannot be determined. Harris et al. (2010) determine the profile heights from observed responses in a known vehicle using a combinatorial optimisation technique. The estimated heights are found to provide a very good fit to the true values. Chapter 2 proposes a novel Inverse Newmark-Beta method to calculate the profile from vehicle accelerations directly, where the vehicle properties are known. A vehicle fleet monitoring concept is also introduced to calculate profiles from the accelerations of a fleet of vehicles without prior knowledge of their properties. Here, Inverse Newmark-Beta method and a Cross Entropy optimisation technique are used together and the road profile is determined with a high degree of accuracy. It is becoming increasingly common for vehicles to be instrumented with sensors, including accelerometers and it seems reasonable to assume that, in the medium or long term, this data can be accessed for road and bridge management purposes. Further, the fifth generation (5G) communications technology, that has been recently developed, allows massive simultaneous connections, even under high mobility situations or densely populated areas (Guevara and Auat Cheein, 2020). This makes it possible to collect large amounts of data from a fleet of vehicles in real time.

Most research to date in the area of 'drive-by' bridge condition monitoring, uses measurements from passing vehicles to identify dynamic characteristics such as natural frequency (Yang et al., 2004), mode shapes (Zhang et al., 2012) or damping (Gonzalez et al., 2012). Other damage detection techniques have been proposed without finding the conventional dynamic properties

of the bridge (Yang et al., 2020a, Malekjafarian et al., 2015). OBrien et al. (2014) apply moving force identification theory in order to identify the dynamic forces between the vehicle and he bridge from the vehicle response. A new algorithm is also developed to identify bridge stiffness which is generally well correlated with bridge damage. OBrien and Keenahan (2015) use a traffic speed deflectometer (TSD) vehicle model to generate simulated measurements. The data gathered is used in an adapted Cross Entropy (CE) optimisation procedure to infer the apparent profile (AP) of the bridge, i.e., the true profile plus components of bridge deflection under the vehicle. The time shifted difference in apparent profiles is used to detect bridge damage even for low damage levels. It requires extremely accurate measurements due to the very limited time window when the vehicle is interacting with the bridge. Li et al. (2020) propose a new two-step method for bridge damage identification from the response of a passing vehicle. Firstly, values of road roughness are calculated from the vehicle responses using a dual Kalman filter (DKF). Then, bridge damage is identified based on an interaction force sensitivity analysis with Tikhonov regularization.

Some researchers use smartphones in passing vehicles as sensors to monitor transportation infrastructure. Souza et al. (2018) develop a new system to evaluate road pavement condition using smartphone data. These smartphone sensors can measure the vehicle vibration which can be used to classify the road quality. Zhao et al. (2019) estimate the road profile using vehicle responses measured by smartphones. The vehicle is modelled as a half car and it is suggested that its parameters can be determined by a genetic algorithm using its responses when passing over a bump of known size. With the calculated vehicle parameters, an augmented Kalman filter is used to estimate the road profile. The method provides good results when validated by experiments. Wu et al. (2020) propose a method to identify potholes in road surfaces using smartphones with accelerometers. Machine-learning models can extract features from acceleration signals and used to identify potholes. Mei et al. (2020) present a novel system for transportation infrastructure monitoring using smartphone sensors in passing vehicles. They propose the use of vibration data collected from a large number of smartphones in moving vehicles to monitor bridges. The results show that the presence of damage can be identified. Road deformation is also shown to be measurable using gyroscopes in smartphones in a series of laboratory experiments. Finally, road surface condition is assessed using a GoPro sports camera. Though these methods can monitor transportation infrastructure in a low cost and efficient way, the interaction between the smart phone and its owner seems likely to influence the accuracy of the results.

In Chapter 2, the results are found to be sensitive to noise. In this chapter, a Bayesian approach is introduced to reduce the influence of noise. The Bayesian approach is used to determine the road profile and bridge damage. Wilson et al. (2006) use a Bayesian statistical inference algorithm to update the distributions of multiple parameters in a fleet of vehicles, using prior assumed distributions and a set of observed dynamic tyre forces from a 'true' fleet of simulated vehicles. It is shown that the fitted distributions, obtained from the Bayesian statistical inference, yield very good agreement with the true distributions.

In this chapter, the road profile is determined with accelerations from a simulated fleet of passing vehicle accelerations, using a Bayesian approach. The vehicle properties, normalized with respect to sprung mass, can be found at the same time. Then, the Bayesian approach is used again to solve the bridge problem. Bearing damage is found to be detectable. Also, the bridge properties and vehicle sprung masses can be calculated. The method is also able to detect local damage, simulated as a crack in the bridge. The results show that the level and the locations of the damage can be determined by this method. Fleet monitoring used in this chapter is incredibly powerful due to the potentially very large quantity of measurements involved.

4.2 Numerical Modelling

In this chapter, a simple coupled vehicle and bridge model is used to demonstrate the principle. The vehicle is represented with a quarter car model and it passes over a 20 m approach length followed by a 20 m simply supported finite element (FE) beam model with a smooth road profile. Similar Vehicle-Bridge-Interaction (VBI) models have been used by many other authors (Tan et al., 2019, Elhattab et al., 2016, Malekjafarian et al., 2019). For the approach section, a 2-dimensional (2-D) profile and a 3-dimensional (3-D) 'carpet profile' are used in sperate simulation. For the 2-D runs, a class 'A' road profile is generated based on the ISO standard (ISO 8608: 1995). For the 3-D profile runs eleven alternative 2-D profiles are generated to represent the 3-D surface 'carpet'. The objective is to allow for the differences in excitation caused by small differences in the lateral position of vehicles on the road. The result is a varied but correlated excitation of the passing vehicles. For any given vehicle, one of the eleven profiles is selected according to a truncated Normal distribution, using Monte Carlo simulation (Blab and Litzka, 1995).

The quarter car vehicle model (Figure 4.1) has a sprung mass, M, and an unsprung mass, m, representing the body and axle masses of the axle system respectively. The sprung and unsprung

masses are connected by a spring of stiffness, K, and a viscous damper with damping, c. The unsprung mass connects to the road/bridge surface via a spring of stiffness, k, representing the tyres.

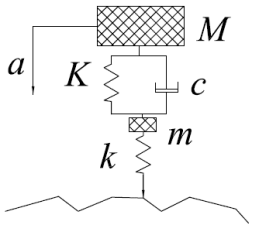

Figure 4.1 Quarter-car model

The bridge is represented by a 20 m span simply supported Euler-Bernoulli beam. It consists of 20 beam elements, each with 4 degrees of freedom (DOF). A span/depth ratio of 20 is assumed, giving a depth of 1 m. The beam is assumed to be of solid rectangular cross section and could be in-situ concrete or composite precast with solid concrete infill. The second moment of area is then $I = 1.25\text{m}^4$, assuming 15 m width. This beam has a modulus of elasticity, $E = 35 \times 10^9\text{N/m}^2$, density $\rho = 2{,}500\text{kg/m}^3$ and mass per unit length $\mu = 37{,}500\text{kg/m}$. The bridge damping ratio is 3% (Li, 2006).

The dynamic interaction between the vehicle and the road profile or bridge is simulated in MATLAB. The vehicle and the road profile or bridge are coupled at the tyre contact points via the interaction force vector. This coupled system is solved using the Newmark-Beta integration scheme.

4.3 Profile Calculation

In this section, a Bayesian updating approach is used to calculate the road profile using measured accelerations ($\boldsymbol{a}$) from a fleet of vehicles. To illustrate the process, the quarter-car model, described in Section 4.2, is used which has 6 unknown vehicle properties, M, m, K, k and c. The profile elevations are, $\boldsymbol{R} = R(y_1), \dots, R(y_P)$ where $y_1, \dots, y_P$ are corresponding location.

4.3.1 Data likelihood

A simple independent Gaussian error model is assumed for the deviations of the observed accelerations from the true ones. For nth vehicle, the model for its acceleration data $\boldsymbol{a_n}$ is

$$p(\boldsymbol{a_n}|\boldsymbol{R}, M_n, m_n, K_n, k_n, c_n) = \prod_{i=1}^{P} p(a_n(y_i)|A(y_i; \boldsymbol{R}, M_n, m_n, K_n, k_n, c_n))$$

$$= \prod_{i=1}^{P} \frac{1}{\sqrt{2\pi\sigma_1^2}} \exp\left(-\frac{1}{2\sigma_1^2}(a_n(y_i) - A(y_i; \boldsymbol{R}, M_n, m_n, K_n, k_n, c_n))^2\right)$$

$$= (2\pi\sigma_1^2)^{-0.5P} \exp(-\frac{1}{2\sigma_1^2}\sum_{i=1}^{P}(a_n(y_i) - A(y_i; \boldsymbol{R}, M_n, m_n, K_n, k_n, c_n))^2)$$

(4.1)

where $A(y_i; \boldsymbol{R}, M_n, m_n, K_n, k_n, c_n)$ is the vehicle acceleration calculated from a vehicle with properties, M_n, m_n, K_n, k_n, c_n, crossing the true profile $\boldsymbol{R}$. The term, σ_1^2 is observation error variance. Assuming that each vehicle's observations are independent, a likelihood is given for all of the acceleration data:

$$p(\boldsymbol{a}|\boldsymbol{R}, \boldsymbol{M_{1:N}}, \boldsymbol{m_{1:N}}, \boldsymbol{K_{1:N}}, \boldsymbol{k_{1:N}}, \boldsymbol{c_{1:N}}) = \prod_{n=1}^{N} p(\boldsymbol{a_n}|\boldsymbol{R}, M_n, m_n, K_n, k_n, c_n)$$

$$= (2\pi\sigma_1^2)^{-0.5NP} \exp(-\frac{1}{2\sigma_1^2}\sum_{n=1}^{N}\sum_{i=1}^{P}(a_n(y_i) - A(y_i; \boldsymbol{R}, M_n, m_n, K_n, k_n, c_n))^2)$$

(4.2)

4.3.2 Priors

A prior distribution $p(M_n|\varphi_M)$ is specified for each vehicle mass. It is the distribution of vehicle masses across the population of vehicles used on the road, which is usually assumed to be the same for each vehicle class. This distribution is described here as a normal distribution and φ_M is its mean and variance. It is assumed that these priors are independent for each vehicle, so the prior for all masses $\boldsymbol{M_{1:N}} = (M_1, \ldots M_N)$ is:

$$p(\boldsymbol{M_{1:N}}|\varphi_M) = \prod_{n=1}^{N} p\big((M_n|\varphi_M)\big) \tag{4.3}$$

In a similar fashion, prior distributions for all other vehicle properties are given as follows:

$$p(\boldsymbol{m_{1:N}}|\varphi_m) = \prod_{n=1}^{N} p\big((m_n|\varphi_m)\big) \tag{4.4}$$

$$p(\boldsymbol{K_{1:N}}|\varphi_K) = \prod_{n=1}^{N} p\big((K_n|\varphi_K)\big) \tag{4.5}$$

$$p(\boldsymbol{k_{1:N}}|\varphi_k) = \prod_{n=1}^{N} p\big((k_n|\varphi_k)\big) \tag{4.6}$$

$$p(\boldsymbol{c_{1:N}}|\varphi_c) = \prod_{i=1}^{N} p\big((c_n|\varphi_c)\big) \tag{4.7}$$

A prior distribution of the road profile uses an intrinsic Gaussian process and is determined as follows:

$$p\,(\boldsymbol{R}) = \prod_{i=1}^{P} \sqrt{\frac{\tau_1}{2\pi(y_i - y_{i-1})^2}} \exp\left(-\frac{\tau_1}{2(y_i - y_{i-1})^2}\big(R(y_i) - R(y_{i-1})\big)^2\right) \tag{4.8}$$

where τ_1 is a smoothing parameter for road profiles. It is the precision or inverse of the variance of a normal distribution. The larger its value, the less variation is allowed in the profile.

4.3.3 Posterior distribution

The output of the Bayesian analysis here is a posterior distribution, the unknown profile and vehicle properties can be estimated given the observed data. By Bayes' Law, this is given in terms of the likelihood and prior terms by (Lee, 2012):

$$\begin{aligned} &p(\boldsymbol{R}, \boldsymbol{M_{1:N}}, \boldsymbol{m_{1:N}}, \boldsymbol{K_{1:N}}, \boldsymbol{k_{1:N}}, \boldsymbol{c_{1:N}}|\boldsymbol{a}) \\ &\propto p(\boldsymbol{a}|\boldsymbol{R}, \boldsymbol{M_{1:N}}, \boldsymbol{m_{1:N}}, \boldsymbol{K_{1:N}}, \boldsymbol{k_{1:N}}, \boldsymbol{c_{1:N}}) p(\boldsymbol{R}) \left(\prod_{n=1}^{N} p\big((M_n|\varphi_M)\big)\right)\left(\prod_{n=1}^{N} p\big((m_n|\varphi_m)\big)\right) \\ &\left(\prod_{n=1}^{N} p\big((K_n|\varphi_K)\big)\right)\left(\prod_{n=1}^{N} p\big((k_n|\varphi_k)\big)\right)\left(\prod_{n=1}^{N} p\big((c_n|\varphi_c)\big)\right) \end{aligned} \tag{4.9}$$

The question now turns to the issue of computing Equation (4.9). The proposal here is to do it by Monte Carlo sampling, specifically Markov Chain Monte Carlo (MCMC) which is suitable for complex and high dimensional distributions (Gelfand and Smith, 1990, Wilson et al., 2006, O'Hagan and Forster, 2004). The specific MCMC method that is described here is called 'Metropolis within Gibbs' sampling. It samples a value of each unknown in turn: each of the vehicle properties, and then each value of the profile. It does this by randomly proposing a new value and then accepting or rejecting it with a certain probability. This probability is such that

the set of accepted samples converge to samples coming from Equation (4.9). The Monte Carlo simulation allows for the construction of approximations to the posterior distribution or parameters of it, such as means or percentiles (Tanner, 1996).

4.3.4 MCMC algorithm

Here a fleet of vehicles is generated based on the mean and standard deviations of vehicle properties which are shown in Table 4.1 (Wilson et al., 2006, Belay et al., 2008). There are 30 different vehicles in this small sample fleet. The fleet is simulated crossing a given road profile and sprung mass accelerations of these vehicles are generated as 'true' accelerations. 2-D and 3-D profile are used separately. Then these accelerations are used as input into the MCMC algorithm to back-calculate the profile and vehicle properties. Additive White Gaussian Noise (AWGN) of 2% is added to the measurements to allow for inaccuracy (Lyons, 2011).

Table 4.1 Vehicle properties.

Parameter	Symbol	Unit	Mean	St. dev.
Sprung mass	M	kg	4,450	445
Unsprung mass	m	kg	420	42
Suspension stiffness	K	N/m	500,000	50,000
Tyre stiffness	k	N/m	1,950,000	195,000
Suspension damping	c	Ns/m	20,000	2000

The MCMC algorithm is a series of 5 steps as outlined below. A flow chart, introducing this MCMC algorithm, is given in Figure 4.2.

1. Firstly, define an initial set of vehicle properties, $\boldsymbol{M}_{\boldsymbol{1:N}}^{(\boldsymbol{0})}$, $\boldsymbol{m}_{\boldsymbol{1:N}}^{(\boldsymbol{0})}$, $\boldsymbol{K}_{\boldsymbol{1:N}}^{(\boldsymbol{0})}$, $\boldsymbol{k}_{\boldsymbol{1:N}}^{(\boldsymbol{0})}$, $\boldsymbol{c}_{\boldsymbol{1:N}}^{(\boldsymbol{0})}$, and an initial profile $\boldsymbol{R}^{(\boldsymbol{0})} = R(y_1)^{(0)}, \dots, R(y_P)^{(0)}$. Define all parameters for the Gibbs sampler: number of iterations $n_{iter} = 2000$, standard deviations to generate unknowns $s_M = 200\text{kg}$, $s_m = 40\text{kg}$, $s_K = 30{,}000\text{N/m}$, $s_k = 100{,}000\text{N/m}$, $s_c = 1000\text{Ns/m}$, $s_{profile} = 0.001\text{m}$, $\tau_1 = 100{,}000$, and observation error variance, $\sigma_1^2 = 0.001$.
2. Compute the expected accelerations $A_n\left(y_i; \boldsymbol{R}^{(\boldsymbol{0})}, M_n^{(0)}, m_n^{(0)}, K_n^{(0)}, k_n^{(0)}, c_n^{(0)}\right), n = 1, \dots, N \text{ and } i = 1, \dots, P$. using the coupled system introduced in Section 4.2.
3. Let $\boldsymbol{R}^{\textbf{current}} = \boldsymbol{R}^{(\boldsymbol{0})}$.
4. For each iteration $j = 1, \dots, n_{iter}$, update vehicle properties and road profile by acceptance probability α_1 and β_1.

a) In iteration j, for each vehicle $n = 1, \dots, N$, generate a population of proposed values for $M_n', m_n', K_n', k_n', c_n'$ from a normal distribution which has a mean and variance equal to the previously sampled values.

$$M_n' \sim N(M_n^{(j-1)}, s_M^2) \tag{4.10}$$

$$m_n' \sim N(m_n^{(j-1)}, s_m^2) \tag{4.11}$$

$$K_n' \sim N(K_n^{(j-1)}, s_K^2) \tag{4.12}$$

$$k_n' \sim N(k_n^{(j-1)}, s_k^2) \tag{4.13}$$

$$c_n' \sim N(c_n^{(j-1)}, s_c^2) \tag{4.14}$$

b) Then, compute the expected accelerations with these proposed vehicle properties using the coupled system introduced in Section 4.2.

$$A_n\left(y_1; \boldsymbol{R}^{(\boldsymbol{j-1})}, M_n', m_n', K_n', k_n', c_n'\right), \dots, A_n\left(y_P; \boldsymbol{R}^{(\boldsymbol{j-1})}, M_n', m_n', K_n', k_n', c_n'\right)$$

c) Compute the acceptance probability α_1 using Equation (4.15):

$$\alpha_1 = min\left\{1, \frac{p\left(\boldsymbol{a_n}\middle|\boldsymbol{R}^{(j-1)}, M_n', m_n', K_n', k_n', c_n'\right)}{p\left(\boldsymbol{a_n}\middle|\boldsymbol{R}^{(j-1)}, M_n^{(j-1)}, m_n^{(j-1)}, K_n^{(j-1)}, k_n^{(j-1)}, c_n^{(j-1)}\right)}\right.$$

$$\left.\frac{p(M_n'|\varphi_M)}{p\left(M_n^{(j-1)}\middle|\varphi_M\right)}\frac{p(m_n'|\varphi_m)}{p\left(m_n^{(j-1)}\middle|\varphi_m\right)}\frac{p(K_n'|\varphi_K)}{p\left(K_n^{(j-1)}\middle|\varphi_K\right)}\frac{p(k_n'|\varphi_k)}{p\left(k_n^{(j-1)}\middle|\varphi_k\right)}\frac{p(c_n'|\varphi_c)}{p\left(c_n^{(j-1)}\middle|\varphi_c\right)}\right\}$$

$$= min\left\{1, \frac{\exp\left(-\frac{1}{2\sigma_1^2}\sum_{i=1}^{P}(a_n(y_i) - A_n\left(y_i; \boldsymbol{R}^{(\boldsymbol{j-1})}, M_n', m_n', K_n', k_n', c_n'\right))^2\right)}{\exp\left(-\frac{1}{2\sigma_1^2}\sum_{i=1}^{P}(a_n(y_i) - A_n\left(y_i; \boldsymbol{R}^{(\boldsymbol{j-1})}, M_n^{(j-1)}, m_n^{(j-1)}, K_n^{(j-1)}, k_n^{(j-1)}, c_n^{(j-1)}\right))^2\right)}\right.$$

$$\left.\frac{p(M_n'|\varphi_M)}{p\left(M_n^{(j-1)}\middle|\varphi_M\right)}\frac{p(m_n'|\varphi_m)}{p\left(m_n^{(j-1)}\middle|\varphi_m\right)}\frac{p(K_n'|\varphi_K)}{p\left(K_n^{(j-1)}\middle|\varphi_K\right)}\frac{p(k_n'|\varphi_k)}{p\left(k_n^{(j-1)}\middle|\varphi_k\right)}\frac{p(c_n'|\varphi_c)}{p\left(c_n^{(j-1)}\middle|\varphi_c\right)}\right\}$$

(4.15)

d) With probability α_1, the new proposed values are accepted, if accepted, let $M_n^{(j)} = M_n', m_n^{(j)} = m_n', K_n^{(j)} = K_n', k_n^{(j)} = k_n', c_n^{(j)} = c_n'$, if rejected, let $M_n^{(j)} = M_n^{(j-1)}, m_n^{(j)} = m_n^{(j-1)}, K_n^{(j)} = K_n^{(j-1)}, k_n^{(j)} = k_n^{(j-1)}, c_n^{(j)} = c_n^{(j-1)}$.

Here the way to do this is to generate a random number u uniformly distributed between 0 and 1. If $u \leq \alpha_1$, accept; else reject.

e) In iteration j, for each profile location $y_i,\ i = 1, \dots, P$, generate a proposed profile R_i for $R(y_i)$ using Equation (4.16):

$$R_i \sim N(R(y_i)^{(j-1)}, s_{profile}^2) \tag{4.16}$$

f) Let $\boldsymbol{R}^*$ be $\boldsymbol{R}^{\boldsymbol{current}}$ with $R(y_i)^{(j-1)}$ replaced by R_i.

g) Compute all values of $A_n\left(y_i; \boldsymbol{R}^*, M_n^{(j)}, m_n^{(j)}, K_n^{(j)}, k_n^{(j)}, c_n^{(j)}\right)$ that are different from $A_n\left(y_i; \boldsymbol{R}^{\boldsymbol{current}}, M_n^{(j)}, m_n^{(j)}, K_n^{(j)}, k_n^{(j)}, c_n^{(j)}\right)$ for $i = 1, \dots, P$ and $n = 1, \dots, N$.

h) Compute the acceptance probability β_1 using Equations (4.17), (4.18) and (4.19). In Equation (4.17), for $i = 2, \dots, P-1$:

$$\beta_1 = \frac{p\left(\boldsymbol{a}\middle|\boldsymbol{R}^*, M_{1:N}^{(j)}, m_{1:N}^{(j)}, K_{1:N}^{(j)}, k_{1:N}^{(j)}, c_{1:N}^{(j)}\right)}{p\left(\boldsymbol{a}\middle|\boldsymbol{R}^{\boldsymbol{current}}, M_{1:N}^{(j)}, m_{1:N}^{(j)}, K_{1:N}^{(j)}, k_{1:N}^{(j)}, c_{1:N}^{(j)}\right)} \frac{p(\boldsymbol{R}^*)}{p(\boldsymbol{R}^{\boldsymbol{current}})}$$

$$= \frac{\exp\left(-\frac{1}{2\sigma_1^2}\sum_{n=1}^{N}\sum_{i=1}^{P}\left(a_n(y_i) - A_n\left(y_i; \boldsymbol{R}^*, M_n^{(j)}, m_n^{(j)}, K_n^{(j)}, k_n^{(j)}, c_n^{(j)}\right)\right)^2\right)}{\exp\left(-\frac{1}{2\sigma_1^2}\sum_{n=1}^{N}\sum_{i=1}^{P}\left(a_n(y_i) - A_n\left(y_i; \boldsymbol{R}^{\boldsymbol{current}}, M_n^{(j)}, m_n^{(j)}, K_n^{(j)}, k_n^{(j)}, c_n^{(j)}\right)\right)^2\right)}$$

$$\times \frac{\exp\left(-\frac{\tau_1}{2}\left(\frac{(R_i - R(y_{i-1})^{(j-1)})^2}{(y_i - y_{i-1})^2} + \frac{(R(y_{i+1})^{(j-1)} - R_i)^2}{(y_{i+1} - y_i)^2}\right)\right)}{\exp\left(-\frac{\tau_1}{2}\left(\frac{(R(y_i)^{(j-1)} - R(y_{i-1})^{(j-1)})^2}{(y_i - y_{i-1})^2} + \frac{(R(y_{i+1})^{(j-1)} - R(y_i)^{(j-1)})^2}{(y_{i+1} - y_i)^2}\right)\right)}$$

(4.17)

For $i = 1$, it is:

$$\beta_1 = \frac{\exp\left(-\frac{1}{2\sigma_1^2}\sum_{n=1}^{N}\sum_{i=1}^{P}\left(a_n(y_i) - A_n\left(y_i; \boldsymbol{R}^*, M_n^{(j)}, m_n^{(j)}, K_n^{(j)}, k_n^{(j)}, c_n^{(j)}\right)\right)^2\right)}{\exp\left(-\frac{1}{2\sigma_1^2}\sum_{n=1}^{N}\sum_{i=1}^{P}\left(a_n(y_i) - A_n\left(y_i; \boldsymbol{R}^{\boldsymbol{current}}, M_n^{(j)}, m_n^{(j)}, K_n^{(j)}, k_n^{(j)}, c_n^{(j)}\right)\right)^2\right)}$$

$$\times \frac{\exp\left(-\frac{\tau_1}{2}\left(\frac{(R(y_2)^{(j-1)} - R_1)^2}{(y_2 - y_1)^2}\right)\right)}{\exp\left(-\frac{\tau_1}{2}\left(\frac{(R(y_2)^{(j-1)} - R(y_1)^{(j-1)})^2}{(y_2 - y_1)^2}\right)\right)}$$

(4.18)

For $i = P$, it is:

$$\beta_1 = \frac{\exp\left(-\frac{1}{2\sigma_1^2}\sum_{n=1}^{N}\sum_{i=1}^{P}\left(a_n(y_i) - A_n\left(y_i; \boldsymbol{R}^*, M_n^{(j)}, m_n^{(j)}, K_n^{(j)}, k_n^{(j)}, c_n^{(j)}\right)\right)^2\right)}{\exp\left(-\frac{1}{2\sigma_1^2}\sum_{n=1}^{N}\sum_{i=1}^{P}\left(a_n(y_i) - A_n\left(y_i; \boldsymbol{R^{current}}, M_n^{(j)}, m_n^{(j)}, K_n^{(j)}, k_n^{(j)}, c_n^{(j)}\right)\right)^2\right)}$$

$$\times \frac{\exp\left(-\frac{\tau_1}{2}\left(\frac{(R_P - R(y_{P-1})^{(j-1)})^2}{(y_P - y_{P-1})^2}\right)\right)}{\exp\left(-\frac{\tau_1}{2}\left(\frac{(R(y_P)^{(j-1)} - R(y_{P-1})^{(j-1)})^2}{(y_P - y_{P-1})^2}\right)\right)}$$

(4.19)

i) With probability β_1, the new proposed values are accepted, let $R(y_i)^{(j)} = R_i$. Else it is rejected and $R(y_i)^{(j)} = R(y_i)^{(j-1)}$.

j) Update $\boldsymbol{R^{current}}$ by replacing $R(y_i)^{(j-1)}$ with $R(y_i)^{(j)}$.

5. Let $\boldsymbol{R}^{(j)} = \boldsymbol{R^{current}}$ and store the updated set of samples $M_1^{(j)}, \dots, M_n^{(j)}, m_1^{(j)}, \dots, m_n^{(j)}, K_1^{(j)}, \dots, K_n^{(j)}, k_1^{(j)}, \dots, k_n^{(j)}, c_1^{(j)}, \dots, c_n^{(j)}$ and profile $\boldsymbol{R}^{(j)}$
   Repeat step 4 for the next iteration, $j \to j + 1$.

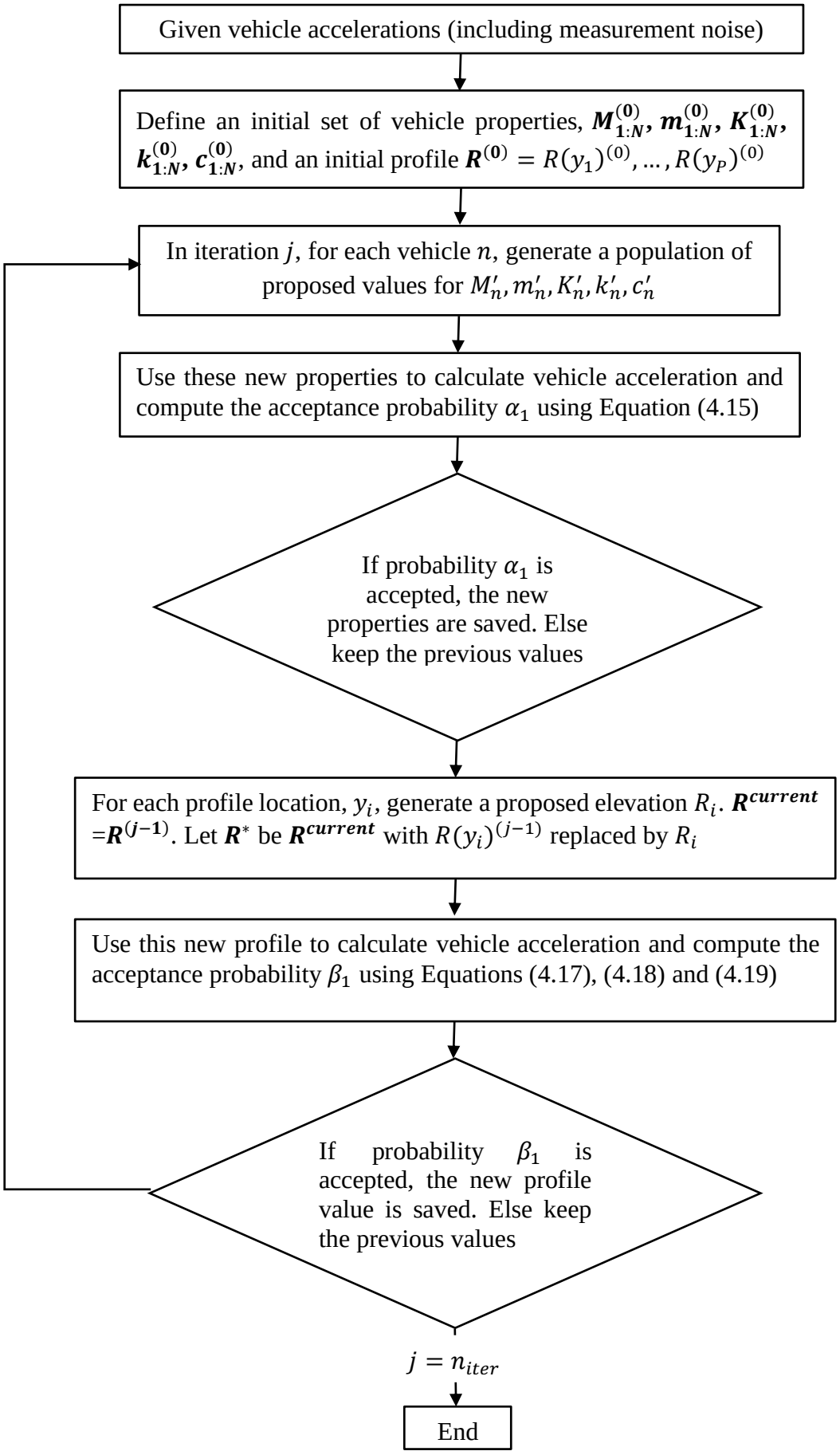

Figure 4.2 Flow chart of MCMC algorithm

4.3.5 Results of profile calculation

For the 2-D input profile, the output from the Bayesian analysis gives a calculated profile and inferred vehicle properties at the same time. The objective in the Bayesian analysis, is to estimate the data, but still leave some uncertainty. While good estimates are possible, the calculated results will not be exactly correct. One way to represent this is to use quantiles of the posterior distribution, which represent an interval in which the true value lies with a specified probability. In this case, the 2.5% and 97.5% quantiles of the MCMC samples and the mean of these samples are used as the calculated results. The mean calculated profile is very close to the true profile (Figure 4.3). Further, the 95% limits almost encompass true profile. The inferred vehicle properties can be found and are of reasonable accuracy, as can be seen in Figure 4.4. However, the method is found to be more accurate when the vehicle properties are normalized with respect to sprung mass, M and only the resulting normalized properties are found using the off-bridge data (The sprung masses will be found later using on-bridge data). These normalized property results are shown in Figure 4.5. Similar to other research in this area and the results in Chapter 2, it was not possible to accurately calculate the absolute values for properties, but it was possible to get the normalized values (Harris et al., 2010). For the 3-D profile, the mean calculated profile is close to the true mean profile found by taking all vehicles (Figure 4.6). In Figure 4.7, the calculated profile can be seen to capture the main features of the different profiles experienced by the 30 vehicles. Figure 4.8 shows that the calculated vehicle properties are not particularly accurate. Clearly even small differences in the lateral vehicle position are important.

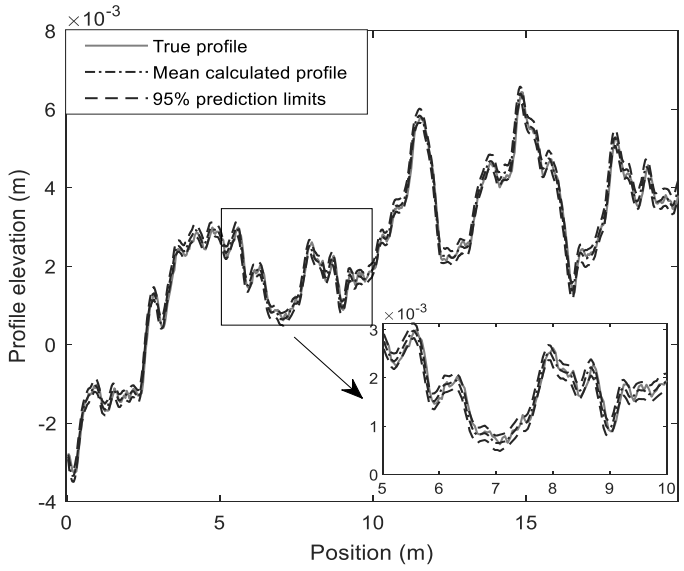

Figure 4.3 True and calculated profile (mean calculated and 95% prediction limits) for the 2-D profile case.

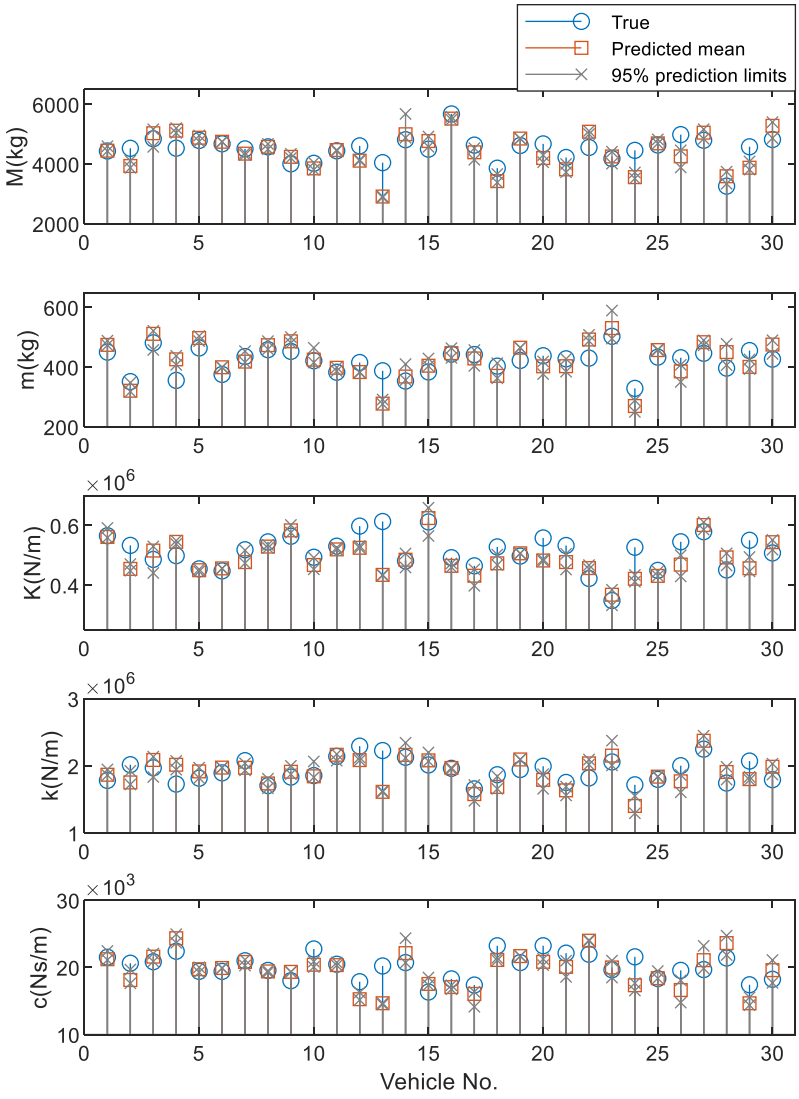

Figure 4.4 True and calculated vehicle properties (mean calculated and 95% prediction limits) for the 2-D profile.

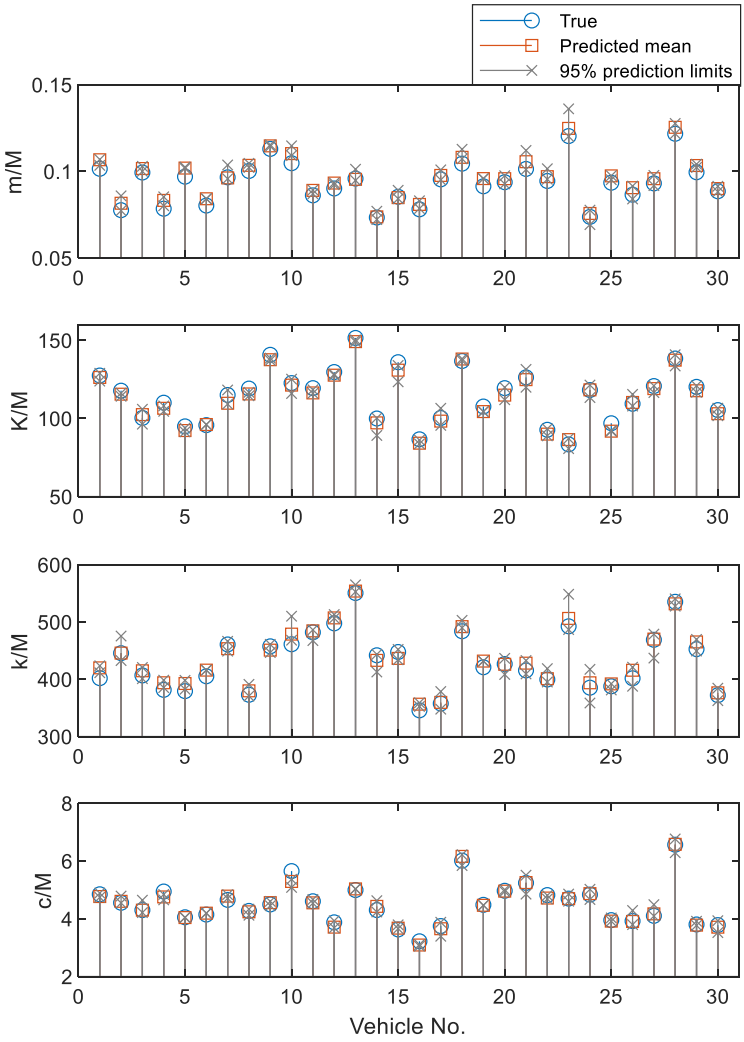

Figure 4.5 True and calculated vehicle properties (mean and 95% prediction limits), normalized with respect to sprung mass, *M*, for the 2-D profile case.

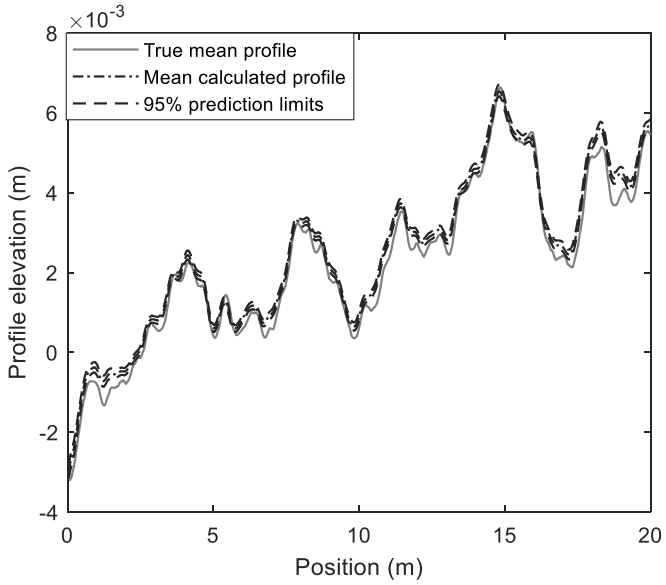

Figure 4.6 True mean profile of all vehicles and calculated profile (mean calculated and 95% prediction limits) for the 3-D profile case.

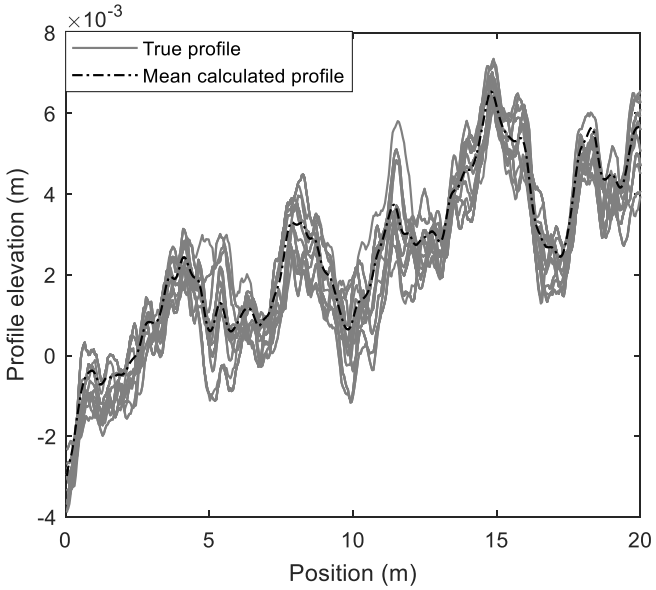

Figure 4.7 True profiles of all vehicles and mean calculated profile in 3-D profile case.

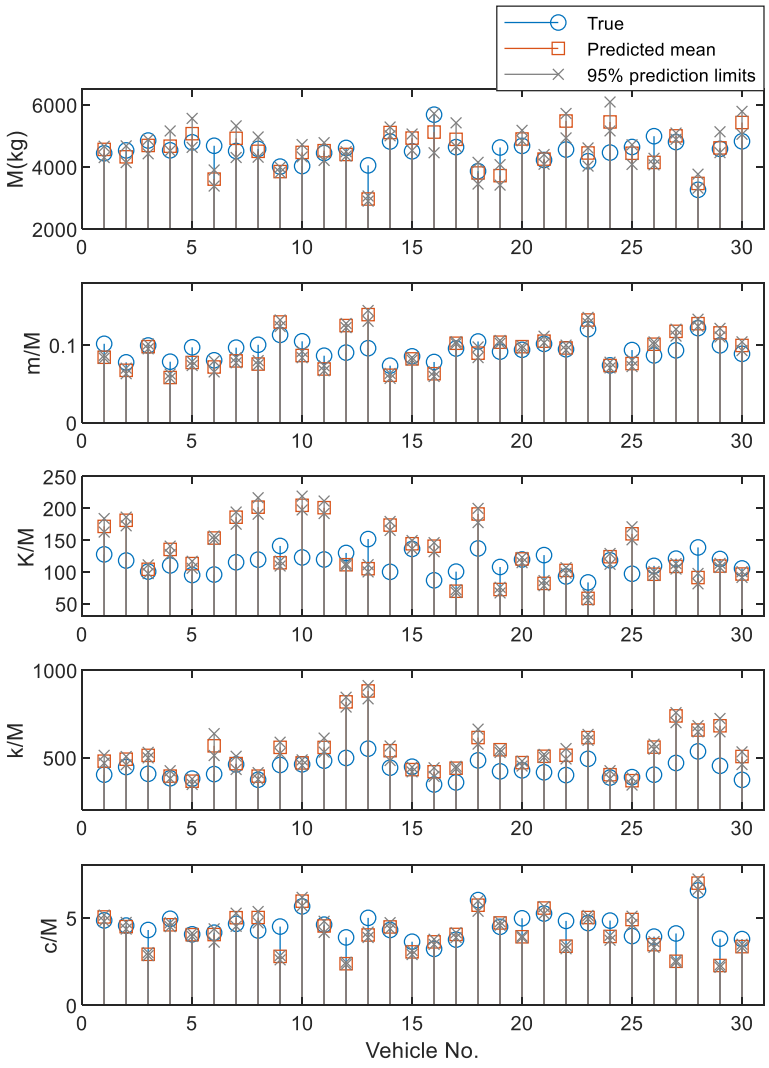

Figure 4.8 True and calculated (mean calculated and 95% prediction limits) sprung mass and normalized vehicle properties for the 3-D profile case.

4.4 Detection of Bridge Bearing Damage Using the Bayesian Analysis

4.4.1 Bearing damage

In this section, a simply supported bridge with different boundary conditions is considered to determine if bearing damage can be detected. Bearings allow supports to rotate freely but, when not functioning properly, can offer significant resistance to rotation. Rotational springs are added at each beam support to represent this resistance with stiffnesses $K_{rot,1}$ and $K_{rot,2}$, as shown in Figure 4.9 (Khan et al., 2021, Kliewer and Glisic, 2017).

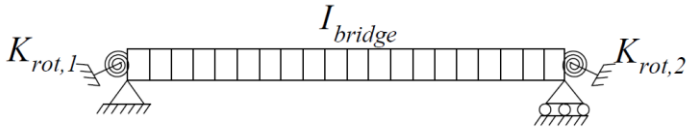

Figure 4.9 Bridge model with rotational springs.

The bearing damage level represented here, by the bearing spring stiffness. The values range from 0 (free to rotate) to infinity (fully fixed). Khan et al. (2021) defined five levels of damage: pinned, low, moderate, severe and fixed, related to the rotational stiffness values. Here, to test the bearing damage level of the bridge model, one vehicle is simulated crossing this bridge with different values of $K_{rot,1}$ and $K_{rot,2}$. Then, the area under the deflection curve is used as an indicator of changes in the bridge condition. $K_{rot,1}$ and $K_{rot,2}$ are kept equal, they start from 0Nm and increase to 10^{12} Nm, when the supports behave almost as though they are fully fixed. The areas under the deflection curve for different $K_{rot,1}$ and $K_{rot,2}$ values, are shown in Figure 4.10. It shows that there is no obvious change in the area under the deflection curve for values less than 10^{8} Nm. Between the about 10^{8} Nm and 10^{12} Nm area change significantly, indicating significant changes in support behaviour.

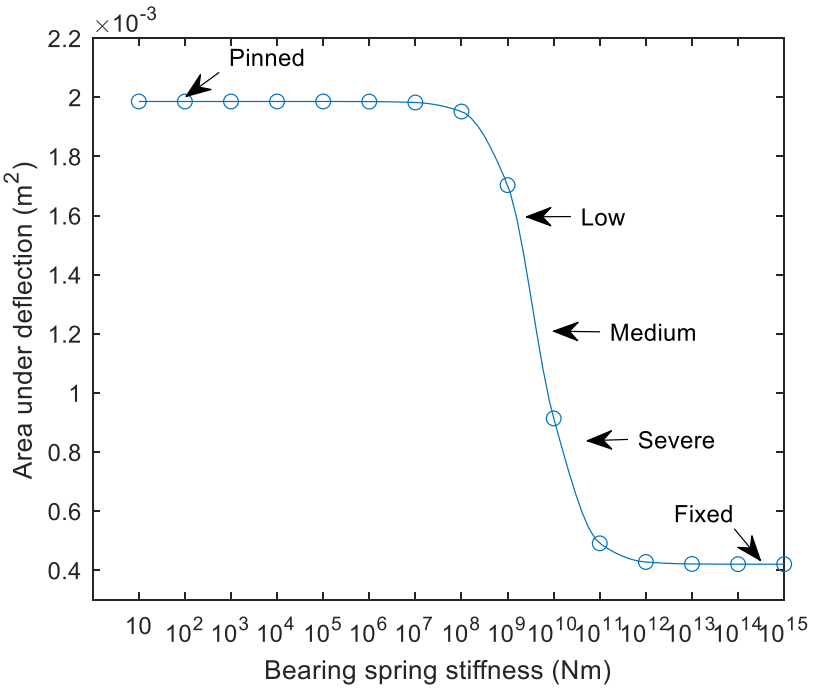

Figure 4.10 Area under the deflection curve for different values of rotational stiffness ($K_{rot,1} = K_{rot,2}$).

In this section, four different bearing damage states are chosen from which accelerations are generated: $K_{rot,1} = K_{rot,2} = \{0, 10^9, 10^{10}, 10^{12}\}$ Nm. The vehicle sprung mass M, bridge second moment of area I_{bridge} and bridge bearing stiffness $K_{rot,1}$ and $K_{rot,2}$ are solved from these 'measured' accelerations using the Bayesian approach. Here, it is assumed all 20 elements of the bridge are the same and have equal values of second moment of area I_{bridge}.

4.4.2 Data likelihood

Similar to Section 4.3.1, a simple independent Gaussian error model is used to calculate the deviations of the observed bridge deflections from the true values. For vehicle n, the sprung mass of the vehicle is deemed to be unknown but other vehicle property ratios are calculated from the off-bridge data, using the 2-D profile. The bridge second moment of area I_{bridge} and bearing stiffness values $K_{rot,1}$, $K_{rot,2}$ are also unknown. The Gaussian error model is formulated in term of the probability of a specific deflection:

$$p(\boldsymbol{w_n}|M_n, I_{bridge}, K_{rot,1}, K_{rot,2}) = \prod_{i=1}^{P} p(w_n(y_i; M_n)|W_n(y_i; M_n, I_{bridge}, K_{rot,1}, K_{rot,2}))$$

$$= \prod_{i=1}^{P} \frac{1}{\sqrt{2\pi\sigma_2^2}} \exp\left(-\frac{1}{2\sigma_2^2}(w_n(y_i; M_n) - W_n(y_i; M_n, I_{bridge}, K_{rot,1}, K_{rot,2}))^2\right)$$

$$= (2\pi\sigma_2^2)^{-0.5P}\exp(-\frac{1}{2\sigma_2^2}\sum_{i=1}^{P}(w_n(y_i;M_n) - W_n(y_i;M_n,I_{bridge},K_{rot,1},K_{rot,2}))^2)$$

(4.20)

where $W_n(y_i;M_n,I_{bridge},K_{rot,1},K_{rot,2})$ is the expected bridge deflection observed from a vehicle with M_n crossing the bridge with true properties, $I_{bridge},K_{rot,1},K_{rot,2}$. The term, $w_n(y_i;M_n)$ is the observed bridge deflection which is calculated from the 'measured' accelerations using the Inverse Newmark-Beta method. The Inverse Newmark-Beta method have already introduced in Chapter 2 and 3. It is used to calculate the apparent profile directly from 'measured' accelerations. In this chapter, the Inverse Newmark-Beta process is implemented in a simpler quarter-car model which is described in detail in Appendix B.

It is assumed that each vehicle's observations are independent:

$$p(\boldsymbol{w}|\boldsymbol{M_{1:N}},I_{bridge},K_{rot,1},K_{rot,2}) = \prod_{n=1}^{N} p(\boldsymbol{w_n}|M_n,I_{bridge},K_{rot,1},K_{rot,2})$$

$$= (2\pi\sigma_2^2)^{-0.5NP}\exp(-\frac{1}{2\sigma_2^2}\sum_{n=1}^{N}\sum_{i=1}^{P}(w_n(y_i;M_n) - W_n(y_i;M_n,I_{bridge},K_{rot,1},K_{rot,2}))^2$$

(4.21)

4.4.3 Priors

As in Section 4.3.2, a prior distribution $p(M_n|\varphi_M)$ is specified for each vehicle mass. It is the distribution of vehicle masses across the population of vehicles at the bridge site, which is usually assumed to be the same for each vehicle class. This distribution is described as normal and φ_M is its mean and variance. It is assumed that these priors are independent for each vehicle, so the prior for all masses $\boldsymbol{M_{1:N}} = (M_1, \dots M_N)$ is:

$$p(\boldsymbol{M_{1:N}}|\varphi_M) = \prod_{n=1}^{N} p((M_n|\varphi_M)) \tag{4.22}$$

where I_{bridge}, $K_{rot,1}$ and $K_{rot,2}$ are constant values across an interval. Their unform distribution over an interval (a,b) are assumed to have a density:

$$p(x) = \frac{1}{b-a}, a \le x \le b. \tag{4.23}$$

4.4.4 Posterior distribution

Similar to the posterior distribution described in Section 4.3.3, a posterior distribution for the bridge section is introduced here. By Bayes' Law, this is given in terms of the likelihood and prior terms by:

$$p\left(\boldsymbol{M}_{\mathbf{1}:\boldsymbol{N}}, I_{bridge}, K_{rot,1}, K_{rot,2} \,|\boldsymbol{w}\right)$$
$$\propto p\left(\boldsymbol{w}|\boldsymbol{M}_{\mathbf{1}:\boldsymbol{N}}, I_{bridge}, K_{rot,1}, K_{rot,2}\right)\left(\prod_{i=1}^{N} p\left((M_n|\varphi_M)\right)\right)p(I_{bridge})p(K_{rot,1})p(K_{rot,2}) \tag{4.24}$$

4.4.5 MCMC algorithm

For the four bridge bearing damage states, the fleet of vehicles used in section 4.3.4 is simulated crossing the bridge and vehicle accelerations are generated as 'measured' accelerations. Then, 2% noise is added to these accelerations and used in the MCMC process introduced below to determine the bridge second moment of area, I_{bridge}, the bearing damage levels $K_{rot,1}, K_{rot,2}$ and vehicle sprung mass value M at the same time.

As in section 4.3.4, Equation (4.24) is solved by MCMC, the process of which is described here.

1. Define an initial set of vehicle sprung masses, $\boldsymbol{M}_{\mathbf{1}:\boldsymbol{N}}^{(\mathbf{0})}$, and bridge properties $I_{bridge}^{(0)}$ $K_{rot,1}^{(0)}, K_{rot,2}^{(0)}$. Define parameters for the Gibbs sampler: $n_{iter} = 5000$, $s_M = 200$ kg, $s_I = 0.001\text{m}^4, s_k = 10^8\text{Nm}$ and $\sigma_2^2 = 10^{-11}$.

2. For each iteration j, for each vehicle n, generate proposed vehicle sprung masses, M_n

$$M_n' \sim N(M_n^{(j-1)}, s_M^2) \tag{4.25}$$

   a) Compute the expected $W_n\left(y_i; M_n', I_{bridge}^{(j-1)}, K_{rot,1}^{(j-1)}, K_{rot,2}^{(j-1)}\right)$ with these sprung masses in the Vehicle-Bridge-Interaction problem.
   b) Calculate $w_n(y_i; M_n)$ from the accelerations using the Inverse Newmark-Beta method.
   c) Compute the acceptance probability α_2 using Equation (4.26).

$$\alpha_2 = min\left\{1, \frac{\exp\left(-\frac{1}{2\sigma_2^2}\sum_{i=1}^{P}(w_n(y_i;M_n) - W_n\left(y_i;M_n',I_{bridge}^{(j-1)},K_{rot,1}^{(j-1)},K_{rot,2}^{(j-1)}\right))^2\right)}{\exp\left(-\frac{1}{2\sigma_2^2}\sum_{i=1}^{P}(w_n\left(y_i;M_n^{(j-1)}\right) - W_n\left(y_i;M_n^{(j-1)},I_{bridge}^{(j-1)},K_{rot,1}^{(j-1)},K_{rot,2}^{(j-1)}\right))^2\right)} \frac{p(M_n'|\varphi_M)}{p\left(M_n{}^{(j-1)}|\varphi_M\right)}\right\} \quad (4.26)$$

d) With probability α_2, the new generated sprung mass will be accepted and $M_n^{(j)} = M_n'$, otherwise, it will be rejected, and $M_n^{(j)} = M_n^{(j-1)}$.

e) Generate a proposed I_{bridge}' and proposed stiffnesses of the rotational springs, $k_{rot,1}, k_{rot,2}$

$$I_{bridge}' \sim N\left(I_{bridge}^{(j-1)}, s_I^2\right) \quad (4.27)$$

$$k_{rot,1} \sim N(K_{rot,1}^{(j-1)}, s_k^2) \quad (4.28)$$

$$k_{rot,2} \sim N(K_{rot,2}^{(j-1)}, s_k^2) \quad (4.29)$$

f) Compute the acceptance probability β_2 using Equation (4.30)

$$\beta_2 = min\left\{1, \frac{\exp\left(-\frac{1}{2\sigma_2^2}\sum_{n=1}^{N}\sum_{i=1}^{P}\left(w_n\left(y_i;M_n^{(j)}\right) - W_n\left(y_i;M_n^{(j)},\ I_{bridge}',k_{rot,1},k_{rot,2}\right)\right)^2\right)}{\exp\left(-\frac{1}{2\sigma_2^2}\sum_{n=1}^{N}\sum_{i=1}^{P}\left(w_n\left(y_i;M_n^{(j)}\right) - W_n\left(y_i;M_n^{(j)},I_{bridge}^{(j-1)},K_{rot,1}^{(j-1)},K_{rot,2}^{(j-1)}\right)\right)^2\right)} \frac{p(\ I_{bridge}^{'})}{p(\ I_{bridge}^{(j-1)})}\frac{p(k_{rot,1})}{p(K_{rot,1}^{(j-1)})}\frac{p(k_{rot,2})}{p(K_{rot,2}^{(j-1)}))}\right\} \quad (4.30)$$

As $I_{bridge}, K_{rot,1}, K_{rot,2}$ are constant values, $\frac{p(\ I_{bridge}')}{p(\ I_{bridge}^{(j-1)})} = \frac{p(k_{rot,1})}{p(K_{rot,1}^{(j-1)})} = \frac{p(k_{rot,2})}{p(K_{rot,2}^{(j-1)}))} = 1$

g) If probability β_2 is accepted, then $I_{bridge}^{(j)} = I_{bridge}', K_{rot,1}^{(j)} = k_{rot,1}, K_{rot,2}^{(j)} = k_{rot,2}$, Otherwise, $I_{bridge}^{(j)} = I_{bridge}^{(j-1)}, K_{rot,1}^{(j)} = K_{rot,1}^{(j-1)}, K_{rot,2}^{(j)} = K_{rot,2}^{(j-1)}$.

3. Repeat this process for the next iteration, $j \to j+1$.

4.4.6 Results for cases of bridge bearing damage

Here, the means of the MCMC samples are used as the calculated results. The calculated results for $\log_{10}(K_{rot,1})$, $\log_{10}(K_{rot,2})$ and I_{bridge} for the four damage states are shown in Table 4.2. For the second and third state, both the bearing spring stiffness values, K_{rot} and bridge second moment of area, I_{bridge} can be calculated with good accuracy. However, for the first and fourth damage states, only the bridge second moment of area, I_{bridge} can be calculated accurately. As shown in Figure 4.10, if the value of K_{rot} is less than 10^8, the bearing damage condition is low, and the support offers a negligible resistance to rotation. As a consequence, it is not possible to determine the stiffnesses accurately. Similarly, for values of K_{rot} greater than 10^{12}, the bearings are approaching being fully fixed and the stiffness is effectively infinite. The calculated sprung masses values (mean calculated and 95% prediction limits) for the second damage state are shown in Figure 4.11 and the calculated masses can be seen to be very close to the true masses.

Table 4.2 Calculated bridge properties by MCMC

		Damage State 1	Damage State 2	Damage State 3	Damage State 4
$\log_{10}(K_{rot,1})$	True	0	9	10	12
	Calculated	7.6	9.1	10.0	12.8
$\log_{10}(K_{rot,2})$	True	0	9	10	12
	Calculated	7.0	9.0	10.0	12.3
$I_{bridge}(\mathrm{m}^4)$	True	1.26	1.26	1.26	1.26
	Calculated	1.22	1.22	1.24	1.23

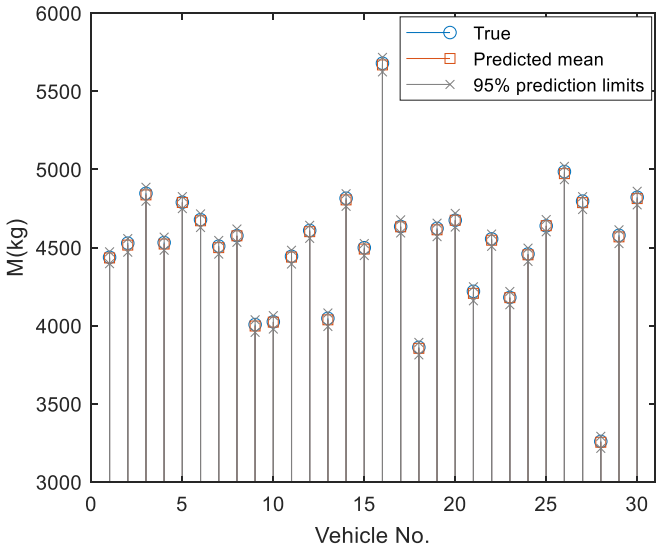

Figure 4.11 True and calculated sprung mass (mean calculated and 95% prediction limits) from MCMC for damage state 2.

4.5 Detection of Local Bridge Damage Using the MCMC Approach

4.5.1 Local damage

In this section, bridge damage is modelled as a local crack in the bridge. The crack is represented by a triangular loss in stiffness of one or multiple elements. As suggested by Sinha et al. (2002), the loss in stiffness affects a region equal to 1.5 times the beam depth on either side of the crack. A crack severity parameter, ϕ, is defined as the ratio of crack depth to overall beam depth and then related to the loss of bending stiffness. Here, the bridge model introduced in Section 4.2 is used and cracks with ϕ=10% and 5% are simulated at 10 m and 14 m from the left support of the bridge separately. For the beam model used here, the stiffness of four elements is affected by the crack. When the parameter, ϕ is 10%, the two elements near the crack have an 18% loss of stiffness, and other two adjacent elements have just 5% stiffness loss. If the parameter, ϕ is 5%, the respective element losses of stiffness are 10% and 3%. The Bayesian approach is then tested to determine if the presence of this damage can be detected.

4.5.2 Data likelihood

As in Section 4.3.1, a simple independent Gaussian error model is introduced. All vehicle property ratios are calculated using off-bridge data section except the sprung mass. The second moment of area, I_z for each of the 20 elements are assumed to be independent and unknown. The Gaussian error model for $\boldsymbol{I} = I_1, \dots, I_z, \dots, I_{20}$ is formulated here as:

$$p(\boldsymbol{w_n}|M_n, \boldsymbol{I}) = \prod_{i=1}^{P} p(w_n(y_i; M_n)|W_n(y_i; M_n, \boldsymbol{I}))$$

$$= \prod_{i=1}^{P} \frac{1}{\sqrt{2\pi\sigma_3^2}} \exp\left(-\frac{1}{2\sigma_3^2}(w_n(y_i; M_n) - W_n(y_i; M_n, \boldsymbol{I}))^2\right)$$

$$= (2\pi\sigma_3^2)^{-0.5P} \exp\left(-\frac{1}{2\sigma_3^2}\sum_{i=1}^{P}(w_n(y_i; M_n) - W_n(y_i; M_n, \boldsymbol{I}))^2\right)$$

(4.31)

where $W_n(y_i; M_n, \boldsymbol{I})$ is the expected bridge deflection observed from a vehicle with sprung mass, M_n, crossing the bridge with true second moment of area, $\boldsymbol{I}$. The term $w_n(y_i; M_n)$ is the observed bridge deflection which is calculated from the 'measured' accelerations using the

Inverse Newmark-Beta method. Each vehicle's observations are assumed to be independent and equally likely for all bridge deflection data:

$$p(\boldsymbol{w}|\boldsymbol{M_{1:N}}, \boldsymbol{I}) = \prod_{n=1}^{N} p(w_n|M_n, \boldsymbol{I}\,)$$

$$= (2\pi\sigma_3^2)^{-0.5NP} \exp(-\frac{1}{2\sigma_3^2} \sum_{n=1}^{N} \sum_{i=1}^{P} (w_n(y_i; M_n) - W_n(y_i; M_n, \boldsymbol{I}))^2$$

(4.32)

4.5.3 Priors and posterior

For a similar approach to Section 4.3.2, a prior distribution $p(M_n|\varphi_M)$ is specified for each vehicle mass. It is assumed that these priors are independent for each vehicle, so the prior for all masses, $\boldsymbol{M_{1:N}} = (M_1, \ldots M_N)$ is:

$$p(\boldsymbol{M_{1:N}}|\varphi_M) = \prod_{n=1}^{N} p\big((M_n|\varphi_M)\big)$$

(4.33)

A Gaussian process is used to simulate the bridge second moment of area, $\boldsymbol{I}$, with prior distribution:

$$p\,(\boldsymbol{I}) = \prod_{z=1}^{20} \sqrt{\frac{\tau_2}{2\pi}} \exp\,(-\frac{\tau_2}{2}(I_z - I_{z-1})^2)$$

(4.34)

where τ_2 is a smoothing parameter of $\boldsymbol{I}$.

Similar to the posterior distribution described in Section 4.3.3, a posterior distribution of the bridge section is introduced here. By Bayes' Law, this is given in terms of the likelihood and prior terms by:

$$p(\boldsymbol{M_{1:N}}, \boldsymbol{I}\,|\boldsymbol{w}) \propto p(\boldsymbol{w}|\boldsymbol{M_{1:N}}, \boldsymbol{I}\,) \left(\prod_{i=1}^{N} p\big((M_n|\varphi_M)\big) \right) p(\boldsymbol{I})$$

(4.35)

4.5.4 MCMC algorithm

The bridge is modelled in one healthy and four damaged states. Same fleets of vehicles are simulated crossing these five different states to generate 'measured' accelerations. To represent measurement inaccuracy, 2% noise is added to the 'measured' accelerations. Then the vehicle accelerations are used as input in the calculation process to calculate the bridge second moments of area and vehicle sprung mass.

Similar to Section 4.3.4, Equation (4.35) is solved by MCMC in the following process:

1. Define an initial set of vehicle sprung masses, $\boldsymbol{M}_{\boldsymbol{1:N}}^{(\boldsymbol{0})}$, and initial bridge properties $\boldsymbol{I}^{(0)} = I_1^{(0)}, \dots, I_z^{(0)}, \dots, I_{20}^{(0)}$. Define the parameters for the Gibbs sampler: $n_{iter} = 2{,}000$, $s_M = 200\text{kg}$, $s_I = 0.001\text{m}^4$, $\tau_2 = 10{,}000$ and $\sigma_3^2 = 10^{-11}$.
2. For each iteration j, and for each vehicle n, generate proposed vehicle sprung masses, M_n

$$M_n' \sim N(M_n^{(j-1)}, s_M^2) \tag{4.36}$$

   a) Compute $W_n\left(y_i; M_n', \boldsymbol{I}^{(j-1)}\right)$, which is the expected deflection arising from the fleet of vehicles in the Vehicle-Bridge-Interaction problem.
   b) Calculate $w_n(y_i; M_n')$ from 'measured' accelerations using the Inverse Newmark-Beta method.
   c) Compute the acceptance probability α_3 using Equation (4.37):

$$\alpha_3 = min\left\{1, \frac{\exp\left(-\frac{1}{2\sigma_3^2}\sum_{i=1}^{P}(w_n(y_i; M_n') - W_n\left(y_i; M_n', \boldsymbol{I}^{(j-1)}\right))^2\right)}{\exp\left(-\frac{1}{2\sigma_3^2}\sum_{i=1}^{P}(w_n\left(y_i; M_n^{(j-1)}\right) - W_n\left(y_i; M_n^{(j-1)}, \boldsymbol{I}^{(j-1)}\right))^2\right)} \frac{p(M_n|\varphi_M)}{p\left(M_n{}^{(j-1)}|\varphi_M\right)}\right\} \tag{4.37}$$

   d) With probability α_3, the new proposed value is accepted, if so let $M_n^{(j)} = M_n'$, else let $M_n^{(j)} = M_n^{(j-1)}$.

   e) In iteration j, for each bridge element z, $z = 1, \dots, 20$, generate a proposed bridge properties I_z' for I_z using Equation (4.38):

$$I_z' \sim N(I_z^{(j-1)}, s_I^2) \tag{4.38}$$

f) Let $\boldsymbol{I}^*$ be $\boldsymbol{I}^{\boldsymbol{current}}$ with $I_z^{(j-1)}$ being replaced by I_z'.

g) Compute all values of $W_n\left(y_i; M_n^{(j)}, \boldsymbol{I}^*\right)$ that are different from $W_n\left(y_i; M_n^{(j)}, \boldsymbol{I}^{\boldsymbol{current}}\right)$ for $i = 1, \ldots, P$ and $n = 1, \ldots, N$.

h) Compute the acceptance probability β_3. For z = 2, …, 19, use Equation (4.39):

$$\beta_3 = \frac{\exp\left(-\frac{1}{2\sigma_3^2}\sum_{n=1}^{N}\sum_{i=1}^{P}\left(w_n\left(y_i; M_n^{(j)}\right) - W_n\left(y_i; M_{1,n}^{(j)}, \boldsymbol{I}^*\right)\right)^2\right)}{\exp\left(-\frac{1}{2\sigma_3^2}\sum_{n=1}^{N}\sum_{i=1}^{P}\left(w_n\left(y_i; M_n^{(j)}\right) - W_n\left(y_i; M_{1,n}^{(j)}, \boldsymbol{I}^{\boldsymbol{current}}\right)\right)^2\right)} \times \frac{\exp\left(-\frac{\tau_2}{2}\left((I_z' - I_{z-1}^{(j-1)})^2 + (I_{z+1}^{(j-1)} - I_z')^2\right)\right)}{\exp\left(-\frac{\tau_2}{2}\left((I_z^{(j-1)} - I_{z-1}^{(j-1)})^2 + (I_{z+1}^{(j-1)} - I_z^{(j-1)})^2\right)\right)} \tag{4.39}$$

For $z = 1$, use Equation (4.40):

$$\beta_3 = \frac{\exp\left(-\frac{1}{2\sigma_3^2}\sum_{n=1}^{N}\sum_{i=1}^{P}\left(w_n\left(y_i; M_n^{(j)},\right) - W_n\left(y_i; M_{1,n}^{(j)}, \boldsymbol{I}^*\right)\right)^2\right)}{\exp\left(-\frac{1}{2\sigma_3^2}\sum_{n=1}^{N}\sum_{i=1}^{P}\left(w_n\left(y_i; M_n^{(j)},\right) - W_n\left(y_i; M_{1,n}^{(j)}, \boldsymbol{I}^{\boldsymbol{current}}\right)\right)^2\right)} \times \frac{\exp\left(-\frac{\tau_2}{2}\left((I_2^{(j-1)} - I_1')^2\right)\right)}{\exp\left(-\frac{\tau_2}{2}\left((I_2^{(j-1)} - I_1^{(j-1)})^2\right)\right)} \tag{4.40}$$

For $z = 20$, use Equation (4.41):

$$\beta_3 = \frac{\exp\left(-\frac{1}{2\sigma_3^2}\sum_{n=1}^{N}\sum_{i=1}^{P}\left(w_n\left(y_i; M_n^{(j)},\right) - W_n\left(y_i; M_n^{(j)}, \boldsymbol{I}^*\right)\right)^2\right)}{\exp\left(-\frac{1}{2\sigma_3^2}\sum_{n=1}^{N}\sum_{i=1}^{P}\left(w_n\left(y_i; M_n^{(j)},\right) - W_n\left(y_i; M_n^{(j)}, \boldsymbol{I}^{\boldsymbol{current}}\right)\right)^2\right)} \times \frac{\exp\left(-\frac{\tau_2}{2}\left((I_{20}' - I_{19}^{(j-1)})^2\right)\right)}{\exp\left(-\frac{\tau_2}{2}\left((I_{20}^{(j-1)} - I_{19}^{(j-1)})^2\right)\right)} \tag{4.41}$$

i) With probability β_3, the new proposed values are accepted, if yes, let $I_z^{(j-1)} = I_z'$, else $I_z^{(j-1)} = I_z^{(j)}$.

j) Update $\boldsymbol{I}^{\boldsymbol{current}}$ by replacing $I_z^{(j-1)}$ with $I_z^{(j)}$.

3. Let $\boldsymbol{I}^{(j)} = \boldsymbol{I}^{\boldsymbol{current}}$ and store the updated set of samples $M_1^{(j)}, \dots, M_n^{(j)}$ and bridge properties $\boldsymbol{I}^{(j)}$.

   Repeat this process for the next iteration, $j \to j + 1$.

4.5.5 Calculated results of detected bridge local damage

The calculated bridge second moment of area, $\boldsymbol{I}$ (mean calculated and 95% prediction limits) from the Bayesian updating algorithm, are shown in Figures 4.12. Figure 4.12(a) is the calculated vector $\boldsymbol{I}$ for the healthy state. It shows that the inferred second moments of area are within 1% to 2% of the true values. The calculated results for the damaged states are shown in Figures 4.12 (b) to (e). Despite the very small fleet (just 30 vehicles), the inferred values are quite close to the true ones and it is easy to estimate the levels and the location of the damage. Further, the method still works well with quite low damage levels. The calculated vehicle sprung masses (mean calculated and 95% prediction limits) are shown in Figures 4.13. It can be seen that these can be found with high accuracy. Clearly the mean vehicle mass is closely related to the mean deflection and the mean damage level of stiffness. If damage reduces stiffness, mean deflection increases for a given mean mass. It follows that the accuracy of the calculated sprung masses evident in the figure is contingent on a known mean mass. It is well known that the distribution of vehicle mass at a site is repeatable but this requires a large number of vehicles (OBrien et al., 2020).

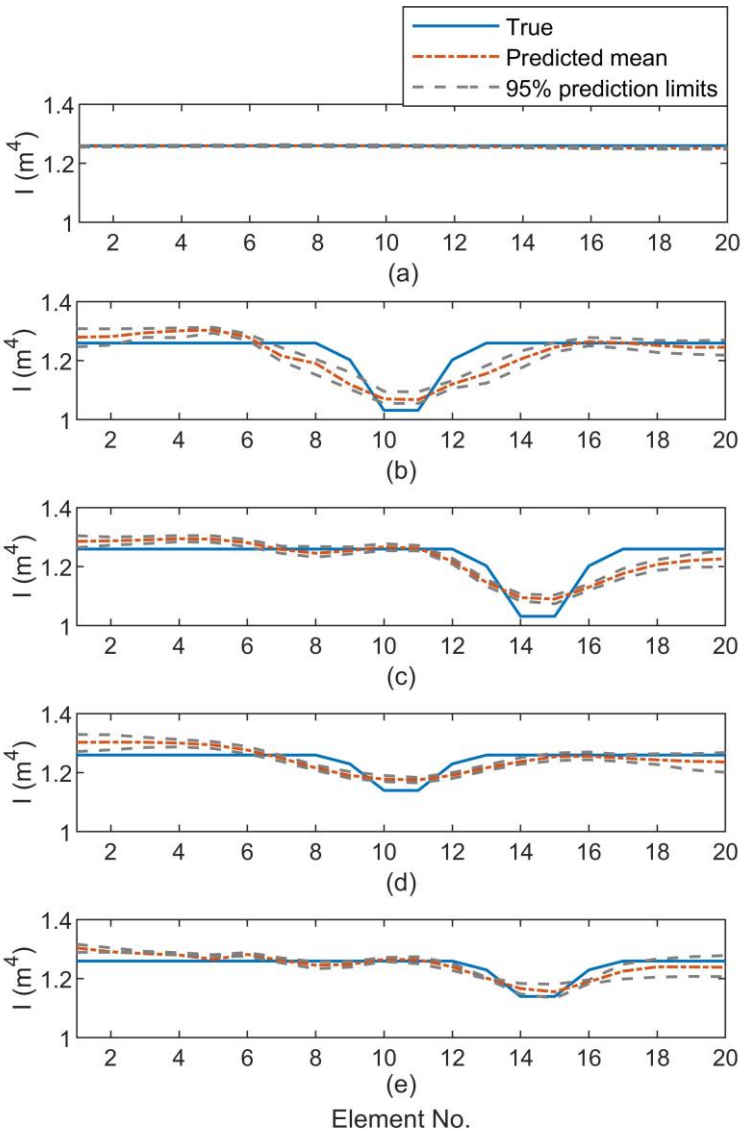

Figure 4.12 True and calculated (mean calculated and 95% prediction limits) 2nd moment of area, *I* of 20 elements: (a) healthy bridge; (b) damaged bridge (ϕ=10%, crack at 10 m); (c) damaged bridge (ϕ=10%, crack at 14 m); (d) damaged bridge (ϕ=5%, crack at 10 m); (e) damaged bridge (ϕ=5%, crack at 14 m).

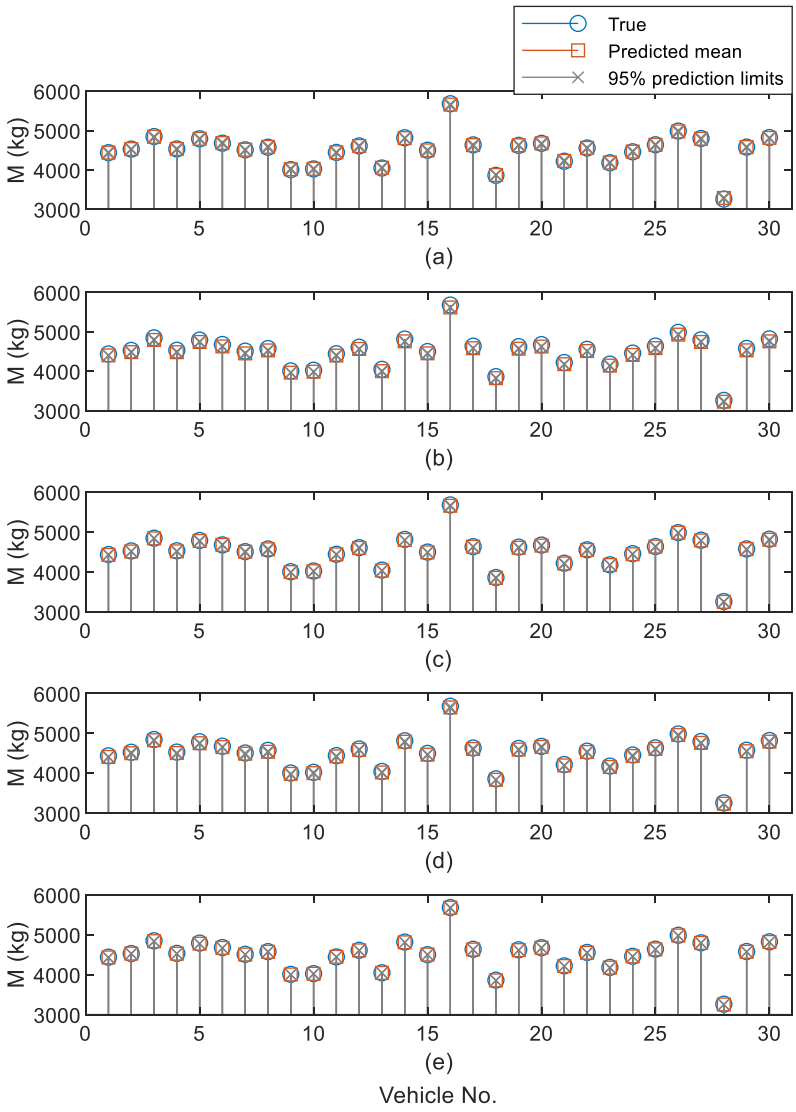

Figure 4.13 True and calculated sprung mass (mean calculated and 95% prediction limits): (a) healthy bridge; (b) damaged bridge (ϕ=10%, crack at 10 m); (c) damaged bridge (ϕ=10%, crack at 14 m); (d) damaged bridge (ϕ=5%, crack at 10 m); (e) damaged bridge (ϕ=5%, crack at 14 m).

4.6 Discussion and Conclusions

This chapter uses a Bayesian approach to analyze data from a fleet of uncontrolled but instrumented vehicles to estimate road profile, calibrate the vehicles and detect bridge damage. In the Bayesian approach, a 'point' or best estimate is determined by quantifying the uncertainty in the estimation. Using off-bridge data, the road profile and most of the vehicle properties are calculated from the vehicle accelerations. The inferred profile has been found to be very close to the true profile, even allowing for measurement noise. The normalized vehicle properties can

also be determined from this process with reasonable accuracy, except for the sprung mass (gross vehicle weight) of each vehicle. Both 2D and 3D road profiles are considered, the latter allowing for uncertainty in the lateral track position on the road surface. It is found that a mean of this 3-D profile can be calculated which is close to the true mean profile. However, this uncertainty significantly affects the accuracy of the vehicle calculation process.

Numerical simulations are used to test the ability of the Bayesian approach to detect bridge damage. Here, the on-bridge vehicle accelerations are used to determine the bridge properties, vehicle sprung masses and the spring stiffnesses of the bearings. Four different bridge damage states are considered with different bearing damage conditions. It is found that the bridge properties and spring stiffnesses can be calculated with good accuracy using this Bayesian approach. The calculated bearing spring stiffnesses can be used to estimate the bearing damage condition.

Local damage is also considered in the form of cracks in the bridge. The second moments of area of each of the 20 elements of the bridge are calculated. Even with a very small vehicle fleet, the levels and locations of the crack damage are found and the vehicle sprung masses. Even for low levels of damage, the method works well (with about 3% error). The results are insensitive to random noise in the measurements.

It is acknowledged that the results are based on simple numerical models and that there will be challenges in making this concept operational for real vehicles in the field. In particular, the vehicle model is a simple quarter car which avoids the complexity of an acceleration resulting from multiple simultaneous axle excitations. It is believed that this problem can be addressed to separate the contributions into their component parts. It is acknowledged that the road surface profile on the bridge, assumed to be smooth in this study, may have a significant effect and that it would be desirable to demonstrate the ability to detect lower levels of damage. To some degree at least, accuracy will be improved by considering larger fleets of vehicles – perhaps numbering in thousands – compared to the fleet of 30 considered here. Further, the calibration process should be greatly improved by accessing potentially hundreds of kilometers of data, compared to the 20 m approach length assumed here. It is anticipated that the accuracy of vehicle location data will be challenging due to the resolution of commercially available GPS sensors. However, it may be possible to improve this accuracy by using optimization algorithms to synchronize data from different vehicles. The purpose of this study has been to establish the principle of vehicle fleet monitoring of bridges. It is concluded that, while many challenges

remain, this approach appears to have considerable potential. Just one vehicle is considered on the bridge in this section but other traffic on the bridge may influence the inferred results. Since a fleet of vehicles are used, it is possible to discount the particular cases when more than one vehicle is on the bridge simultaneously. The influence of other traffic on the bridge during the measurements should be investigated in the future. A potential damage scenario consisting of a combination of different damages is not considered in this section. Each damage may influence the bridge behavior and it may be difficult to sperate them. Further work on this issue is needed in the future.

Chapter 5 – Conclusions

Chapter 5 – Conclusion

5.1 Summary

In this chapter, the principal findings and contributions to the state-of-the-art of this thesis are summarised. Figure 1.1 provides a summary of this thesis with the links between the key contributions of this work and the different chapters. In Chapter 2, an Inverse Newmark-Beta integration method is developed to determine road profile using passing vehicle measurements which is accurate and computationally efficient. Then the vehicle fleet monitoring concept is proposed. Here, the Inverse Newmark-Beta integration and the Cross Entropy (CE) optimization are used together to solve vehicle fleet monitoring problem with unknown vehicle properties. Sprung mass and half car vehicle models are simulated separately. The results show that the calculated road profile is close to the true profile. For the vehicle properties, the property ratios are accurately calculated but the vehicle masses are not. Clearly vehicle mass affects its frequency, meaning that some information exists in the data on mass. However, the relationship between vehicle mass and the signal is found to be weak so it is difficult to determine mass accurately. Noise is added to the acceleration and velocity responses to allow for possible measurement inaccuracy. It is found that increasing noise levels have an influence on the calculated results, but a reasonable level of accuracy is achieved. The influence of noise may be much reduced if the populations are larger.

In Chapter 3, the vehicle fleet monitoring concept is further developed, this time for a flexible railway track calculation and railway bridge damage detection. A 4-axle railway carriage and train/track/bridge dynamic interaction model is used. The apparent profile (AP) of the track can be determined from bogie vertical accelerations and angular velocities using the Inverse Newmark-Beta algorithm. The numerical inaccuracies tend to accumulate which results in a 'drift' in the calculated AP over time/distance. This is not considered to be a significant issue as track damage or deterioration is generally evident over short lengths. Combining the Inverse Newmark-Beta method with CE optimisation, the APs of the track and vehicle properties can be calculated using batches of trains. There are 50 trains in each batch which have constant vehicle properties except mass, moment of inertia and speed. The calculated APs and vehicle properties are very close to the true values. A new method is proposed to determine the moving reference influence line (MR-IL) from the moving reference deflections. Using a 2-axle half-car and simply supported beam model, the results show that the MR-IL is a good indicator of bridge damage level. As the MR-IL is essentially a static deflection function, it relates directly

to overall bridge stiffness. For this reason, it is unsurprising that it is directly correlated with overall bridge damage, represented as a loss of stiffness. Though bridge frequencies may influence the calculated MR-IL values, it can still detect the level of damage with reasonably accuracy. A blind test with an independent research group is used to validate the results. A culvert is simulated as a railway bridge. The independent research group use a 4-axle railway carriage model to generate 'measurements'. The 4-axle railway carriage model and the 2-axle half-car are used by UCD to calculate MR-IL, derived from the 'measured' bogie vertical accelerations and angular velocities. The results show that the calculated MR-IL is a good indictor to detect the damage levels of the bridge.

In Chapter 4, the vehicle fleet monitoring concept is applied again to profiles and bridges, this time using the Bayesian approach. Here, 2-D and 3-D road profiles are tested separately. For the 2-D profile, given accelerations from vehicles, the road profile and vehicle properties ratios can be determined with good accuracy. Same as before, vehicle mass cannot be determined accurately from the off-bridge data but it can be solved using the on-bridge data, assuming that the mean vehicle mass is known. For the 3-D case, the calculated profile is close to the true mean profile. However, the calculated vehicle properties are not particularly accurate – clearly they are sensitive to deviations in the lateral vehicle position. The Bayesian approach is also used to detect bridge damage. It can detect, locate and quantify the bridge damage with reasonable accuracy. For bridge bearing damage, the Bayesian approach estimates the bridge segment second moments of area and bearing spring stiffnesses at each support. If the bearing damage condition is too low or too high, it is not possible to determine the stiffnesses accurately. However the calculated results can still determine the healthy/damaged state of the bridge bearing. Also, the sprung masses of the individual vehicles can be found, assuming a knowledge of the mean vehicle mass for the site. The vehicle mass is closely related to the bridge deflection. Further, the masses of the vehicle fleet can be solved in the bridge section. The Bayesian approach is also used to detect local crack damage. The results show that it can determine the levels and locations of crack damage with reasonable accuracy. The results are reasonably insensitive to random noise in the (simulated) measurements. The Bayesian approach is a good way to improve robustness of the calculation compared to previous work.

This thesis develops a fleet monitoring concept for road/railway profiles and bridge damage detection. Fleet monitoring is shown to have good potential to find road/railway profiles and, through the apparent profile concept, to monitor bridge health. Clearly using a large fleet of

regular vehicles allows a great deal of information to be combined which can greatly increase accuracy. The main contributions of the thesis are as follows:

1. Development of the Inverse Newmark-Beta concept.
2. Solving the calibration problem for the fleet of vehicles with unknown properties.
3. Developing the concept of a Moving Reference Influence Line.
4. Using Bayesian Updating to greatly improve robustness and efficiency and to allow for continuous updating of the profile, vehicle properties or bridge properties.

The methods are validated and tested with different vehicles (sprung-mass/quarter-car/half-car/4-axle, road/rail), different profiles (rigid/deformable, 2-D/3-D), different bridges (simply supported/with rotational stiffness/culvert) and different bridge damage types (global/bearing damage/local crack).

5.2 Limitations and Assumptions

A limitation of this work has been the lack of a 3D numerical analysis. The thesis uses 1D beam finite elements and simplified 2D planar vehicle models. The suspension system has been modelled as a linear spring and damper, and the tyres have been modelled as linear springs. Another limitation is that the drive-by monitoring methods are examined in this thesis using numerical models only. Experimental laboratory-scale models and full-scale field tests have not been carried out. For bridge condition monitoring, just one vehicle or carriage is assumed on the bridge. Other traffic on the bridge during the measurements is not considered. Further, combinations of different damage states on the bridge are not considered. In this thesis, simply supported bridges are assumed in most cases. In Section 3, a culvert bridge model is also used. While other bridge forms are not considered, it seems reasonable to assume that they may also work. Nevertheless, there is scope for further work in this area.

In each contribution, just one scanning frequency is used - different scanning rate should be considered. In this thesis the simulated measurements used are acceleration and velocity. The simulation in this thesis suggests that a small fleet will give some useful information, but a larger fleet would clearly be better. The measurements can be collected by accelerometers and gyroscopes mounted on the vehicles. Different locations are assumed in different sections. The sensors are attached to the bogie of the train model, and they are attached to the sprung mass of a vehicle model. Determining the most effective location of these sensors is one of the potential challenges. The data can be collected and stored locally in the vehicle. For trains, on board Wi-

Fi could collect the data locally and transfer it to the Cloud. It may also be possible to collect these data from a fleet of vehicles in real time using 5G technology

5.3 Recommendations for Future Research

As these works are just examined by numerical model, field tests will ultimately be necessary to give road owners/managers the confidence to implement the concept of fleet monitoring in real-world applications.

In this thesis, the vehicle models are simplified 2D planar sprung-mass, quarter-car, half car and railway carriage model. Some vehicle components have been modelled as linear systems (suspension system and tyres). Significant improvements can be made to extend these models to consider non-linear behaviour of some of the vehicle components and extend the vehicle models to three dimensions.

The fleet monitoring concept can solve many infrastructure health monitoring problems using vehicle drive-by data. The concept is to harvest this data from regular vehicles using the network, and to use it to infer information on road/rail and bridge condition. However, the quantity of data involved is potentially immense and research may be needed on the development of an Edge Computing strategy for data processing, storage and transfer.

References

ANON 2010. Malahide Viaduct - Reinstatement. *Journal of the Irish Railway Record Society,* 24 (171)**,** 2–3.

BELAY, A., OBRIEN, E. & KROESE, D. 2008. Truck fleet model for design and assessment of flexible pavements. *Journal of Sound and Vibration,* 311**,** 1161-1174.

BEN HASSEN, D., MILADI, M., ABBES, M. S., BASLAMISLI, S. C., CHAARI, F. & HADDAR, M. 2019. Road profile estimation using the dynamic responses of the full vehicle model. *Applied Acoustics,* 147**,** 87-99.

BLAB, R. & LITZKA, J. Measurements of the lateral distribution of heavy vehicles and its effects on the design of road pavements. 4th International Symposium on Heavy VehicleWeights and Dimensions, 25–29 June 1995 Ann Arbor, MI, USA. 389-395.

BOTEV, Z. & KROESE, D. P. 2004. Global likelihood optimization via the CE method, with an application to mixture models. *Proceedings of the 36th conference on Winter simulation.* Washington, DC, USA: IEEE.

CANTERO, D., ARVIDSSON, T., OBRIEN, E. J. & KAROUMI, R. 2016. Train–track–bridge modelling and review of parameters. *Structure and Infrastructure Engineering,* 12**,** 1051-1064.

CANTERO, D. & BASU, B. 2015. Railway infrastructure damage detection using wavelet transformed acceleration response of traversing vehicle. *Structural Control and Health Monitoring,* 22**,** 62-70.

CASERO, M., GONZALEZ, A. & COVIAN, E. 2014. Finite Element Updating using Cross-Entropy combined with Random Field Theory. *The Twelfth International Conference on Computational Structures Technology (CST 2014).* Naples, Italy: Civil-Comp Press.

DU, R., QIU, G., GAO, K., HU, L. & LIU, L. 2020. Abnormal Road Surface Recognition Based on Smartphone Acceleration Sensor. *Sensors (Basel),* 20.

ELHATTAB, A., UDDIN, N. & OBRIEN, E. J. 2016. Drive-by bridge damage monitoring using Bridge Displacement Profile Difference. *Journal of Civil Structural Health Monitoring,* 6**,** 839-850.

ERGUN, M., IYINAM, S. & IYINAM, A. F. 2005. Prediction of Road Surface Friction Coefficient Using Only Macro- and Microtexture Measurements. *Journal of Transportation Engineering,* 131**,** 311-319.

FAURIAT, W., MATTRAND, C., GAYTON, N., BEAKOU, A. & CEMBRZYNSKI, T. 2016. Estimation of road profile variability from measured vehicle responses. *Vehicle System Dynamics,* 54**,** 585-605.

FITZGERALD, P. C., MALEKJAFARIAN, A., CANTERO, D., OBRIEN, E. J. & PRENDERGAST, L. J. 2019. Drive-by scour monitoring of railway bridges using a wavelet-based approach. *Engineering Structures,* 191**,** 1-11.

FLINTSCH, G. W., FERNE, B., DIEFENDERFER, B., KATICHA, S., BRYCE, J. & NELL, S. 2012. Valuation of traffic speed continuous deflection devices. *91st Annual Meeting, Transport Research Board.* USA.

FOX, A., KUMAR, B. V. K. V., CHEN, J. & BAI, F. 2017. Multi-Lane Pothole Detection from Crowdsourced Undersampled Vehicle Sensor Data. *IEEE Transactions on Mobile Computing,* 16**,** 3417-3430.

FUJINO, Y. & SIRINGORINGO, D. M. 2011. Bridge monitoring in Japan: the needs and strategies. *Structure and Infrastructure Engineering,* 7**,** 597-611.

GELFAND, A. E. & SMITH, A. F. M. 1990. Sampling-based approaches to calculating marginal densities. *Journal ofthe American Statistical Association,* 85**,** 398-490.

GOLDBERG, D. E. & HOLLAND, J. H. 1988. Genetic algorithms and machine learning. *Machine Learning,* 3**,** 95-99.

GONZALEZ, A., OBRIEN, E. J., LI, Y. Y. & CASHELL, K. 2008. The use of vehicle acceleration measurements to estimate road roughness. *Vehicle System Dynamics,* 46**,** 483-499.

GONZALEZ, A., OBRIEN, E. J. & MCGETRICK, P. J. 2012. Identification of damping in a bridge using a moving instrumented vehicle. *Journal of Sound and Vibration,* 331**,** 4115-4131.

GUEVARA, L. & AUAT CHEEIN, F. 2020. The Role of 5G Technologies: Challenges in Smart Cities and Intelligent Transportation Systems. *Sustainability,* 12.

HARRIS, N. K., GONZALEZ, A., OBRIEN, E. J. & MCGETRICK, P. 2010. Characterisation of pavement profile heights using accelerometer readings and a combinatorial optimisation technique. *Journal of Sound and Vibration,* 329**,** 497-508.

HARRIS, N. K., OBRIEN, E. J. & GONZALEZ, A. 2007. Reduction of bridge dynamic amplification through adjustment of vehicle suspension damping. *Journal of Sound and Vibration,* 302**,** 471-485.

IMINE, H., DELANNE, Y. & M'SIRDI, N. K. 2006. Road profile input estimation in vehicle dynamics simulation. *Vehicle System Dynamics,* 44**,** 285-303.

ISEN13848 2018. Railway applications - Track - Track geometry quality - Part 2: Measuring systems - Track recording vehicles- CEN European Committee for Standardisation.

ISO8606 1995. Mechanical vibration—Road surface profiles—Reporting of measured data.

IWNICKI, S. 1998. Manchester Benchmarks for Rail Vehicle Simulation. *Vehicle System Dynamics,* 30**,** 295-313.

KEENAHAN, J. C. & OBRIEN, E. J. 2018. Drive-by damage detection with a TSD and time-shifted curvature. *Journal of Civil Structural Health Monitoring,* 8**,** 383-394.

KHAN, M. A., MCCRUM, D. P., OBRIEN, E. J., BOWE, C., HESTER, D., MCGETRICK, P. J., O'HIGGINS, C., CASERO, M. & PAKRASHI, V. 2021. Re-deployable sensors for modal estimates of bridges and detection of damage-induced changes in boundary conditions. *Structure and Infrastructure Engineering***,** 1-15.

KIM, G.-W., KANG, S.-W., KIM, J.-S. & OH, J.-S. 2019. Simultaneous estimation of state and unknown road roughness input for vehicle suspension control system based on discrete Kalman filter. *Proceedings of the Institution of Mechanical Engineers, Part D: Journal of Automobile Engineering,* 234**,** 1610-1622.

KLIEWER, K. & GLISIC, B. 2017. Normalized Curvature Ratio for Damage Detection in Beam-Like Structures. *Frontiers in Built Environment,* 3.

LEE, P. M. 2012. *Bayesian Statistics: An Introduction,* London, UK, John Wiley & Sons Ltd.

LEI, X. & NODA, N. A. 2002. Analyses of dynamic response of vehicle and track coupling system with random irregularity of track vertical profile. *Journal of Sound and Vibration,* 258**,** 147–165.

LI, J., ZHU, X., LAW, S.-S. & SAMALI, B. 2020. A Two-Step Drive-By Bridge Damage Detection Using Dual Kalman Filter. *International Journal of Structural Stability and Dynamics,* 20.

LI, W., JIANG, Z., WANG, T. & ZHU, H. 2014. Optimization method based on Generalized Pattern Search Algorithm to identify bridge parameters indirectly by a passing vehicle. *Journal of Sound and Vibration,* 333**,** 364-380.

LI, Y. 2006. *Factors affecting the dynamic interaction of bridges and vehicle loads.* Ph.D, University College Dublin.

LOU, P. 2007. Finite element analysis for train–track–bridge interaction system. *Archive of Applied Mechanics,* 77**,** 707-728.

LU, F., KENNEDY, D., WILLIAMS, F. W. & LIN, J. H. 2008. Symplectic analysis of vertical random vibration for coupled vehicle–track systems. *Journal of Sound and Vibration,* 317**,** 236-249.

LYONS, R. G. 2011. *Understanding digital signal processing,* Boston, MA, USA, Prentice Hall.

MA, L., LI, Y., LI, J., WANG, C., WANG, R. & CHAPMAN, M. 2018. Mobile Laser Scanned Point-Clouds for Road Object Detection and Extraction: A Review. *Remote Sensing,* 10**,** 1531.

MALEKJAFARIAN, A., GOLPAYEGANI, F., MOLONEY, C. & CLARKE, S. 2019. A Machine Learning Approach to Bridge-Damage Detection Using Responses Measured on a Passing Vehicle. *Sensors (Basel),* 19.

MALEKJAFARIAN, A., MARTINEZ, D. & OBRIEN, E. J. 2017. Pavement condition measurement at high velocity using a TSD. *27th annual European Safety and Reliability Conference (ESREL 2017).* Portoroz, Slovenia: CRC Press.

MALEKJAFARIAN, A., MCGETRICK, P. J. & OBRIEN, E. J. 2015. A review of indirect bridge monitoring using passing vehicles. *Shock and Vibration,* 2015**,** 1-16.

MEI, Q., GüL, M. & SHIRZAD-GHALEROUDKHANI, N. 2020. Towards smart cities: crowdsensing-based monitoring of transportation infrastructure using in-traffic vehicles. *Journal of Civil Structural Health Monitoring,* 10**,** 653-665.

MICU, A. E., OBRIEN, E. J., BOWE, C., FITZGERALD, P. & PAKRASHI, V. 2022. Bridge Damage and Repair Detection using an Instrumented Train. *Journal of Bridge Engineering,* 27**,** 1-12.

NGUYEN, G. K., GOICOLEA, R. M. & GABALDON, C. F. 2012. Comparison of dynamic effects of high-speed traffic load on ballasted track using a simplified two-dimensional and full three-dimensional model. *Proceedings of the Institution of Mechanical Engineers, Part F: Journal of Rail and Rapid Transit,* 228**,** 128–142.

O'HAGAN, A. & FORSTER, J. 2004. *Kendall's Advanced Theory of Statistics, volume 2B: Bayesian Inference,* London, UK, Hodder Arnold.

O'LEARY, D. E. 2013. Exploiting Big Data from Mobile Device Sensor-Based Apps: Challenges and Benefits. *Mis Quarterly Executive,* 12**,** 179-187.

OBRIEN, E. J., BOWE, C., QUIRKE, P. & CANTERO, D. 2016. Determination of longitudinal profile of railway track using vehicle-based inertial readings. *Proceedings of the Institution of Mechanical Engineers, Part F: Journal of Rail and Rapid Transit,* 231**,** 518-534.

OBRIEN, E. J., BROWNJOHN, J. M. W., HESTER, D., HUSEYNOV, F. & CASERO, M. 2020. Identifying damage on a bridge using rotation-based Bridge Weigh-In-Motion. *Journal of Civil Structural Health Monitoring,* 11**,** 175-188.

OBRIEN, E. J. & KEENAHAN, J. 2015. Drive-by damage detection in bridges using the apparent profile. *Structural Control and Health Monitoring,* 22**,** 813-825.

OBRIEN, E. J., MCGETRICK, P. J. & GONZALEZ, A. 2014. A drive-by inspection system via vehicle moving force identification. *Smart Structures and Systems,* 13**,** 821-848.

OBRIEN, E. J., QUILLIGAN, M. & KAROUMI, R. 2006. Calculating an influence line from direct measurements. *Proceedings of the Institution of Civil Engineers-Bridge Engineering,* 159**,** 31-34.

OBRIEN, E. J., QUIRKE, P., BOWE, C. & CANTERO, D. 2017. Determination of railway track longitudinal profile using measured inertial response of an in-service railway vehicle. *Structural Health Monitoring,* 17**,** 1425-1440.

PAIXAO, A., FORTUNATO, E. & CALCADA, R. 2019. Smartphone's sensing capabilities for on-board railway track monitoring: Structural performance and geometrical degradation assessment. *Advances in Civil Engineering,* 2019**,** 1-13.

QUIRKE, P., BOWE, C., OBRIEN, E. J., CANTERO, D., ANTOLIN, P. & GOICOLEA, J. M. 2017. Railway bridge damage detection using vehicle-based inertial measurements and apparent profile. *Engineering Structures,* 153**,** 421-442.

QUIRKE, P., CANTERO, D., OBRIEN, E. J. & BOWE, C. 2016. Drive-by detection of railway track stiffness variation using in-service vehicles. *Proceedings of the Institution of Mechanical Engineers, Part F: Journal of Rail and Rapid Transit,* 231**,** 498-514.

RAKOCZY, A. M., OTTER, D. E., MALONE, J. J. & FARRITOR, S. 2016. Railroad Bridge Condition Evaluation Using Onboard Systems. *Journal of Bridge Engineering,* 21.

RAKOCZY, A. M., SHU, X. & OTTER, D. 2017. Vehicle–Track–Bridge Interaction Modeling and Validation for Short Span Railway Bridges. *Transportation Research Record: Journal of the Transportation Research Board,* 2642**,** 127-138.

RUBINSTEIN, R. Y. & KROESE, D. P. 2004. *The cross-entropy method: A unified approach to combinatorial optimization, monte-carlo simulation and machine learning,* New York, Springer-Verlag.

SATTAR, S., LI, S. & CHAPMAN, M. 2018. Road Surface Monitoring Using Smartphone Sensors: A Review. *Sensors (Basel),* 18.

SAYERS, M. W. & KARAMIHAS, S. M. 1996. *Interpretation of road profile roughness data,* University of Michigan Transportation Research Institute, UMTRI-96-19.

SAYERS, M. W. & KARAMIHAS, S. M. 1998. *The little book of profiling,* University of Michigan Transportation Research Institute, UMTRI-96-19.

SINHA, J. K., FRISWELL, M. I. & EDWARDS, S. 2002. Simplified Models for the Location of Cracks in Beam Structures Using Measured Vibration Data. *Journal of Sound and Vibration,* 251**,** 13-38.

SOUZA, V. M. A., GIUSTI, R. & BATISTA, A. J. L. 2018. Asfault: A low-cost system to evaluate pavement conditions in real-time using smartphones and machine learning. *Pervasive and Mobile Computing,* 51**,** 121-137.

TAN, C., UDDIN, N., OBRIEN, E. J., MCGETRICK, P. J. & KIM, C.-W. 2019. Extraction of Bridge Modal Parameters Using Passing Vehicle Response. *Journal of Bridge Engineering,* 24.

TANNER, M. A. 1996. *Tools for statistical inference,* New York, Springer-Verlag.

WALSH, B. J. & GONZALEZ, A. 2009. Assessment of the Condition of a Beam Using a Static Loading Test. *Key Engineering Materials,* 413-414**,** 269-276.

WANG, Z., DONG, M., QIN, Y., DU, Y., ZHAO, F. & GU, L. 2016. Suspension system state estimation using adaptive Kalman filtering based on road classification. *Vehicle System Dynamics,* 55**,** 371-398.

WEI, X., LIU, F. & JIA, L. 2016. Urban rail track condition monitoring based on in-service vehicle acceleration measurements. *Measurement,* 80**,** 217-228.

WESTON, P., ROBERTS, C., YEO, G. & STEWART, E. 2015. Perspectives on railway track geometry condition monitoring from in-service railway vehicles. *Vehicle System Dynamics,* 53**,** 1063-1091.

WILSON, S. P., HARRIS, N. K. & OBRIEN, E. J. 2006. The use of Bayesian statistics to predict patterns of spatial repeatability. *Transportation Research Part C: Emerging Technologies,* 14**,** 303-315.

WU, C., WANG, Z., HU, S., LEPINE, J., NA, X., AINALIS, D. & STETTLER, M. 2020. An Automated Machine-Learning Approach for Road Pothole Detection Using Smartphone Sensor Data. *Sensors (Basel),* 20.

YANG, Y. B. & LIN, C. W. 2005. Vehicle–bridge interaction dynamics and potential applications. *Journal of Sound and Vibration,* 284**,** 205-226.

YANG, Y. B., LIN, C. W. & YAU, J. D. 2004. Extracting bridge frequencies from the dynamic response of a passing vehicle. *Journal of Sound and Vibration,* 272**,** 471-493.

YANG, Y. B., WANG, Z.-L., SHI, K., XU, H. & WU, Y. T. 2020a. State-of-the-Art of the Vehicle-Based Methods for Detecting the Various Properties of Highway Bridges and Railway Tracks. *International Journal of Structural Stability and Dynamics,* 20**,** 2041004.

YANG, Y. B., WANG, Z. L., WANG, B. Q. & XU, H. 2020b. Track modulus detection by vehicle scanning method. *Acta Mechanica,* 231**,** 2955-2978.

YANG, Y. B. & YANG, J. P. 2018. State-of-the-Art review on modal identification and damage detection of bridges by moving test vehicles. *International Journal of Structural Stability and Dynamics,* 18**,** 1850025.

ZANG, K., SHEN, J., HUANG, H., WAN, M. & SHI, J. 2018. Assessing and Mapping of Road Surface Roughness based on GPS and Accelerometer Sensors on Bicycle-Mounted Smartphones. *Sensors (Basel),* 18.

ZHAI, W. M., WANG, K. Y. & LIN, J. H. 2004. Modelling and experiment of railway ballast vibrations. *Journal of Sound and Vibration,* 270**,** 673-683.

ZHANG, Y., WANG, L. & XIANG, Z. 2012. Damage detection by mode shape squares extracted from a passing vehicle. *Journal of Sound and Vibration,* 331**,** 291-307.

ZHAO, B., NAGAYAMA, T. & XUE, K. 2019. Road profile estimation, and its numerical and experimental validation, by smartphone measurement of the dynamic responses of an ordinary vehicle. *Journal of Sound and Vibration,* 457**,** 92-117.

Appendix A – Inverse Newmark-Beta Method to Find the Railway Track Apparent Profile Using In-Service Train

Note to the Reader:

This appendix extends the Inverse Newmark-Beta method of half car model described in Chapter 2 and Chapter 3 to calculate the railway track apparent profile. The purpose of doing so is to illustrate that the simple model can be useful in more complex models.

Appendix A – Inverse Newmark-Beta Method to Find the Railway Track Apparent Profile Using In-Service Train

A.1 Introduction

In Chapter 2, a new Inverse Newmark-Beta method is developed to calculate road profile using a half-car model. Here, this method is used to determine a flexible track apparent profile (AP). For the forward problem, a train-track model is used to generate vehicle accelerations. This model is developed from the train-track-bridge model described by Cantero et al. (2016). For the vehicle, a 4-axle railway carriage model which has ten degrees of freedoms (DOF) is used. As shown in Figure A.1, it includes four wheelsets (allowing vertical translation only), two bogies (allowing vertical translation and rotation about each centre of gravity) and the main body (allowing for vertical translation and rotation). For the track, a three-layer track model is used (Figure A.2). The track is modelled using beam elements and is supported by masses and springs. The masses represent sleepers and ballast and the springs represent the pad, ballast and sub-ballast.

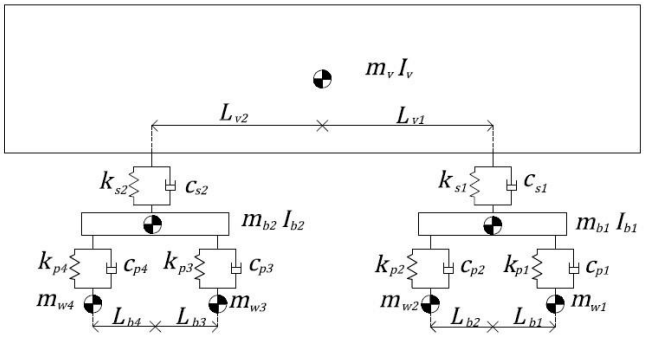

Figure A.1 4-axle railway carriage model.

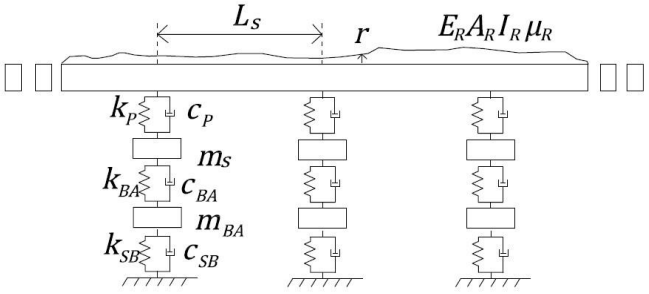

Figure A.2 Three-layer track model.

For the inverse problem, a 4 degree-of-freedom half-car model used in Chapter 2 and a 2 degree-of-freedom half-car model used in Chapter 3 are used separately to back-calculate the track APs. The half car models are shown in Figure A.3 and A.4.

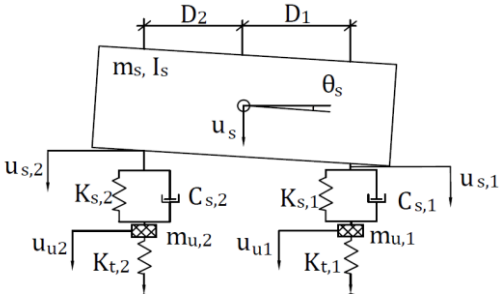

Figure A.3 4-degree-of-freedom half car model.

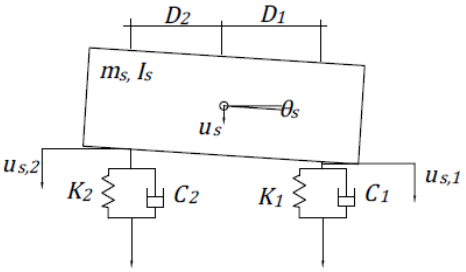

Figure A.4 2-degree-of-freedom half car model.

A.2 Results with 4-Degree-of-Freedom Half Car Model

For the forward problem, the train-track model is used to generate vehicle accelerations and rotation accelerations of the main body and one bogie which are regarded as the 'measured' data. The properties of the train are given in Table A.1. Using this 'measured' data, the 4-degree-of-freedom half-car model is used in different way to calculate the track profile under the vehicle. The properties of the half-car model are given in Table A.2.

Method 1: Firstly, the whole 4-axle railway carriage model is represented by the half-car model. Then, the Inverse Newmark-Beta method introduced in Chapter 2 is used to solve this half-car model. Here, 'measured' accelerations and rotation accelerations of main body are used as inputs. The results are shown in Figure A.5. It has a constant difference between calculated APs and true APs because of the initial values. After shifting, the calculated APs has the same shape as the 'true' APs, but it is not accurate.

Method 2: Then, the half-car model represents the bogie of the train model and the track APs under the first bogie are calculated using the Inverse Newmark-Beta method. Here, the 'measured' accelerations and rotations of the bogie are used. Same as before, it has a constant difference between calculated APs and true APs (Figure A.6). But after shifting, the calculated APs is close to the 'true' APs.

Table A.1 Train properties in the forward problem.

Property	Symbol	Unit	Value
Carriage body mass	m_v	kg	32.4×10^3
Carriage body moment of inertia	I_v	kg m^2	1.99×10^6
Speed	v	m/s	33
Bogie mass	m_b	kg	2 615
Bogie moment of inertia	I_b	kg m^2	1 476
Wheelset mass	m_w	kg	1 813
Primary suspension stiffness	k_p	N/m	2.4×10^6
Secondary suspension stiffness	k_s	N/m	0.86×10^6
Primary suspension damping	c_p	N s/m	7×10^3
Secondary suspension damping	c_s	N s/m	16×10^3
Distance between bogie centre of gravity and wheelsets	L_b	m	1.28
Distance between main body centre of gravity and bogies	L_v	m	9.5

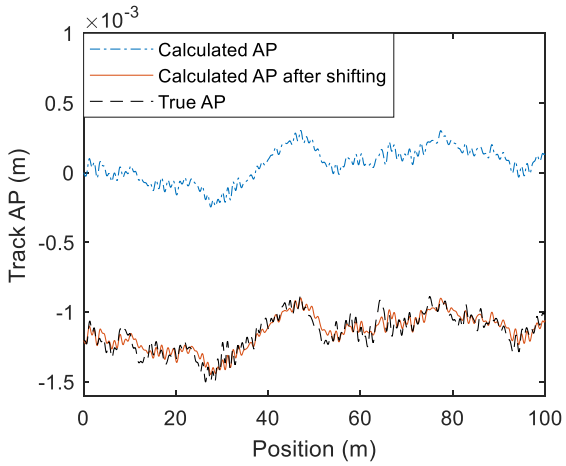

Figure A.5 Calculated AP, calculated AP after shifting and true profile of Method 1.

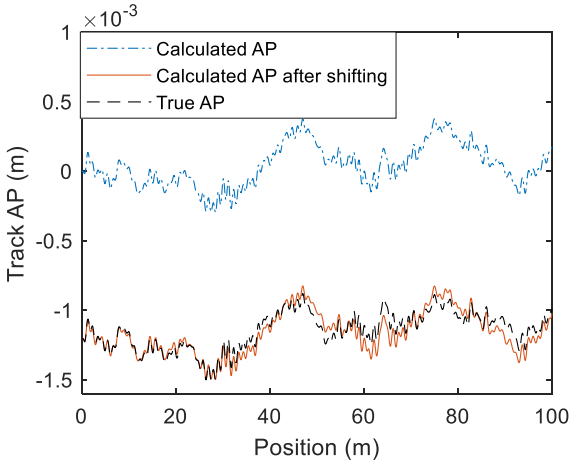

Figure A.6 Calculated AP, calculated AP after shifting and true profile of Method 2.

Table A.2 4-degree-of-freedom half-car properties in Method 1 and Method 2.

Property	Symbol Value and Unit	Method 1	Method 2
Pitch Moment	I_s (kg m^2)	1.99×10^6	1 476
Body mass	m_s (kg)	32.4×10^3	2 615
Axle mass	m_u (kg)	2 615	1 813
Suspension Stiffness	K_s (N/m)	0.86×10^6	2.4×10^6
Tyre Stiffness	K_t (N/m)	4.8×10^6	1×10^9
Suspension Damping	C_s (N s/m)	16×10^3	7×10^3
Distance of axle to centre of gravity	D (m)	9.5	1.28

A.3 Results with 2-Degree-of-Freedom Half Car Model

A 2-degree-of-freedom half-car model is used again to represent the bogie of the train model. The track APs are calculated using the 'measured' accelerations and rotations of the bogie by the Inverse Newmark-Beta method. The properties used is shown in Table A.3. The results show that the calculated APs is close to the 'true' APs after shifting (Figure A.7).

Table A.3 2-degree-of-freedom half-car properties.

Property	Symbol	Unit	Value
Sprung mass	m_s	kg	2,615
Sprung mass moment of inertia	I_s	kg m^2	1,476
Spring stiffness	K_1, K_2	N/m	2.4×10^6
Damping	C_1, C_2	N s/m	7×10^3
Distance of axle to body centre of gravity	D_1, D_2	m	1.28

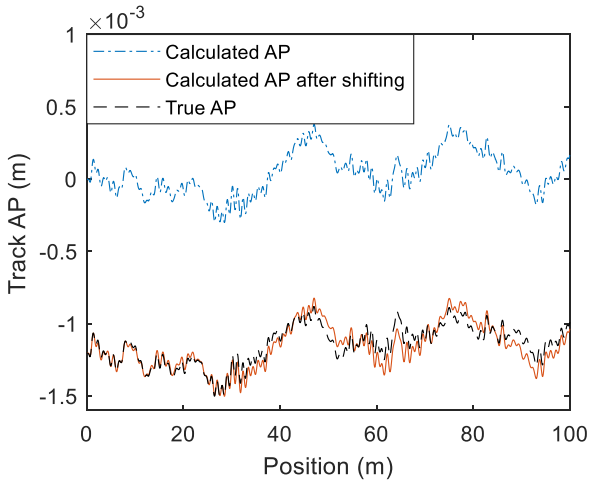

Figure A.7 Calculated AP, calculated AP after shifting and true profile of 2-degree-of-freedom half car model.

A.4 Conclusion

Previous research has shown that railway track AP is a good indicator for monitoring the conditions of railways and can be determined using a complex optimization method. This involves finding the profile that gives a best fit to the measured data which is computationally expensive and time consuming. Here, the railway track AP is calculated using Inverse Newmark-Beta Method. The railway car model is represented using the simple half-car model. The calculated AP is calculated in a fraction of the computing time and the results are very close to the 'true' ones. This method still works even the model is simpler than the true behaviour.

Appendix B – Inverse Newmark-Beta Process

Appendix B – Inverse Newmark-Beta Process

B.1 Introduction

This appendix contains Inverse Newmark-Beta method of 4-axle train carriage model used in Chapter 3 and quarter-car model used in Chapter 4.

B.2 Inverse Newmark-Beta Method of 4-Axle Train Carriage Model

Hence, for the inverse problem, $\ddot{u}_{b1}, \ddot{u}_{b2}, \dot{\theta}_{b1}$ and $\dot{\theta}_{b2}$ are known inputs. Same as Equation (3.10), other values can be obtained by integration of the inputs:

$$\dot{u}_{b1,t+\Delta t} = \dot{u}_{b1,t} + a_6\ddot{u}_{b1,t} + a_7\ddot{u}_{b1,t+\Delta t} \tag{B.1}$$

$$u_{b1,t+\Delta t} = (\ddot{u}_{b1,t+\Delta t} + a_2\dot{u}_{b1,t} + a_3\ddot{u}_{b1,t})/a_0 + u_{b1,t} \tag{B.2}$$

$$\dot{u}_{b2,t+\Delta t} = \dot{u}_{b2,t} + a_6\ddot{u}_{b2,t} + a_7\ddot{u}_{b2,t+\Delta t} \tag{B.3}$$

$$u_{b2,t+\Delta t} = (\ddot{u}_{b2,t+\Delta t} + a_2\dot{u}_{b2,t} + a_3\ddot{u}_{b2,t})/a_0 + u_{b2,t} \tag{B.4}$$

$$\ddot{\theta}_{b1,t+\Delta t} = (\dot{\theta}_{b1,t+\Delta t} - \dot{\theta}_{b1,t} - a_6\ddot{\theta}_{b1,t})/a_7 \tag{B.5}$$

$$\theta_{b1,t+\Delta t} = (\dot{\theta}_{b1,t+\Delta t} + a_4\dot{\theta}_{b1,t} + a_5\ddot{\theta}_{b1,t})/a_1 + \theta_{b1,t} \tag{B.6}$$

$$\ddot{\theta}_{b2,t+\Delta t} = (\dot{\theta}_{b2,t+\Delta t} - \dot{\theta}_{b2,t} - a_6\ddot{\theta}_{b2,t})/a_7 \tag{B.7}$$

$$\theta_{b2,t+\Delta t} = (\dot{\theta}_{b2,t+\Delta t} + a_4\dot{\theta}_{b2,t} + a_5\ddot{\theta}_{b2,t})/a_1 + \theta_{b2,t} \tag{B.8}$$

According to Equation (3.1)-(3.8), the equations of motion of the main body can be expressed:

$$m_v\ddot{u}_{v,t+\Delta t} + (c_{s1} + c_{s2})\dot{u}_{v,t+\Delta t} - c_{s1}\dot{u}_{b1,t+\Delta t} - c_{s2}\dot{u}_{b2,t+\Delta t} + (L_{v1}c_{s1} - L_{v2}c_{s2})\dot{\theta}_{v,t+\Delta t} + (k_{s1} + k_{s2})u_{v,t+\Delta t} - k_{s1}u_{b1,t+\Delta t} - k_{s2}u_{b2,t+\Delta t} + (L_{v1}k_{s1} - L_{v2}k_{s2})\theta_{v,t+\Delta t} = m_v g \tag{B.9}$$

$$J_v\ddot{\theta}_{v,t+\Delta t} + (L_{v1}c_{s1} - L_{v2}c_{s2})\dot{u}_{v,t+\Delta t} - L_{v1}c_{s1}\dot{u}_{b1,t+\Delta t} + L_{v2}c_{s2}\dot{u}_{b2,t+\Delta t} + (L_{v1}{}^2c_{s1} + L_{v2}{}^2c_{s2})\,\dot{\theta}_{v,t+\Delta t} + (L_{v1}k_{s1} - L_{v2}k_{s2})u_{v,t+\Delta t} - L_{v1}k_{s1}u_{b1,t+\Delta t} + L_{v2}k_{s2}u_{b2,t+\Delta t} + (L_{v1}{}^2k_{s1} + L_{v2}{}^2k_{s2})\,\theta_{v,t+\Delta t} = 0 \quad \text{(B.10)}$$

In the Newmark-Beta method,

$$\ddot{u}_{v,t+\Delta t} = a_0(u_{v,t+\Delta t} - u_{v,t}) - a_2\dot{u}_{v,t} - a_3\ddot{u}_{v,t} \quad \text{(B.11)}$$

$$\dot{u}_{v,t+\Delta t} = a_1(u_{v,t+\Delta t} - u_{v,t}) - a_4\dot{u}_{v,t} - a_5\ddot{u}_{v,t} \quad \text{(B.12)}$$

$$\dot{\theta}_{v,t+\Delta t} = a_1(\theta_{v,t+\Delta t} - \theta_{v,t}) - a_4\dot{\theta}_{v,t} - a_5\ddot{\theta}_{v,t} \quad \text{(B.13)}$$

$$\ddot{\theta}_{v,t+\Delta t} = a_0(\theta_{v,t+\Delta t} - \theta_{v,t}) - a_2\dot{\theta}_{v,t} - a_3\ddot{\theta}_{v,t} \quad \text{(B.14)}$$

Substituting (B.11)-(B.14) into (B.9) and (B.10)

$$\begin{aligned} m_v(a_0(u_{v,t+\Delta t} - u_{v,t}) - a_2\dot{u}_{v,t} - a_3\ddot{u}_{v,t}) + (c_{s1} + c_{s2})(a_1(u_{v,t+\Delta t} - u_{v,t}) - a_4\dot{u}_{v,t} \\ - a_5\ddot{u}_{v,t}) - c_{s1}\dot{u}_{b1,t+\Delta t} - c_{s2}\dot{u}_{b2,t+\Delta t} + (L_{v1}c_{s1} - L_{v2}c_{s2})(a_1(\theta_{v,t+\Delta t} - \theta_{v,t}) \\ - a_4\dot{\theta}_{v,t} - a_5\ddot{\theta}_{v,t}) + (k_{s1} + k_{s2})u_{v,t+\Delta t} - k_{s1}u_{b1,t+\Delta t} - k_{s2}u_{b2,t+\Delta t} \\ + (L_{v1}k_{s1} - L_{v2}k_{s2})\theta_{v,t+\Delta t} = m_v g \end{aligned} \quad \text{(B.15)}$$

$$\begin{aligned} J_v(a_0(\theta_{v,t+\Delta t} - \theta_{v,t}) - a_2\dot{\theta}_{v,t} - a_3\ddot{\theta}_{v,t}) + (L_{v1}c_{s1} - L_{v2}c_{s2})(a_1(u_{v,t+\Delta t} - u_{v,t}) - \\ a_4\dot{u}_{v,t} - a_5\ddot{u}_{v,t}) - L_{v1}c_{s1}\dot{u}_{b1,t+\Delta t} + L_{v2}c_{s2}\dot{u}_{b2,t+\Delta t} + (L_{v1}{}^2c_{s1} + L_{v2}{}^2c_{s2})\,(a_1(\theta_{v,t+\Delta t} - \\ \theta_{v,t}) - a_4\dot{\theta}_{v,t} - a_5\ddot{\theta}_{v,t}) + (L_{v1}k_{s1} - L_{v2}k_{s2})u_{v,t+\Delta t} - L_{v1}k_{s1}u_{b1,t+\Delta t} + L_{v2}k_{s2}u_{b2,t+\Delta t} + \\ (L_{v1}{}^2k_{s1} + L_{v2}{}^2k_{s2})\,\theta_{v,t+\Delta t} = 0 \end{aligned} \quad \text{(B.16)}$$

In Equations (B.15) and (B.16), all symbols are given except $u_{v,t+\Delta t}$ and $\theta_{v,t+\Delta t}$. So $u_{v,t+\Delta t}$ and $\theta_{v,t+\Delta t}$ could be solved now and $\ddot{u}_{v,t+\Delta t}, \dot{u}_{v,t+\Delta t}, \dot{\theta}_{v,t+\Delta t}, \ddot{\theta}_{v,t+\Delta t}$ can be calculated from $u_{v,t+\Delta t}$ and $\theta_{v,t+\Delta t}$ using Equations (B.11) to (B.14). Therefore, all the symbols in left side of Equation (3.1) are known and the right side of Equation (3.1), F can be found, say

$$F = \begin{Bmatrix} F_1 \\ F_2 \\ F_3 \\ F_4 \\ F_5 \\ F_6 \end{Bmatrix} \tag{B.17}$$

$$m_{b1}g + k_{p1}r_{w1} + c_{p1}r'_{w1} + k_{p2}r_{w2} + c_{p2}r'_{w2} = F_2 \tag{B.18}$$

$$m_{b2}g + k_{p3}r_{w3} + c_{p3}r'_{w3} + k_{p4}r_{w4} + c_{p4}r'_{w4} = F_3 \tag{B.19}$$

$$L_{b11}\left(k_{p1}r_{w1} + c_{p1}r'_{w1}\right) - L_{b12}\left(k_{p2}r_{w2} + c_{p2}r'_{w2}\right) = F_5 \tag{B.20}$$

$$L_{b21}\left(k_{p3}r_{w3} + c_{p3}r'_{w3}\right) - L_{b22}\left(k_{p4}r_{w4} + c_{p4}r'_{w4}\right) = F_6 \tag{B.21}$$

To get the $k_{p1}r_{w1} + c_{p1}r'_{w1}$, the terms, r_{w2} and r'_{w2} can be removed by combining Equation (B.18) with (B.20), scaled by L_{b12}. Finally, the profile r_{w1} is calculated in the third step by solving for $k_{p1}r_{w1} + c_{p1}r'_{w1}$ as a 1st order differential equation in r_{w1}. This is solved using the Runge-Kutta method (Gonzalez et al., 2012). Same as this, other profile r_{w2}, r_{w3} and r_{w4} can be calculated separately.

B.3 Inverse Newmark-Beta Method of Quarter-Car Model

Here, the Inverse Newmark-Beta method is further developed using a quarter-car model which is used in Chapter 4. The quarter car consists of a sprung mass, M, and an unsprung mass, m, which represent the body and axle masses of the vehicle system respectively. A spring of stiffness K and a viscous damper of value c connect the sprung mass and unsprung mass together. The axle mass connects to the road/rail surface via a sprung of stiffness, k.

The equations of motion of the vehicle can be defined as:

$$M_1\ddot{u} + C_1\dot{u} + K_1u = f_v \tag{B.22}$$

where M_1, C_1, and K_1 are the mass, damping and stiffness matrices of the vehicle respectively. The parameters, $\ddot{u}$, $\dot{u}$ and u are vehicle acceleration, velocity and displacement vectors respectively. The displacement vector of the vehicle is, $u = \{u_s, u_u\}^T$. The time-varying dynamic interaction force vector by f_v where $f_v = \{0, F_t\}^T$. The dynamic interaction force is, $F_t = k \times y$; where y is the profile. The matrices are given by:

$$M_1 = \begin{bmatrix} M & 0 \\ 0 & m \end{bmatrix} \quad \text{(B.23)}$$

$$C_1 = \begin{bmatrix} c & -c \\ -c & c \end{bmatrix} \quad \text{(B.24)}$$

$$K_1 = \begin{bmatrix} K & -k \\ -K & K+k \end{bmatrix} \quad \text{(B.25)}$$

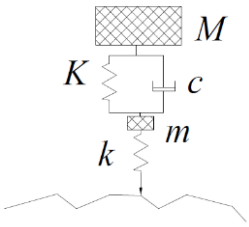

Figure B.1. Quarter-car model and road model

The mass, damping and stiffness matrices of the vehicle M_1, C_1, and K_1 are assumed initially to be known. Also, the acceleration of the sprung mass $\ddot{u}_s$ will be measured and therefore assumed to be known for each time step. Then, the displacement and velocity of the sprung mass in each time step can be calculated using the Newmark-Beta method:

$$u_{s,t+\Delta t} = (\ddot{u}_{s,t+\Delta t} + a_2 \times \dot{u}_{s,t} + a_3 \times \ddot{u}_{s,t})/a_0 + u_{s,t} \quad \text{(B.26)}$$

$$\dot{u}_{s,t+\Delta t} = \dot{u}_{s,t} + a_7 \times \ddot{u}_{s,t+\Delta t} + a_6 \times \ddot{u}_{s,t} \quad \text{(B.27)}$$

Taking Equations (B.22) to (B.25),

$$M \times \ddot{u}_{s,t+\Delta t} + c \times \dot{u}_{s,t+\Delta t} - c \times \dot{u}_{u,t+\Delta t} + K \times u_{s,t+\Delta t} - K \times u_{u,t+\Delta t} = 0 \quad \text{(B.28)}$$

$$m \times \ddot{u}_{u,t+\Delta t} - c \times \dot{u}_{s,t+\Delta t} + c \times \dot{u}_{u,t+\Delta t} - K \times u_{s,t+\Delta t} + (K+k) \times u_{u,t+\Delta t} = k \times y \quad \text{(B.29)}$$

In the Newmark-Beta method, for unsprung mass:

$$\dot{u}_{u,t+\Delta t} = a_1 \times (u_{u,t+\Delta t} - u_{u,t}) - a_4 \times \dot{u}_{u,t} - a_5 \times \ddot{u}_{u,t} \quad \text{(B.30)}$$

Substituting Equation (B.30) into Equation (B.28) to replace $\dot{u}_{u,t+\Delta t}$:

$$u_{u,t+\Delta t} = (M \times \ddot{u}_{s,t+\Delta t} + c \times \dot{u}_{s,t+\Delta t} + K \times u_{s,t+\Delta t} + c \times a_4 \times \dot{u}_{u,t} + c \times a_5 \times \ddot{u}_{u,t} + c \times a_1 \times u_{u,t})/(c \times a_1 + K) \quad \text{(B.31)}$$

Hence, the displacement and velocity of the unsprung mass can be calculated as follows:

$$\dot{u}_{u,t+\Delta t} = a_1 \times (u_{u,t+\Delta t} - u_{u,t}) - a_4 \times \dot{u}_{u,t} - a_5 \times \ddot{u}_{u,t} \quad \text{(B.32)}$$

$$\ddot{u}_{u,t+\Delta t} = a_0 \times (u_{u,t+\Delta t} - u_{u,t}) - a_2 \times \dot{u}_{u,t} - a_3 \times \ddot{u}_{u,t} \quad \text{(B.33)}$$

The effective stiffness matrix is:

$$[\bar{K}] = [K_1] + a_0 \times [M_1] + a_1 \times [C_1] \quad \text{(B.34)}$$

The effective force is:

$$\bar{F}_{t+\Delta t} = \bar{K} \times u_{t+\Delta t} \quad \text{(B.35)}$$

$$F_{t+\Delta t} = \bar{F}_{t+\Delta t} - M_1 \times (a_0 \times u_t + a_2 \times \dot{u}_t + a_3 \times \ddot{u}_t) - C_1 \times (a_1 \times u_t + a_4 \times \dot{u}_t + a_5 \times \ddot{u}_t) \quad \text{(B.36)}$$

Finally, the profile can be calculated as follows:

$$y_{t+\Delta t} = F_{t+\Delta t}/k \quad \text{(B.37)}$$

where, in the Newmark- Beta method, the integration constants are as listed here for time step, Δt:

$$\gamma = 0.8, \quad \beta = 0.25 \times (0.5 + \gamma)^2, \quad a_0 = \frac{1}{\beta \times \Delta t^2}, \quad a_1 = \frac{\gamma}{\beta \times \Delta t},$$
$$a_2 = \frac{1}{\beta \times \Delta t}, a_3 = \frac{1}{\beta \times 2} - 1, a_4 = \frac{\gamma}{\beta} - 1, a_5 = \frac{\Delta t}{2} \times \left(\frac{\gamma}{\beta} - 2\right), a_6$$
$$= (1 - \gamma) \times \Delta t, a_7 = \gamma \times \Delta t \quad \text{(B.38)}$$